Time Synchronization in Multimodal Wireless Cyber-Physical Systems
A Wearable Biopotential Acquisition and Collaborative Brain-Computer Interface Paradigm

Von der Fakultät für Ingenieurwissenschaften,

Abteilung Elektrotechnik und Informationstechnik

der

Universität Duisburg-Essen

zur Erlangung des akademischen Grades

Doktors der Ingenieurwissenschaften

genehmigte Dissertation

von

M. Sc. Unmesh Ghoshdastider

aus

Kalkutta

1. Gutachter: Prof. Ph. D. Michael Kraft
2. Gutachter: Prof. Dr.-Ing. Torben Weis

Tag der mündlichen Prüfung: 4. Dezember 2015

Zusammenfassung

Die Forschung zu Brain-Computer Interface (BCI) hat in den letzten drei Jahren riesige Fortschritte gemacht, nicht nur im Bereich der menschlich gesteuerten Roboter, der Steuerung von Prothesen, des Interpretierens von Wörtern, der Kommunikation in einer Virtual Reality Umgebung oder der Computerspiele, sondern auch in der kognitiven Neurologie. Patienten, die unter enormen motorischen Dysfunktionen leiden (letztes Stadium *Amyotrophe Lateralsklerose*) könnten solch ein BCI System als alternatives Medium zur Kommunikation durch die eigene Gehirnaktivität nutzen. Neuste Studien zeigen, dass die Verwendung dieses BCI Systems in einem Gruppenexperiment helfen kann die menschliche Entscheidungstreffung deutlich zu verbessern. Dies ist ein neues Feld des BCI, nämlich das *Collaborative BCI*. Einerseits erfordert die Durchführung solch eines Gruppenexperiments drahtlose Hochleistungs-EEG Systeme, basierend auf BCI, welches kostengünstig und tragbar sein sollte und Langzeit-Monitoring hochwertiger EEG Daten sicherstellt. Andererseits ist es erforderlich, eine Zeitsynchronisierung zwischen den einzelnen BCI Systemen einzusetzen, damit diese für ein Gruppenexperiment zum Einsatz kommen können. Diese Herausforderungen setzten die Grundlage dieser Doktorarbeit.

In dieser Arbeit wurde ein neuartiges, nicht invasives, modulares, biopotentiales Messsystem entwickelt: Dieses kann Breitband (0.5 Hz–150 Hz) Biopotentiale ableiten, bestehend aus Elektromyographie (EMG), Elektrokardiografie (EKG), Elektroencephalografie (EEG), wurde insgesamt bezeichnet als ExG bzw. das Messsystem als *ExG-System* benannt. Die Modularität des ExG-Systems erlaubt 8 bis hin zu 256 Kanäle zu konfigurieren, je nach Anforderung, ob in einen textilen Schlauch eingekapselt zur Erfassung von EMG Signalen, in eine textilen Weste zur Erfassung von ECG Signalen oder in eine textilen Kappe zur Erfassung von EEG Signalen. Der Einbau des ExG-Systems in eine Kappe wurde ebenfalls im Rahmen der Arbeit entwickelt. Der letzte Schritt des ExG-Systems zeigt niedriges Eingangsrauschen von $\sim$7 $\mu V_{\text{von-Spitze-zu-Spitze}}$ und benötigt 41 mW/Kanal der Datenaufnahme im aktiven Zustand. Ein WiFi-Modul wurde für eine drahtlose Datenübertragung an einen ferngesteuerten PC in das ExG-System eingebaut. Um mit dem entwickelte System BCI Anwendungen zu ermöglichen, wurde ein akustisch und visuell evozierter Potenzialstimulator (SSVEP/AEP Stimulator) entwickelt. In eben diesem wurde ein *Rasperry Pi* als Zentralrechner benutzt und ein *Bash* basiertes Player-Skript

einprogrammiert, das Mediadaten (Video, Audio, Ton) aus der Angabe einer Lookup Tabelle (LUT) in ihr *Linux* Betriebssystem spielt.

Im Rahmen der Arbeit wurde eine Zeitsynchronisierung an einigen dieser ExG-Systeme mit Hilfe von einer eingebetteten Hardware/Softwarelösung durchgeführt. Die Hardwareteile bestehen aus einigen Leiterplatten, nämlich *Sync* Modulen mit einem Quarzoszillator, einem Mikrocontroller und einem Funkmodul (Hierbei *Bluetooth* 4.0). Eines von diesen ist das *Sync-Addon*, das mit jedem Messsystem (z.B. ExG-System) das zu synchronisieren ist, angeschlossen wird. Das andere bezeichnet man als *Sync-Center*, das an die Datenverarbeitungsrechner angehängt wird. Das Softwareteil übernimmt den Zeitsynchronisierungsmechanismus mit Hilfe eines funkbasierten Protokolls. Im Rahmen der Arbeit wurde ein neues energieeffizientes *pairwise broadcast Zeitsynchronisationsprotokoll* (PBS), welches nur theoretisch vorgestellt wurde, experimentell verifiziert. Außerdem wurde es mit anderen bestehenden Zeitsynchronisationsprotokollen auf dem aktuellen Stand der Technik evaluiert, basierend auf den Ergebnissen der gleichen Hardwareebene. In der letzten Iteration der Sync-Module wurde ein durchschnittlicher Synchronisationsfehler von ~2 ms, den Konfidenzintervall von 95% berücksichtigend, erlangt. Da für Collaborative BCI, P300, ein Ereignis bezogenes Potenzial mit dem Auslöseimpuls, der $300-500$ ms nach dem Vorgang eintritt, eingestellt wurde, ist die erreichte Synchronisationsgenauigkeit genügend, um solch ein Experiment durchzuführen.

Abstract

Brain-computer interface (BCI) has experienced the last three decades tremendous technological advances not only in the field of human controller robotics, or in controlling prosthesis, or in spelling words, or in interacting with a virtual reality environment, or in gaming but also in cognitive neuroscience. Patients suffering from severe motoric dysfunction (e.g. late stage of Amyotrophic Lateral Sclerosis) may utilise such a BCI system as an alternative medium of communication by mental activity. Recently studies have shown that usage of such BCI in a group experiment can help to improve human decision making. This is a new field of BCI, namely collaborative BCI. On one hand, performing such group experiments require wireless, high density EEG system based BCI which should be low-cost, wearable and provide long time monitoring of good quality EEG data. On the other hand time synchronization is required to be established among a group of BCI systems if they are employed for such a group experiments. These drawbacks set the foundation of this thesis work.

In this work a novel non-invasive modular biopotential measurement system which can acquire wideband (0.15 Hz–200 Hz) biopotential signals consisting Electromyography (EMG), Electrocardiography (ECG), Electroencephalography (EEG) together called ExG, following ExG-system was designed. The modularity of the ExG-system allows it to be configured from 8 up to 256 channels according to the requirement if it's to be encapsulated in a textile sleeve for recording of EMG signals, or in a textile vest for recording of ECG signals, or in a textile cap for recording of EEG signals. The assembly of the ExG-system in cap was also developed during the scope of the work. The final iteration of the ExG-system exhibits low input noise of ~ 7 $\mu V_{\text{peak-to-peak}}$ and require 41 mW/channel of data recording in active state. A WiFi module was embedded into the ExG-system for wireless data transmission to a remote PC. To enable the developed system for BCI applications a steady-state visually/auditory evoked potential stimulator (SSVEP/AEP stimulator) incorporating a *Raspberry Pi* as a main computer and a bash based player script which plays media data (video, pictures, sound) as defined in a lookup table in the *Linux* operating system of it.

Within the scope of the work time synchronization among a group of such ExG-systems was further realized with the help of an embedded hardware/software solution. The hardware part consists of two different PCB sync modules that are incorporated with a crystal oscillator a microcontroller, a radio module (in this case *Bluetooth 4.0*). One of them is

called the sync-addon which is to be attached to each of the measurement systems (e.g. ExG-system) that are to be synchronized and the sync-center which is to be attached to the remote PC. On the software part, a wireless time synchronization protocol exchanging tim-timing information among the sync-center and sync-addons must establish tight time synchronization between the ExG-system. Within the framework of this work, a novel time synchronization protocol energy efficient pairwise broadcast synchronization protocol (PBS) that was only theoretically proposed before but not evaluated on real hardware was experimentally evaluated with the developed sync modules. Moreover a benchmarking with other state-of-the-art existing time synchronization protocols based on the results from same hardware platform were drawn. In the final iteration of sync modules an average synchronization error of ~2 ms was achieved considering the 95% of confidence interval. Since for collaborative BCI, P300, an event related potential was triggered with the stimuli that occur 300−500 ms after the event, the achieved synchronization accuracy is sufficient to conduct such experiments.

Table of Contents

List of Figures

List of Tables

List of Abbreviations

Abbreviation	Meaning
µC	microcontroller
AC	alternating current
AD	*Analog Devices, Inc.*
ADC	analog-to-digital converter
AEP	auditory evoked potential
API	application peripheral interface
BCI	Brain-computer interface
BGR	band-gap reference
BLE	Bluetooth low energy
BOLD	blood-oxygen-level-dependent
CAN	controller area network
cBCI	collaborative Brain-computer interface
CE	*Conformité Européene*
CMRR	common-mode rejection ratio
CONFIG_STATE	configuration state
CPE	constant phase element
CPS	Cyber-physical system
CTS	clear-to-send
DAQ	data acquisition
DATA_STREAMING_STATE	data streaming state
DC	direct current
DMA	direct memory access

ECoG   electrocorticography

ECoG	electrocorticography
EEG	electroencephalography
EGG	electroglotography
EMF	electromotive force
EMG	electromyography
EMI	electromagnetic interference
EOG	somatosensory evoked potential
EOG	electrooculogram
EP	evoked potential
ERG	electroretinogram
ERP	event-related potential
FAULT_STATE	fault state
FCC	Federal Communications Commission
FIFO	first in first out
fMRI	functional magnetic-resonance imaging
FoM	*figure of merit*
FPU	floating point unit
FSM	finite state machine
FTSP	Flooding Time Synchronization Protocol
GAP	Generic Access Profile
GFSK	*Gaussian frequency shift keying*
GPIO	general-purpose input/output
GPS	global position system
GTP	global time provider
HBS	Hybrid Broadcast Synchronization
HPF	high-pass filter

IMU	inertial measurement unit
INA	instrument amplifier
INI_STATE	initialization state
INIT	initialization phase
IoT	Internet-of-Things
ISM	industrial scientific and medical
LFP	local field potential
LR	linear regression
LiPo	Lithium-Polymer
LL	Link Layer
LUT	lookup table
MAC	medium access control
MBS	Multi-hop Broadcast Synchronization
MEG	magnetoencephalogram
PBS	Pairwise Broadcast Synchronization
PCB	printed circuit board
PCB	personal computer
PPC	posterior parietal cortex
PSD	power spectral density
PSD	power spectrum
PSP	post-synaptic potential
Radio frequency	RF
RBS	Reference Broadcast Synchronization
RFI	radio frequency interference
RISC	reduced instruction set computing
RMS	root mean square
RT	reaction time

RTOS	real-time operating system
RTS	request-to-send
SA	synchronization-addon
SC	synchronization-center
SD card	secure digital memory card
SPI	Serial Peripheral Interface
SYNC	synchronization phase
sync error	*synchronization error*
TCP/IP	Transmission Control Protocol/Internet Protocol
TDM	time division multiplexing
TI	*Texas Instruments Incorporated*
TPSN	Timing-sync Protocol for Sensor Networks
TTL	transistor-transistor logic
UART	universal asynchronous receiver/transmitter
USART	universal asynchronous receiver/transmitter
USB	Universal Serial Bus
VEP	visually evoked potential
WAIT_STATE	wait state
WORK_STATE	working state
WSN	wireless sensor networks

List of Symbols

Latin Characters

Symbol	Unit	Meaning
T_{INTD}	s	the interrupt handling time at the host controller
$\bar{t}_i$	s	average of the local timestamps on node i
$\bar{t}_p$	s	average of the local timestamps on node p
Δ_{nm}	s	pairwise difference
A_x	s	difference between timestamps
B_x	s	difference between offsets
C_1^x		ratio between A_x and B_x
C_{bg}	F	coupling capacitance between ground and human body
C_{bp}	F	coupling capacitance between main AC and human body
C_{dl}	F	Double layer capacitance
C_{double}		double capacitor
C_{iso}	F	isolation capacitance between the ground of the amplifier battery and earth
C_{sh}	F	Capacitance between insulated electrode and tissue

E_{hc}	V	Voltage source
I_D	A	displacement current passes from human body to the coupling capacitor
N_M		number of Meridian-ADCs
$R_1,$	Ω	input resistance of the instrument amplifier
R_2	Ω	input resistance of the instrument amplifier
R_{ct}	Ω	resistance caused by Faradaic current
R_{el1}	Ω	input resistance of the amplifier
R_{el2}	Ω	input resistance of the amplifier
R_g	Ω	gain selecting resistance of the instrument amplifier
R_{gnd}	Ω	coupled resistance between ground of the amplifier and human body
R_s	Ω	resistance to the ion movement in the diffusion region
R_{sh}	Ω	shunt resistance from the insulated electrode to the tissue
R_t	Ω	resistance in the electrode from electrode site to electronic interface
$T_{BGLD,}$	s	the time required to process the message by the application peripheral interface (API) of the Bluetooth module
T_{GLD}	s	delay to transmit the message from the Link Layer

(LL) to the Generic Access Profile

$T_{UARTD,}$	s	the time to transmit the message over the UART
V_{CM}	V	common-mode voltage
V_{IN+}	V	Non-inverting input of the instrument amplifier
V_{IN-}	V	inverting input of the instrument amplifier
V_{out}	V	Output voltage of the instrument amplifier
Z_{in}	Ω	input impedance of the amplifier
d_l		Data loss in %
d_r		number of received data bytes
t_1	s	First timestamp
t_g	s	New global time of each node after adjustment
t_i	s	current time of each node
t_i^k	s	k$^{\text{th}}$ timestamp at the general node
$t_k^{SA\#m}$	s	timestamp on node SA#n
$t_k^{SA\#n}$	s	timestamp on node SA#n
t_p^k	s	k$^{\text{th}}$ timestamp at the reference node
$v_{elec-ns}$	V	lumped electrode intrinsic noise voltage sources
$\delta_{n,m}$	s	sync error between the SA#n and SA#m
ΔV_{IN}	V	differential error signal
Δt_k	s	The difference between two successive timestamps

		subtracted by the interval T
Δf	Hz	frequency range of interest
F	1/s	sample rate of the ADC
k	eVK-1	*Boltzmann*'s constant
k^{th}		number of a timestamp
M		number of incoming *Framemarkers*
$N.$		Number of messages
T	K	Kelvin temperature
T		interval between messages
T_{duration}		duration of the synchronization test
Vcc	V	operating voltage
Z	Ω	electrode magnitude impedance
G		Gain of the instrument amplifier

Greek Characters

Symbol	Unit	Meaning
$\theta_i^{d\_t}$		offset difference of node i w.r.t.t. parent node
$\bar{\theta}_{min}$		average of minimum offsets
θ_{min}^k		minimum of k number of offsets θ
$\varphi_i^{d\_t}$		skew difference of node i w.r.t.t. parent node
$\varphi_i^{d\_\theta}$		skew difference
$\cup$		velocity of the model train

1 Introduction

In this chapter the scientific basis of this thesis work will be created so that the motivation, need of the work, research problem and scientific innovation of it can be perceived. At first the motivation behind this work will be discussed. In line with motivation, the existing solution and its limitation will be introduced. This will lead to the research questions that were raised in the course of the formation of the work. To investigate the aroused questions, a scientific methodology that was followed during the work will be discussed. After that an overview of the scope of the work will be described before the concrete scientific goals and approach are being discussed.

1.1 Motivation

Cyber-physical systems (CPS) have recently been gaining popularity and emerging as a frontier technology in robotics and biomedical engineering. This progress is contributing to the enhancement of brain-computer interfaces (BCI) [1] which is having significant impact in brain science. Brain-computer interfaces (BCIs) were introduced to address as an

alternative medium for individuals to bypass conventional channels of com-communication (i.e. muscles and speech). This allowed a direct communication and control between the human brain and physical devices by translating different patterns of brain activities into commands in real time [2]. Recording of electroencephalography (EEG) can be achieved either invasive using electrocorticography (ECoG) method or non-invasive. ECoG method involves a surgery so that electrodes can be placed directly on or inside the cortex that makes it a less popular alternative in respect to non-invasive BCI. Apart from EEG, magnetoencephalogram (MEG), blood-oxygen-level-dependent (BOLD) signals, and (de) oxyhemoglobin concentrations can be used as inputs for BCI systems [3]. EEG has been the most popular signal input for developing BCI system due to its convenience to be used in practice and relatively lower cost.

BCI based application has huge potential in several disciplines starting from neurophysiology, ambulatory medical diagnostics, bionics to gaming. BCI based robotics could assist paralyzed patients; group BCI can be used to understand how human brain works; BCI can be used in automated divining and many more potential applications. However, BCI technology has not succeeded in bringing laboratory demonstration to a real-life application [4], [5] as this imposes many challenges in terms of signal integrity, signal quality, miniaturization or form factor, signal-to-noise ratio (SNR), and system assembly [6]. For instance, the accuracy of a single-trial EEG classification using a binary finger-tapping task (left hand vs. right hand) in BCI Completion II ranged from 51% to 84% from 15 research groups [6]. Neuroimaging studies of human cognitive, sensory, and motor processes are usually based on noninvasive techniques such as EEG, magnetoencephalography (MEG) or functional magnetic-resonance imaging (fMRI). These techniques have either inherently low temporal or low spatial

resolution, and suffer from low signal-to-noise ratio and/or poor sensitivity at higher-frequency [4]. Currently many applications suffer from the low ac-accuracy of single-trial classification. In achieving enhanced SNR, averaging methods were employed not only across multiple trials, but also on multiple subjects [6]. In event-related potential (ERP)-based BCI applications, averaging single trial is the common mean to improve system performance [7].

In such BCI application, the stimulus was played repeatedly many times to produce multiple trails from a single subject so that the averaging method could be applied. The main problem of this method arises when a real time access of the measured data is necessary. Moreover accessing multiple trails from a single subject is not practical in specific environments. A solution in such environments would be to fuse trials from multiple subjects. Statistically it was observed in human performance studies that a team of individuals always outperforms individuals especially when performance requires a collection of various skills, judgment and experience under time constraints [6]. An analogy from this fact can be utilized to state that a better performance could be expected if a single-trail EEG data from a group of people can be obtained, integrated, and time synchronously correlated. This hypothesis has triggered the development of the closed-loop collaborative method for BCI systems comprising wearable wireless EEG systems, and steady-state visual and auditory evoked potential (SSVEP/AEP) stimulator [8] that aims to improve BCI performance by fusing collaborative brain activities form a group of probands. In the BCI experiment as depicted in the Figure 1.1, the steady state visually and auditory evoked potential (SSVEP/AEP) stimulator together with an EEG-system forms a feedback loop in which the stimulator triggers the ERP or evoked potentials (EP) in human brains [9].
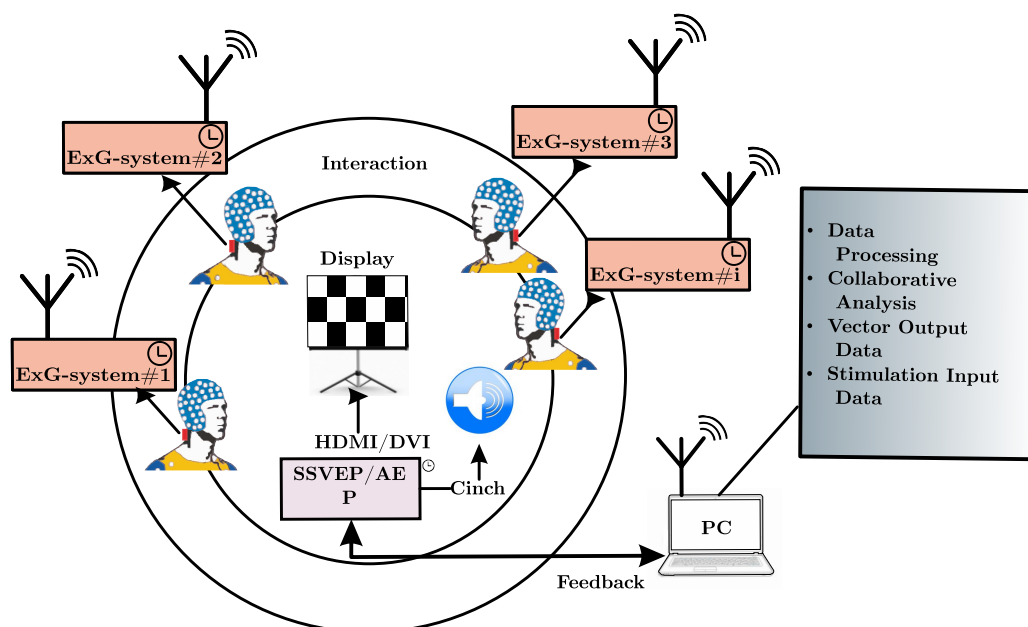
Figure 1.1 Overview of a cBCI scenario among a group of probands in a feed-back loop where each proband embodied with an EEG-system is stimulated with a common VEP/AEP-Stimulator. As per the EEG signal characteristics the software running on the PC modulates tone and video

A practical framework of collaborative BCI system was proposed for motor action paradigm [10] and its feasibility, practicability and usability were analyzed. Collaborative BCI shows a significant improvement (from 75.8% to 91.4%) in the classification accuracy for human decisions [6]. Yet, the unsolved problems that prevent to bring collaborative BCI to real life applications include low signal quality of non-invasive EEG, high-cost, lack of modularity, high-power consumption, bulky system size, and the challenge of real-time signal processing on multiple BCI platforms.

1.2 Research Questions

In comparison to single user BCI, collaborative BCI face considerable technological challenges in both bio-potential data recording from several subjects as well as processing the data time synchronously. Task scheduling and collaborative signal processing among the various BCI systems require a global time prevailing in each EEG-system. For example, in a group experiment many users are stimulated with a sequential stimulus data (image, video and acoustic) for neurofeedback training. Neurophysiologist are then interested to correlate the EEG data from the group of subjects at an instantaneous time to find out the occurrence of ERPs on users with a positive peak (in the range of 2–5 µV) that appears between $300-600$ ms after the stimulus. P300 is a common ERP which is used in non-invasive BCI [5]. Realizing a collaborative BCI using P300 ERP, arises the requirement of implementing time synchronization protocol for such group experiments. However, correlating in time the multimodal sensor data (EEG, video, audio) with each other is not trivial since each of the sensor nodes has its own clock with different frequency and stability.

As discussed in the paper [6], the framework for collaborative BCI system uses EEG as input signal. To realize a wireless collaborative BCI system, capable of transmitting data wirelessly to a remote PC being part of the same local area network, a biopotential acquisition system is required to be developed. The functionality of this biopotential acquisition system would require to be extended in such a way so that it could also be realized as a collaborative BCI. A stimulator for triggering ERPs and a live time synchronization using radio modules among EEG-systems are to be developed. Dealing with time synchronization in relation to collaborative EEG experiments has not been described in the literature to date, yet there

is a strong demand for time synchronization to enable further development of non-invasive BCI research. This thesis work strives to tackle these prob-problems.

Biomedical signals such as, electroencephalography (EEG), electrocardiogram (ECG), and Electromyography (EMG) have very low amplitude and low frequency. The signal bandwidth of EEG and ECG signals range from 0.1 up to 200 Hz and the amplitude of EEG in in the range between $2-100$ µV whereas the ECG signal amplitude lies in the range of 0.5 up to 4 mV [11], [12] It requires meticulous design methodologies in order to acquire and store these signals. Since developing a collaborative BCI requires the storage of data from multiple proband for long time, the system design should be optimized for low power consumption. The power consumption of the system should low enough, so that a 24 hours measurement with a light-weight Lithium-Polymer (LiPo) battery could be conducted. These specifications constitute the difficulty level of the system design. It is very uncomfortable for probands to wear conventional head-box containing wet passive electrodes which also hinders the proband's degree of freedom for long time and increase the risk of strangulation. This results in an increased demand of recording biopotentials with dry electrodes due to its minimal scalp preparation time. However dry electrodes have proved to be prone a voltage drift over time since the impedance between the skin and electrode varies. This is a trade-off of using dry electrodes for the development of biopotential measurement systems.

There exists a huge challenge in transferring the technology from the hospital to the homes of users. The designs of current solutions in hospitals are mostly too cumbersome, complex and gigantic to be brought outside the hospital environment and require expert assistance. Most of the EEG system with high channel density (over 64 channels) is huge box with lots of cables

that are impracticable to use outside clinic. A miniaturized, modular system concept with wireless data transmission capability is required to eradicate the risk of strangulation with wireless data transferring mechanism.

1.3 Scope of the Work

During the scope of this work it will be strived to develop a wireless, autarkic biopotential measurement system for long time recording of user data set to be used in collaborative BCI scenario. The system should comprise of interfaces that would let it to be enhanced into a functional collaborative BCI system. The corresponding steady-state visually or auditory evoked potential (SSVEP/AEP) stimulator will also be developed. Furthermore, a bunch of autarkic sync modules (comprising of a synchronization-center and several synchronization-addons) will be developed. Those modules will be responsible for live time synchronization of the biopotential measurement system with the help of a suitable wireless time synchronization protocol communicating their timing information on a different channel than that of the biopotential measurement system. This work will additionally provide a full custom system solution including the necessary software components that are required for each of the developed hardware modules (biopotential measurement system, stimulator, sync modules) of the entire BCI system i.e. a firmware for the biopotential measurement system and, a firmware with live time synchronization algorithm for the sync modules. In order to integrate the developed system into a wearable cap, vest, and arm sleeve, assembling and encapsulation of the hardware into suitable clothing will be presented.

1.4 Research Goal

The main three objectives of this thesis work are the following:

a) Develop a modular, low-power biopotential measurement system that can record from 8−256 channels of biopotential data including both the analog to digital signal processing chain.

b) Achieving a signal resolution of less than 10 µVpeak-to-peak.

c) Develop a SSVEP/AEP stimulator that plays media (video, audio) data from as specified in a lookup table (LUT).

d) Realizing synchronization wirelessly among the biopotential measurement systems so that they can me employed in collaborative BCI experiment scenarios for P300 based BCI applications.

1.5 Thesis Outline

In the following Chapter 2 the theoretical background required for the design and implementation of both biopotential measurement system and time synchronization will be described.

The Chapter 3 of the thesis will talk about the design, prototyping and encapsulation of the biopotential measurement system. It will describe the system in a top-down manner where it'll start with the description of the complete architecture of the biopotential measurement system and then describing each of its sub-units.

In the Chapter 4, the realization of time synchronization with an additional hardware module attachable to existing biopotential measurement system without any hardware modification, described before in the Chapter 3, will be presented.

The Chapter 6 will summarize and discuss the work. Thereafter a perspective for future work will be presented so that the system could go to pre-production phase from this research work.

At the end the Chapter 5 will introduce two novel group experiment scenarios where the developed time synchronized collaborative BCI system could be employed. One of them will introduce a quasi-stationary cBCI application scenario and another will introduce a dynamic cBCI application scenario.

2 Theoretical Background

Before starting the designing phase it is required to understand the basics of biopotential signals, biopotential electrodes and biopotential amplifiers. As this work is mainly focusing on the development of a time synchronized cBCI system, a brief introduction to BCI and diverse aspects of time synchronization will be discussed in this chapter.

2.1 Biopotential Signals

Below in the Table 2-I, the commonly used biopotentials signals, e.g. electrocardiography (ECG), EEG, electromyography (EMG), electroglotography (EGG), electroretinogram (ERG), electrooculogram (EOG), and evoked potentials e.g. auditory evoked potential (AEP), somatosensory evoked potential (SEP), visually evoked potential(VEP) with their typical characteristics are presented.

Table 2-I Range of amplitude and frequency of commonly used biopotential signals

Signal	Frequency [Hz]	Amplitude [mv]	Source
ECG (Heart)	0.01–250	0.5 –4	[11], [13]
EEG (Brain)	0.5–100	0.001 –100	[11], [13]
ECoG (Brain)	0–500	0.05–0.1	[14], [15]
EMG (Muscle)	0.01–10	50–10	[11], [13]
EGG (Throat)	0.02–0.2	0.0001–0.005	[13]
EUG (Uterus)	0–200	100–8000	[13]
ERG (Retina)	0.2–200	0.01–0.1	[11]
EOG (Eye)	0–100	0.005–0.2	[11], [13]
P300 (ERP)		4–10µV	[16], [17]

Since in this work only EEG, ECG were recorded, so the technical background of these biopotentials will be discussed in the following section of this chapter.

2.1.1 Introduction

Electrochemical activity of certain class of cells which are components of nervous, muscular, or glandular tissue acts towards the generation of biopotential signals. The potential of a membrane of an inactive cell is called *resting potential.* These cells can be considered as resting potentials in terms of electrical engineering and upon stimulation they generate action potential. Ion exchange through the cell membrane describes the electrical activity of each cell. At the rest state, the permeability of the membrane of the cell is more towards K^+ than Na^+, and the concentration of K^+ at the exterior of the cell is much lower than the exterior.
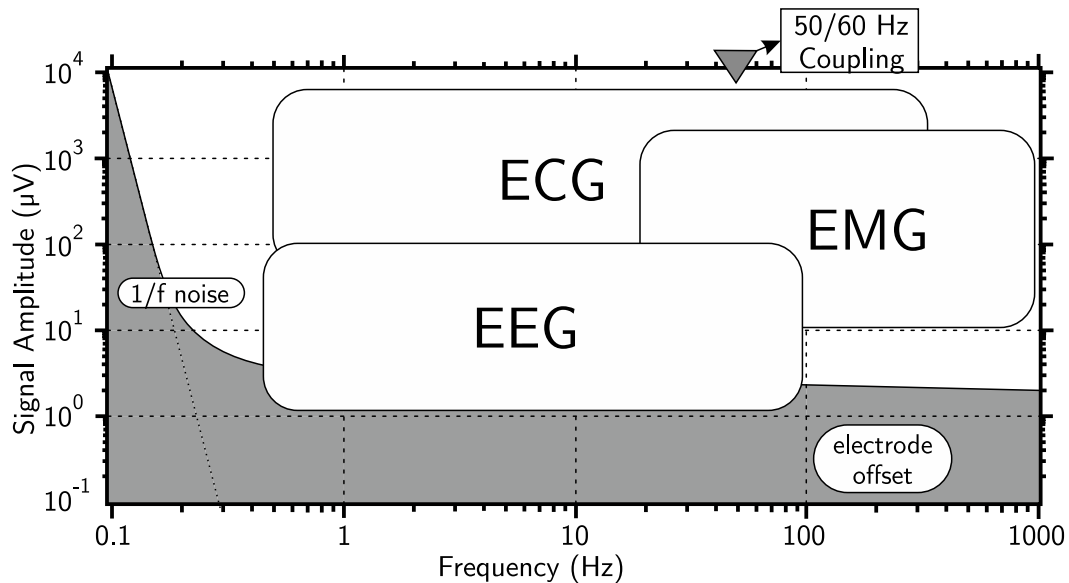
Figure 2.1 Amplitude and frequency characteristics of the biopotential signals, ECG, EEG, EMG and the correlating signals of the biopotential signals

That causes the occurrence of a diffusion gradient of K^+ at the exterior of the cell, creating a potential difference with respect to the interior – resulting in an electrical field towards the interior of the cell. At steady state, this

electric field balances the diffusion gradient and a polarization voltage of nearly −70 mV is reached at equilibrium. When the central nervous system stimulates the cell electrically, the permeability of the membrane towards Na^+ ions increases and a diffusion of Na^+ inside the cell occurs – resulting potential increase of the interior of the cell. As soon as the potential of the cell reaches +40 mV, the permeability of the membrane towards Na^+ decreases and increases towards K^+ − resulting a sharp decrease in the membrane while reaching to the rest state. This cycle of the cellular potential is called action potential. The biopotential signals, e.g. EEG, ECG, EMG, etc. are the consequence of diverse action potentials that are produced by combination of different cells [**18**].

The EEG is represented by a difference in potential measured between various points on the scalp. The electrical activity of the brain created by a group of neurons is measured with EEG. The electrical activity on the scalp arises as a result of neural activity whose action can be regarded as a collection of distributed current sources embedded in a volume conductor (the head). During the active stage of the brain, communication patterns alter across large number of neurons, primarily in the form of synaptic state changes. How such synaptic activity lead to local changes in membrane do is explained above. The local change in potential is termed as *post-synaptic potential* (PSP) [**19**]. The local field potential (LFP) was generated due to the changes in ionic currents and LFP associated with a single cell synaptic activity is very small. However a substantial current source is created when a synchronized activation of large number of specific set of neurons in the cortex sharing similar orientation during brain activity causing sum of the LFPs. A diverse combination of current sources occurs due to different brain states. These current sources are mixed and filtered as they manifest as biopotentials on the scalp. As a consequence an ill-defined inverse problem

can be stated that reconstructs the position and geometry of such sources (here volumetric localization of neural activity). However, the temporal reso-resolution of neural activity is unaffected and therefore the EEG contains accurate regarding timing of neural activation patterns [18]

Similarly ECG is the representation of electrical activity of heart. It is measured with electrodes placed on chest and it has three main feature characteristics. Those are P-wave, the QRS-complex, and the T-wave [20]. EMG is the electrical potential of the skeletal muscle cells, which is generated during the contraction of the muscle.

The distribution of amplitude and frequency of this standard biopotential signals EEG, ECG, EMG are shown in the Figure 2.1 that was measured with surface electrodes. There are three correlating signals that cause problem in extracting biopotential signals from human body. One of them is 1/f noise of the transistor present in the amplifier, secondly, 50-Hz interference from the mains, and the last one is the direct current (DC) differential electrode offset voltage between the biopotential electrodes and human skin. The readout circuit should be able reject, filter these unwanted signals, frequency present with the biopotential signals.

2.1.2 Biopotential Electrodes

There are two groups of biopotential electrodes and these are *polarizable* and *non-polarizable* electrodes. In the case of perfectly polarizable electrodes, electrodes have no actual charge transfer through the electrode-electrolyte interface. Therefore such electrode has a capacitive characteristic. The most common type of non-polarisable electrode is Ag/AgCl. The electrode metal is manufactured with Ag that is coated with an AgCl layer. An electrolyte gel is used to establish the electrical contact between electrode and the surface

of the skin. This kind of electrode is advantageous due to its low impedance and low artifact. However usage of such electrode creates discomfort and increases the preparation time of the acquisition system.

Dry electrode is the solution to the cumbersome wet Ag/AgCl where no gel is required as it name suggests. This helps to reduce the preparation time. However, due to the lack of the electrolyte, their characteristics are similar to polarizable electrode that behaves as a leaky capacitor. Therefore, the readout circuit for such electrode requires high input impedance ($\gg 1$ G Ω). Moreover it is required to place the read out circuit very close to the electrode to prevent electromagnetic interference and can be achieved using active electrodes [21]. The main disadvantage of the active electrodes lies in the requirement for matched components, which is non-trivial problem in CMOS process.

A pure capacitive electrode is a non-contact electrode which allows sensing biopotential signals remotely [22]. Since it does not draw DC current from the body, these are intrinsically safe and biocompatible. However the input impedance of the readout circuit is very high for extracting biopotential signals from non-contact electrodes. In addition these are very prone to motion artifacts since that cause change in capacitance.

The lumped-element functional model is shown in the Figure 2.2 that provides the basic representation of the primary functional elements of neural recording. With an electrode array containing L electrode sites, the model shows the biopotential acquisition from k neurons. Each electrode contains three functional submodels arranged in series (see Figure 2.2A). The first submodel shows the summation of biopotentials within the recording volume of the electrode; *neural interface tissue impedance* to represent the conductivity of the local tissue surrounding an electrode site; and an

electrode-tissue interface to represent electrochemical and electrical charac-characteristics of the electrode. Intrinsic neural noise resulting from the neural activity is too small and is represented by v_{neu-ns} input to the S node extrinsic biopotential noise that is caused by muscle activation (e.g. EMG) from cranial or extraocular muscle (e.g. EOG), by heart beats (e.g. ECG), and motion artifacts are represented by the lumped input v_{bio-ns}. The *neural interface tissue impedance submodel* (see Figure 2.2B) describes the tissue impedance surrounding an electrode site, caused by response of the localized reactive tissue. The biopotential signal transduction at the *electrode-tissue interface* (see Figure 2.2C) and transmission of the resulting signal through the electrodes to the electronics interface are described in terms of a submodels with lumped-element equivalent circuit [23], [24].
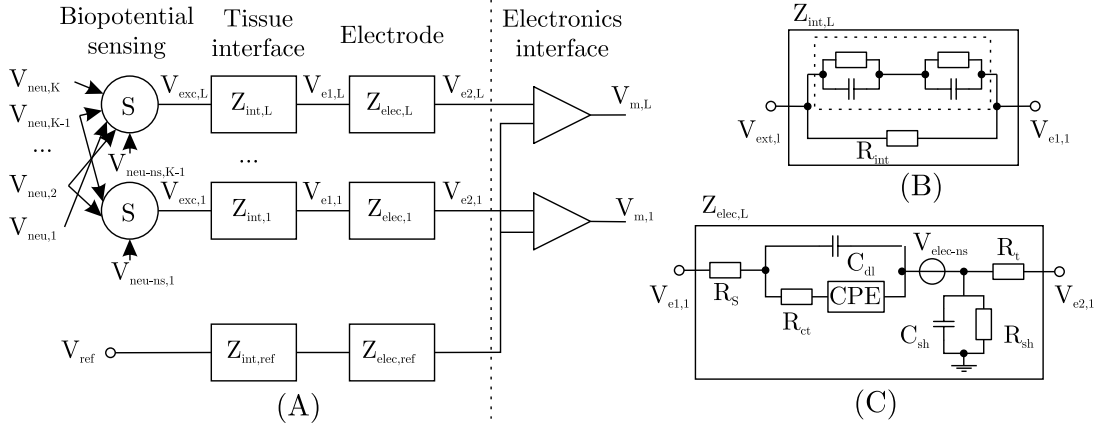
Figure 2.2 Lumped-element functional models of neural recording with a microelectrode array. (A) System model of extracellular neural recording from K neurons with an electrode array with L channels. The three components for each channels are biopotential sensing (S), tissue interface impedance ($Z_{int,j}$), and electrode equivalent impedance ($Z_{elec,j}$)(where j can range from 1 to L). (B) lumped-element equivalent circuit for impedance changes in the neural interface associated with reactive tissue responses. (C) lumped-element equivalent circuit of the electrode part.

The half-cell potential of the interface is represented with a voltage source E_{hc}. The capacitor C_{dl} represents double layer capacitance. The resistor R_{ct} represents the resistance to the transfer of charge that occurs because of the *Faradaic* currents. The constant phase element (CPE) impedance represents charge-transfer variations resulting from the surface morphology of the electrode site and the ion-diffusion nonlinearities in the diffusion region. The resistor R_s represents the resistance to the ion movement in the diffusion region. The capacitor C_{sh} and resistor R_{sh} represent the shunt and leakage pathways from the insulated electrodes to the tissue. The resistor R_t represents resistance in the electrode from electrode site to electronic interface.

2.1.3 Noise and Interference

The primary reason behind noise associated with electrode-tissue is Brownian motion of electronic, drift and diffusion of charged ions due to concentration gradients, and oxidation/reduction reaction occurring at the electrode/electrolyte interface [24], [25], [26].

Site material, size, surface morphology and contamination of electrode influence the magnitude of the noise. Moreover, there exist additional noise sources which include random fluctuations and instability in the half-cell potential due to the disturbances of the double-layer capacitance and contamination of electrode surface, thermal noise (also referred to as *Johnson* or *Nyquist* noise) as a result of random motion of electrons in the electrode trace, and frequency dependent 1/f noise [27] (also referred to as flicker or pink noise). As a reasonable first approximation these noise sources can be modelled as thermal noise [28] and represented by the voltage source (see Figure 2.2B):

$$v_{elec-ns} = (4kTZ\Delta f)^{0.5} \tag{2.1}$$

where k is *Boltzmann*'s constant, T is Kelvin temperature, Z is electrode magnitude impedance, and Δf is the frequency range of interest.

One of the main disturbances on Biopotential systems is the interference caused by the main alternating current (AC) power line. The interference can be categorized into two kinds and these are electromagnetic interference and electrostatic interference. The alternating main current creates a magnetic field building up an enclosed loop with human body, the leads of the circuit, and the biopotential amplifier. This induces an electromotive force (EMF), which creates an AC potential at the input of the circuit, and

the biopotential amplifier. Decreasing the area of the loop will reduce the electromagnetic interference [**29**]. A miniaturized wearable compact biopo-biopotential acquisition system will further decrease the electromagnetic interference.

Since C_{bp} and C_{iso} have similar capacitance value and R_{gnd} is much smaller than the impedance of C_{bp} and C_{bp} at 50 Hz/60 Hz, thereby creating an AC voltage of the following magnitude can be calculated:

$$V_{CM} = \left(\frac{I_D}{2}\right) R_{gnd} \tag{2.2}$$

provided $R_{el1} \approx R_{el2}$. This voltage V_{CM} appears as a common-mode input to the amplifier, and can be rejected by the amplifiers with high common-mode rejection ratio (CMRR). Although since the input impedance of the electrodes are not exactly same, a differential error signal is created with amplitude:

$$\Delta V_{IN} = V_{CM} \left(\frac{|R_{el1} - R_{el2}|}{Z_{in}}\right) \tag{2.3}$$

where Z_{in} represents the input impedance of the amplifier [27]. So only the amplifier should also have high input impedance along with high CMRR for rejecting electrostatic interference.
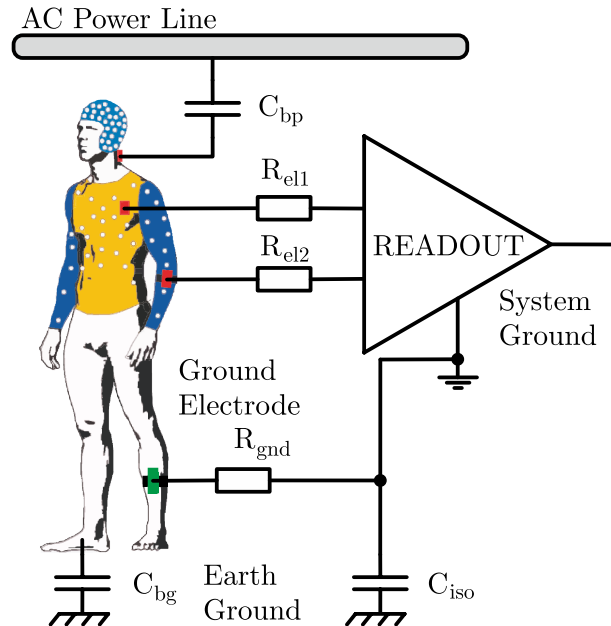
Figure 2.3 Electrostatic interference in terms of capacitive coupling between the main AC power line and human body, and between earth ground and the human body

2.1.4 Biopotential Amplifiers

The main purpose of a biopotential amplifier is to acquire, amplify and filter the extremely weak biopotential signals eradicating common-mode interference, DC electrode offset voltage. Designing of such an amplifier is not trivial. Biopotential amplifier must encounter diverse challenges for extracting biopotential signals. To maintain a long time operation, the power dissipation of the amplifier must be minimized. The following challenges are identified while designing a biopotential amplifier:

- High CMRR to reject interference from mains.
- HPF characteristics for filtering differential DC electrode offset.
- Low-noise for high signal quality.

- Ultra-low power dissipation for long-term power autonomy.
- Configurable gain and filter characteristics that suit the needs of different biopotential signals and different applications.

As shown in the Figure 2.3 the 50-Hz interference and its harmonics appear with the biopotential signal spectrum. So an amplifier is required with a high CMRR in order to reject this common-mode signal. The biopotential amplifier must reject the differential DC offset which orders of magnitude larger than the biopotential signals. A high-pass filter (HPF) is used for this purpose. An ultra-low power amplifier is required to maintain the power autonomy.

2.2 Brain-computer Interface

In the last two decades BCI has emerged as an important research topic in the fields of neuroscience, neural engineering, robotics, medicine, and rehabilitation. The main objective of BCI was to increase human performance e.g. using it as a bio-feedback technique that would improve performance of persons involved in tasks with high mental loads [**30**], augment human performance with direct interface to machine bypassing the muscle activation delay. Recently a few studies have demonstrated the feasibility of BCI usage in enhancing human performance [**30**] [**31**]. They can be categorized into four main paradigms:

a) Motor action paradigm: Since BCI establishes a direct communication between the brain and the control device, the human peripheral nerves and muscles in motor control can be bypassed [**32**]. This allows predicting motoric behavior more rapidly than actual motor reaction time (RT). In one of the recent work, it was shown that evoked EEG potentials in the posterior parietal cortex (PPC)

could be used to predict directions of subsequent reaching or gazing movements [32].

b) Mental-state monitoring paradigm: According to many studies sever-several mental states alertness, arousal, and cognition can be detected [33] [34] from EEG data. By capturing this kind of information in real time from a group of probands in real time, BCI technology can be used to characterize, understand human cognitive states, thus improving human performance through sending warning feedbacks or controlling commands.

c) Visual target detection paradigm: To confirm a detection of target, a manual response is required. P300 is one of such event-related potential (ERP) that signifies brain activities upon elicitation from rare target event.

d) Additional input paradigms: A combination of BCI with traditional input devices (e.g., joystick, mouse, keyboard, etc.) could operate faster while playing a video game. BCIs can provide hands-free interfaces for astronauts to facilitate operations if there is a lack of traditional input methods in the condition with absence of gravity [35].

In the processing of some specific events and triggering neural activity at the scalp, event related brain potentials (ERPs) are found as a manifestation in the EEG. The representing voltages for the ERP are usually quite small relative to the EEG. ERPs are however time-locked events and follow a constant time course, that helps to extract them by averaging multiple trials of eliciting events. After extracting the ERPs, a series of positive and negative deflections are found and are referred as components. The characteristic difference among the successive components is visible in

stimulus rate, amplitude dependence, their topographical distribution, and their relationship to the information processing activities of the brain.

The P300 is a positive deflection that occurs in the scalp recorded EEG after a well-controlled stimulus is applied subject. The well-controlled stimu-stimulus is a part of a specific set of circumstances for eliciting P300 ERP which is known as *Oddball Paradgm* [**36**]. It was first described by *Sutton et al.* in 1965 and has been widely studied since then to explore higher cortical functions in humans. The amplitude of the P300 ERP in an Oddball experiments is usually 10–20 µV. The P300 ERPs occurs normally at a latency of around 300 ms relative to the eliciting stimulus as its name suggests. However its latency may vary from 250 up to 750 ms. The main cause of this variance in latency lies in the fact that P300 is triggered by the decision, not necessarily by consciousness. The decision latency depends on the complexity of decision [**37**]. The P300 based BCI was first introduces in 1988 and a steady growth in the research of such system is observable.

2.3 Time Synchronization

Due to the popularity of low-cost, low-power wireless sensors, they are utilized into forming sensor networks by deploying them in an ad hoc fashion. Those sensors can cooperate to sense, process physical phenomenon and share information wirelessly, thereby creating wireless sensor networks (WSN). Such WSNs [**38**] use time information in various forms while cooperation, e.g. task scheduling, task handling, data fusion, communication. To reduce interference in radio communication a precise allocation of a timeslot in the medium access control (MAC) protocol is maintained with time division multiplexing (TDM) [**39**]. Multimodal sensor data fusion application are required to be adapted to an appropriate duty-cycle in order

to save energy by switching off one of the sensors or the power consuming radio module which is not used continuously [**40**]. For these applications a common notion of time in a network is necessary that bring us to the prob-problem of time synchronization. Safe functioning of a WSN requires stable operation of sensors for extended period of time with real time data processing and transmission under harsh environmental and resource constraints (energy, communication bandwidth, memory capacity).

2.3.1 The Clock Synchronization Problem

In this section the general time synchronization problem in a WSN will be described. A general mathematical model of hardware and software with its parameters clock will be presented. At the end the various sources that are responsible for time delay and uncertainties during a message delivery will be discussed.

Time is a crucial aspect in many applications as described before. Each sensor in a WSN is equipped with a local crystal oscillator. As a consequence of random phase shifts and drift rates of oscillators, the local time of a sensor node in WSN differs from the local time of other sensor node. This induced problems in cooperating task among sensor nodes, correlating data from various sensor nodes, sensor data fusion, etc. Thus time synchronization mechanism is generally employed to cope up with this issue. Time synchronization in a WSN enables the following [**41**]:

a) communication protocols which are based on time-division multiple access

b) coordinated wakeup routines from low-power modes

c) distributed sampling and data correlation

2.3.2 Clocks

The clock of the sensor node has two states which can be modelled differently. The physical state of the hardware clock $H(i)$ can be modelled for a sensor node i that confers a value at time t, and is defined as

$$H_i(t) = \int_{t_0}^{t} h_i(\tau)d\tau + \varphi_i(t_0) \tag{4.1}$$

where $h_i(\tau)$ is the hardware clock rate at time τ and $\varphi_i(t_0)$ is the hardware clock offset at time t_0. Assuming bounded drift of the hardware clock, there exists a constant ρ with $0 \leq \rho < 1$ and such that

$$1 - \rho \leq h(t) \leq 1 + \rho$$

for all times t. This implies that the hardware clock never stops and always increments with at least a rate of $1 - \rho$. As the hardware clock is a crystal oscillator that is used as clock source for a counter register of a µC, the software clock, t_i, can be modelled as:

$$t_i = s_i t + k_i \text{ where } i \in \mathbb{N} \tag{4.2}$$

2.3.3 Sources of Time Delay and Uncertainties in Message Delivery

During the time synchronization mechanism, the participating nodes share their timing information in terms of timestamps with other nodes. To share their timing information each node has to generate their local timestamp according to the crystal oscillator and transmit them via a wireless channel. In this mechanism, a number of non-deterministic delays appear which can

be higher than the required precision of time synchronization. It is therefore required to analyze these delays carefully and compensate them. There are several works in the past that has investigated the source of time delay of a timestamp delivery of which the first introduces by *Kopertz and Ochsen-Ochsenreiter* [**42**], [**43**] and further extended in [**44**] and [**45**]. These can be listed as following:

(a)   *Send Time*—time taken for the generation of the timestamp and for issuing send request to the MAC layer on the transmitter side. This delay is dependent on the system call overhead of the operating system running on that node and is nondeterministic.

(b)   *Access Time*—time required for sender node from waiting to accessing the wireless transmission channel until the point of transmission beginning. It is least deterministic part of the timestamp delivery.

(c)   *Transmission Time*—Time required for the sender to transmit the timestamp. It depends on the length of the message.

(d)   *Propagation Time*—This is the time required for a message from leaving the sender until it's being received by the receiver. The propagation time is deterministic because it dependents only on the distance between two nodes.

(e)   *Reception Time*—Time required for the receiver to receive the message. It is the same as transmission time. The overlap of transmission and reception times is shown in the Figure 2.4.
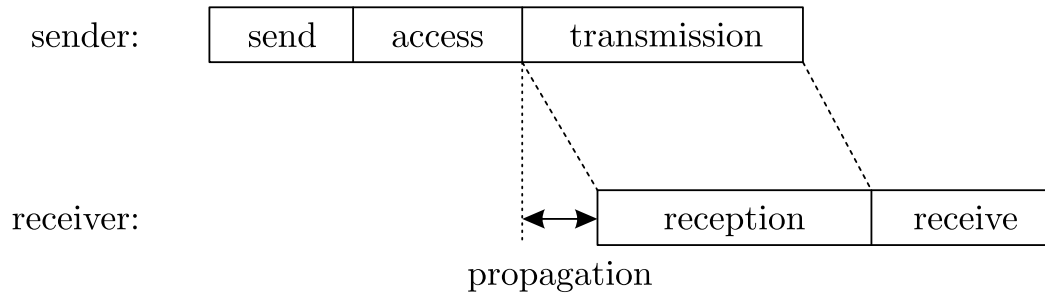
Figure 2.4 Block-diagram of sources of delays during a message delivery

(f)   *Receive Time*—Time required to process the message at the receiver's side and to inform application of the receiver.

Understanding the constituents of time delay and uncertainties in a message delivery, it is required to analyze the entire path of a message delivery from its generation at the sender's side to its processing at the receiver's side. At first the message is transferred to the radio module byte-by-byte. The radio module encodes the transferred message and generates an electromagnetic wave through the antenna. The wave propagates through space and the radio module of the receiver converts it to digital data. The radio module alarms the microcontroller to fetch the data. This constitutes to the following delivery delays at an instantaneous point of time of the message:

(g)   *Interrupt Handling Time*—the time required for the radio module to raise and interrupt until the response from the microcontroller. This time is dependent on the processors load

(h)   *Encoding Time*—the time required for the radio module to encode and transform a message to electromagnetic wave starting from the instant of time when the radio module raised an interrupt to signalize the reception of message from the microcontroller.
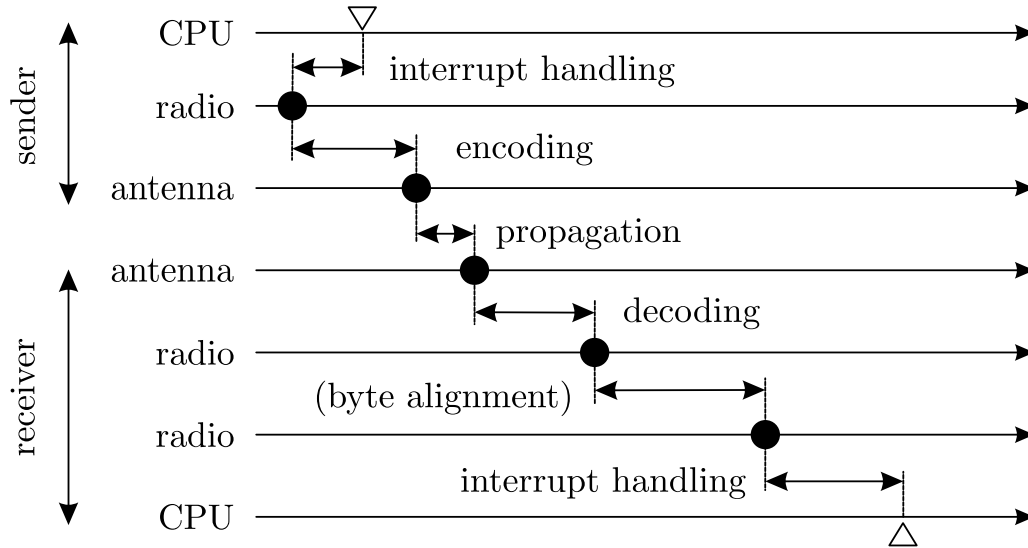
Figure 2.5 A simplified display of the timing of the transmission according to the software (CPU), radio module, and physical layer (antenna) of both sender and the receiver

(i)   *Decoding Time*—the time it is required for the radio module at the receiver to transform and decode the message from electromagnetic wave to digitized data. It ends with interrupt of the radio module signalizing the reception of the reception point.

(j)   *Byte Alignment Time*—the delay is caused due to the different byte alignment of the sender and receiver.

In the Figure 2.5, the decomposition of delivery delay of the idealized point of the message while traversing over a wireless channel is shown. To visualize idealized point of the message, the lines are used for the layer. The dots and triangles represent time instance and timestamps respectively. The timestamp is recorded at the microcontroller according to the interrupts of the radio module for both sender and receiver.

3 Brain-computer Interface

During the first part of the work, a Brain-computer interface consisting of entire biopotential acquisition system hardware as well as its data acquisition software and a SSVEP/AEP stimulator system were developed. In this chapter the design of the biopotential acquisition system and SSVEP/AEP stimulator system will be described from the top level to the bottom level. The complete system architecture of these systems will be presented at first and their components will be described thereafter.

3.1 Bio-potential Acquisition System

In order to cope up with the drawbacks of the state-of-the-art biopotential acquisition system mentioned in the introductory Chapter 1, it was required to develop a design that would provide the following features:

a) Modularity – so that channel density of the biopotential acquisition system can be configured from 8 to 256 channels with an increment of 8 channels. This modularity could be achieved with help of cascading similar system modules

physically. Moreover it should be possible select or deselect a particular channel with the help of software commands.

b)   Miniaturization: As opposed to existing biopotential acquisition systems, the novel system should be miniaturized and flexible so that it could be integrated into a cap for EEG measurement, in a vest for ECG measurement and in a sleeve band to be mounted on head, chest and arm respectively.

c)   Channel Density: 2 cm distance between the channel electrodes, spatial oversampling

d)   Dry active sensors, eradicate the usage of conductive electrolyte gel

e)   Mobility, Wireless Data Transmission

f)   Flexible electronics – encapsulation in a cap, vest, arm band

3.1.1 Complete Architecture of ExG-system
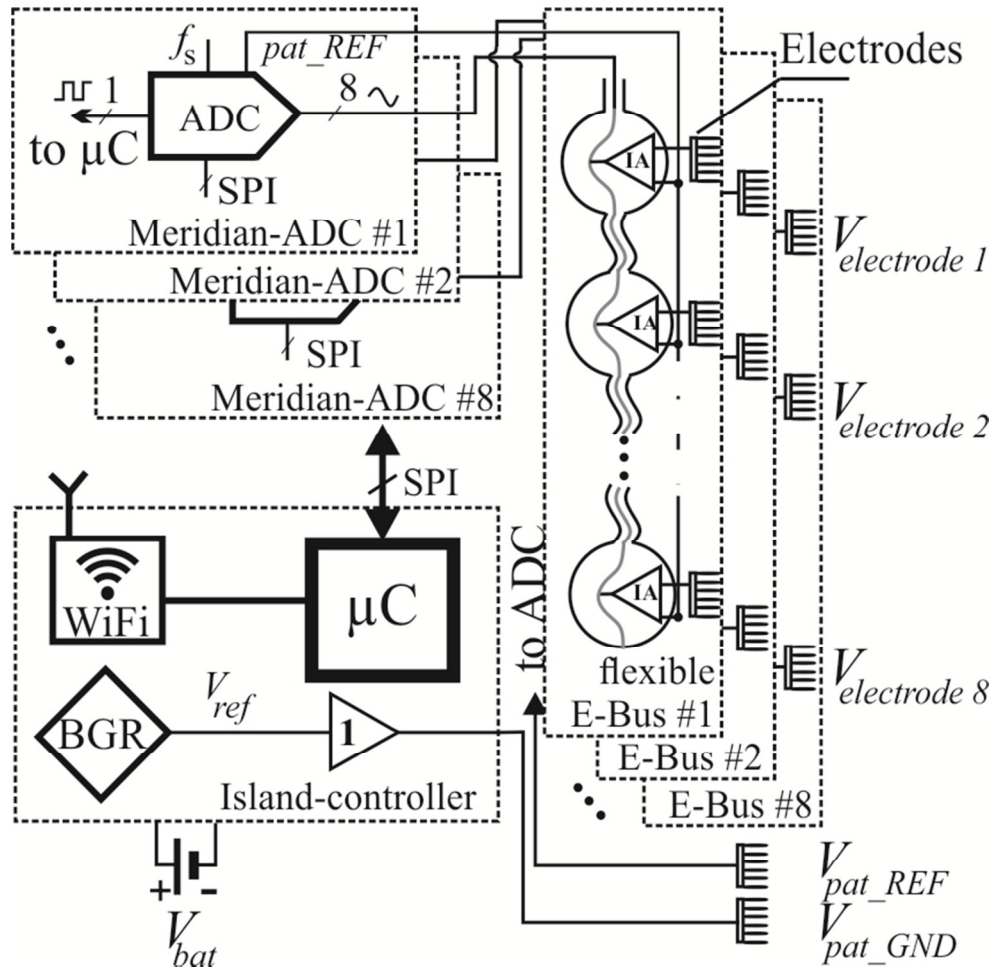
Figure 3.1 Detailed signal-processing architecture of the ExG-system; starting from the analog bio-potential acquisition to its digitalization and transmission of the data wirelessly via WiFi module; BGR states the band-gap reference voltage and V_{pat_REF}, V_{pat_GND} refer to the reference electrode and patient's reference electrode respectively

In the above Figure 3.1, the complete architecture of biopotential acquisition system is presented. This system is capable of recording EEG, ECG, EMG (combined ExG) from the surface of the human body. It has three main signal processing layers starting from the contact to surface of human skin or

scalp to the digitalized data transmission over a wireless link. The main three layers are:

a) Electrode-bus , b) Meridian-ADC, c) Island-controller

3.1.2 Electrode-bus

The first part of the biopotential signal processing chain was to amplify and filter the extremely weak (see Table 1-I) biopotential signals. In this pre-amplification stage, the bio-potentials from the surface of the skin were to be amplified directly on the measurement point. This prevents the signals to travel a long path through the wires susceptible to the environmental noise what is done in conventional biopotential measurement techniques. On each measurement point a dry electrode was placed. This close proximity of the amplifier to the skin reduces the electromagnetic interference (EMI) and mechanical disturbance on the wires carrying the bio-potentials.
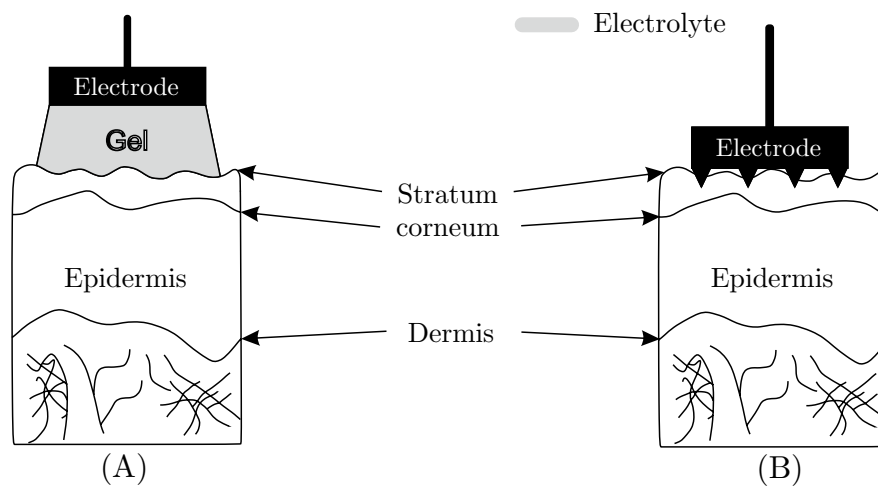
Figure 3.2 Application of biopotential electrodes: (A):standard EEG wet electrode and (B):dry EEG electrode

These kind of dry electrodes reduce the preparation time for 32 standard EEG electrodes from 45 minutes (which is case of using Ag/AgCl electrode) to 5 minutes [46]. On one hand, in traditional measurement technique with wet electrode an electrolyte gel was used to reduce the impedance of each electrode. This gel helped to bypass *stratum corneum* isolation properties as illustrated in the Figure 3.2, thereby reducing unwanted noise in the recording. On the other hand, dry electrodes with pins that are able to penetrate the outer skin layer (stratum corneum) and directly interface to the electrolyte fluids of living epidermis are of great importance (see Figure 3.2) since they can achieve better signal quality than that of wet electrodes. A novel dry electrode which acts as the analog sensor to measure the biopotential signals directly from *epidermis* was designed and fabricated. The mechanical design layout of the electrode is shown in the Figure 3.3. An array of 19 gold-pins as shown in the Figure 3.4 is tied together in a circular area which is made of FR-4 epoxy/glass laminates [47] to design an electrode.

This Pins are cut on one side after assembly except these three pins that can be soldered electronics PCB which must be designed accordingly
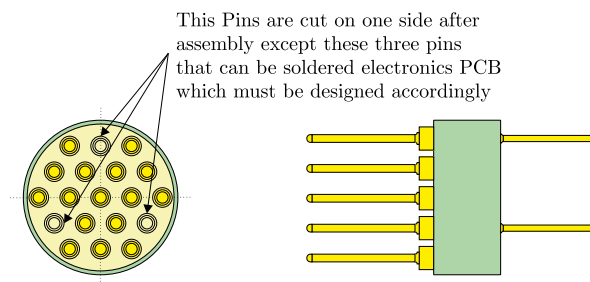
Figure 3.3 Mechanical design drawing of the dry electrode array
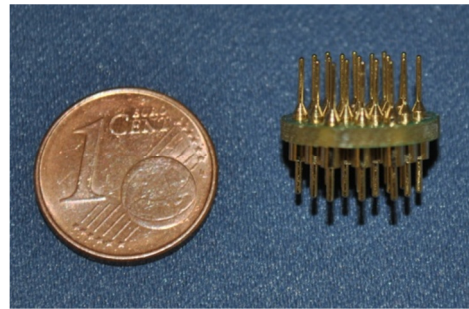
Figure 3.4 Dry electrode after production with 19 golden pin-array and euro-cent on the left as a comparison

The most suitable amplifier that satisfies the requirement as mentioned in the Section 2 of the Chapter 2 where the theoretical details concerning biopontential signals, electrode, and amplifier were discussed, is an instrument amplifier (INA).

The choice of an INA was due to the following reasons:

1. It has a high input impedance which is $1\,\text{G}\Omega$ that allows low polarizing input currents (below 200 pA)

2. Low input noise $50\,\text{nV}/\sqrt{Hz}$

3. High common-mode rejection (100 dB at $G \geq 100$)

4. Extended input common-mode range to avoid saturation while preserving overall gain at the maximum value.

Considering these specifications of three difference kinds of INAs, *INA333* [48], *INA331* [49], from *Texas Instruments Incorporated* (TI) and *AD8222* [50] from *Analog Devices, Inc.* (AD) were selected to design 6 different active electrode prototypes as shown in the Figure 3.5. Since these electronics were directly placed directly on the top of the electrode and powered, these were called active electrodes.
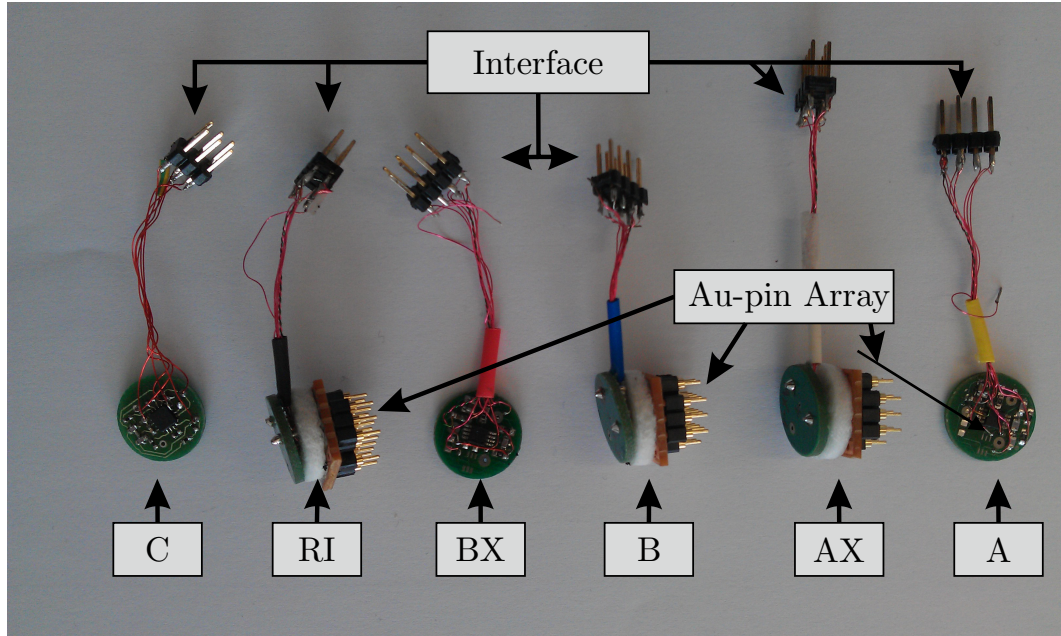
Figure 3.5 Active electrodes with different variations of IA and amplification factors which were designed and tested. Each of the variation has its name which is described in Table 3-I.

The six varieties of the manufactured INA prototypes are listed in the Table 3-I.

The listed active electrodes were tested with an EEG Amplifier namely $EEGO^{TM}$ from eemagine *Medical Imaging Solutions GmbH*, Germany [**51**]. These tests were carried out to evaluate performance of the prototypes in terms of their current consumption, system resolution to determine the best suited INA for the design of active Electrode-bus. The prototypes showed a root mean square (RMS) value of input noise in the range of 1-3 μV_{RMS}. Using the new selection of INAs, the current consumption was observed to have minimized with respect to the existing active electrodes in the EEGO

amplifier. This has helped in determining the suitable INA so that they could be used for mobile usage in home monitoring scenario.

Table 3-I Overview of first INA prototypes tested in the design phase of the active electrodes

Name of Variation	Type of Electrode	INA Type	Amplification Factor	No of Tested Prototypes
A	Active	INA331	5	10
AX	Active	INA331	2,5	10
B	Active	INA333	5	10
BX	Active	INA333	2,5	10
RI	Reference	INA333	1	10
C	Active	AD8222	1	5

There were three different types of electrodes used for biopotential acquisition and they are signal electrode, reference electrode, patient's reference. Each of them has the same structure as shown in the Figure 3.5. The signal electrodes are to be placed e.g. for an EEG measurement according to international 10−20 system [52]. The INA was positioned directly on the dry electrode-array, amplified the differential signal between the signal electrode and reference electrode as shown in the Figure 3.7.
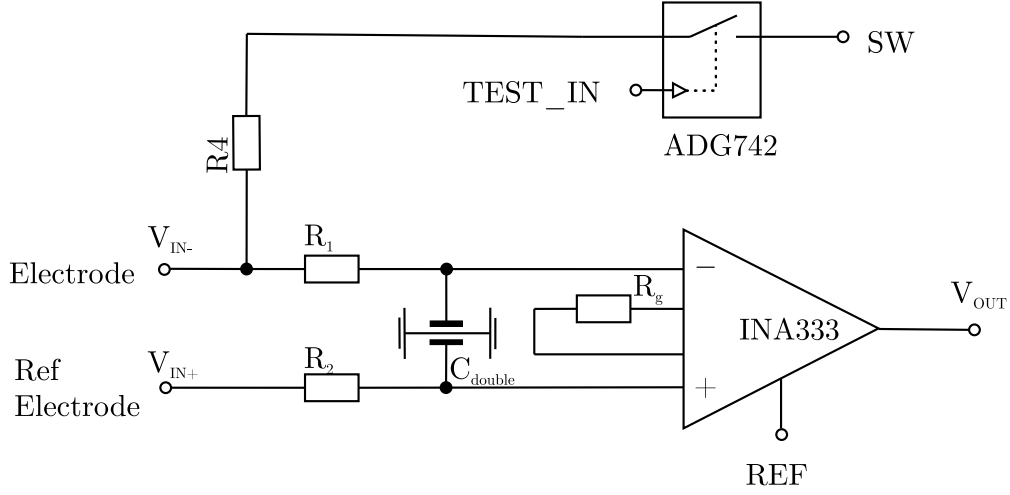
Figure 3.6 First amplification stage of differentially measured biopotential with INA, A low-pass filter for rejecting RFI using R_1, R_2 and C_{double}; R_g is responsible for setting the gain of the first amplification stage. A separate switch using ADG742 for impedance measurement option

Due to the lowest noise among the six tested INAs, *INA333* was chosen for this purpose. To eliminate the radio frequency interference (RFI) from the environment a RF filter with a bandwidth of approximately 1.5 MHz were used at the input of each electrode.

$$V_{out} = (1 + 100k\Omega/R_G)(V_{IN-} - V_{IN+}) \tag{3.1}$$

In the Figure 3.6 a channel of the biopotential acquisition system is displayed where it consists of a pair of electrodes, and an INA measures the difference between two electrodes.

To remove the DC part of from the biopotential signals an active high-pass filter was implemented at the output stage after the first amplification and thereby allowing only a small in the range of 1 mV or below through the analog signal processing chain, named as Electrode-bus.

Solder stop

FLEX Polyimide layer with
solder mask coverage:
No vias in flex section

Stiffener for
FFC-FPC connector

No flow under filler

Separate 1 layer PCB
with press fit Au pins

active and passive SMD
components
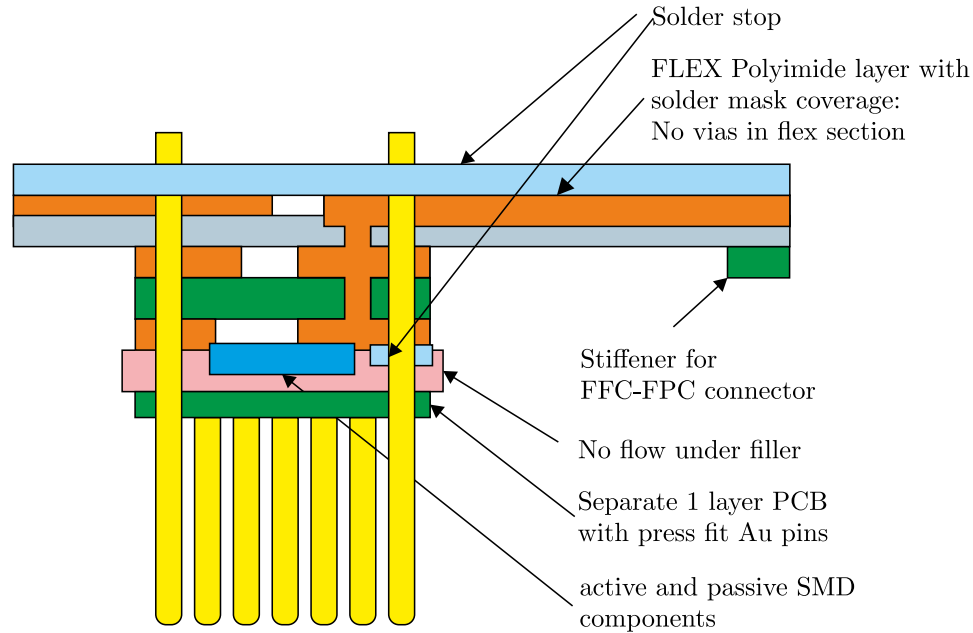
Figure 3.7 Conceptual sketch of the dry electrode in connection with the amplification circuitry and flexible bus

Since the chosen analog-to-digital converter (ADC) has eight channels, it was required to design an Electrode-bus containing eight channel electrodes numbering one to eight. There was a huge challenge in the assembly and connection technique of a flat and flexible bus containing those eight active electrodes so that those can be encapsulated in a cap, vest or in an arm band for mobile acquisition of EEG, ECG and EMG potentials. A novel Electrode-bus was designed for this purpose as shown in the Figure 3.7. The design employed the rigid-flex printed circuit board (PCB) manufacturing technique.
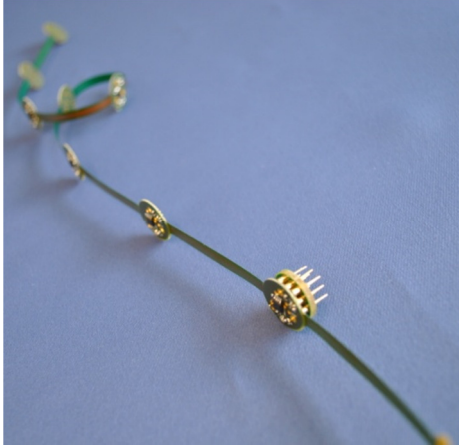
Figure 3.8 A flexible, flat electrode-bus containing 8 active electrodes
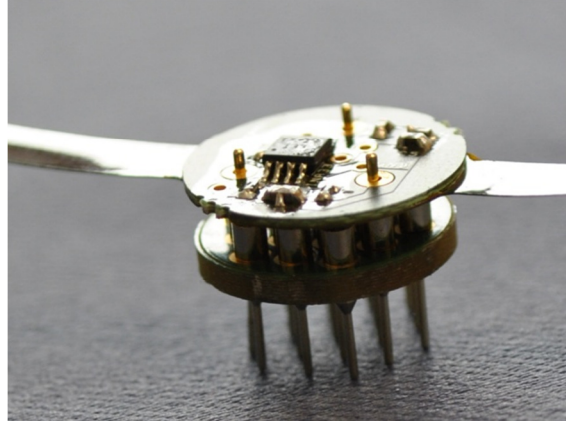
Figure 3.9 Single active electrode with a IA circuitry on the top

The flexible bus was kept flexible and the electronics were placed on the rigid part as shown in the Figure 3.8 and in the Figure 3.9.

3.1.3 Meridian-ADC

In this part of the signal processing chain, the differentially amplified signal from INA was digitized with the help of a delta-sigma ADC from TI. The choice of the ADC was for the following reasons:

a) High signal resolution of 24-bit

b) Low input referred noise of 4 µV (*ADS1298* [**53**]) and 1 µV (*ADS1299* [**54**]) in the bandwidth of 1 Hz−10 Hz

c) Σ-Δ modulator based ADC architecture causing low noise

d) Differential input with inbuilt radio frequency interference (RFI) filter

e) High simultaneous sampling rate up to 32 kSPS (ADS1298) and 16 kSPS (ADS1299)

f) Programmable gain: 1, 2, 4, 6, 8, 12, or 24

g) Input bias current: 300 pA

h) Low Power: 5 mW/channel (ADS1298), 41 mW/channel (ADS1299)

i) Serial peripheral interface (SPI) bus for data transfer to a µC with 2 MHz

For this purpose a separate unit of PCB belonging to the 2nd part of signal processing chain of biopotential acquisition system was designed. It was named *Meridian-ADC* since it was to be placed on the meridian of the human head.

The reference electrode was connected to this unit so that it can be passed through each of the signal electrode on electrode-bus. The interface to the electrode bus was realized with zero-insertion force (ZIF) connector for mechanical flexibility and miniaturized size. This also guaranteed a suitable encapsulation in combination with the Electrode-bus in a textile. The design of Meridian-ADC allowed the Electrode-bus to be placed on the both sides and can be trimmed from both sides to achieve an eight channel density as shown in the Figure 3.10.
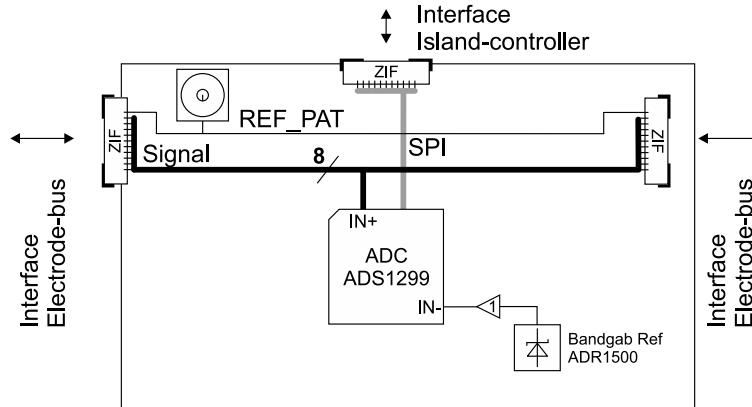
Figure 3.10 Top Level Design of Meridian-ADC

The design of Meridian-ADC was realized in a 4-layer PCB manufacturing technology and the manufactured PCB resulted in the dimension of (width x breadth x height) 32.5 x 22.5 x 1.2 mm^3.
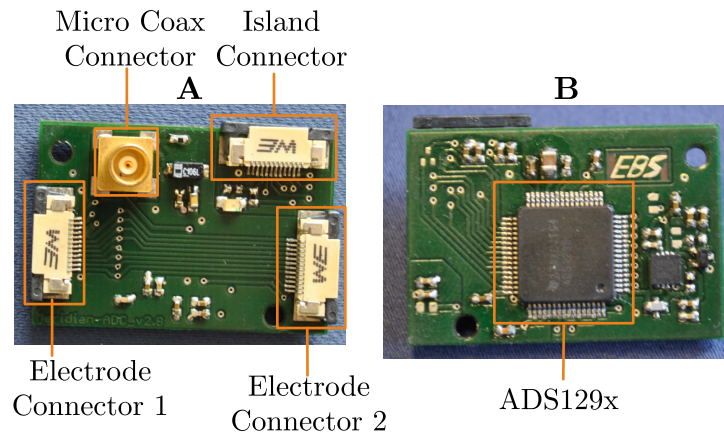
Figure 3.11 Manufactured PCB prototype of the Meridian-ADC; A) Top side of the Meridian-ADC with 2 ZIF connecters for connecting Electrode-busses, a shielded micro coax connected for reference electrode input; B) Bottom side of the Meridian-ADc with the ADC, ADS129x (x = 8,9)

The characteristic of the manufactured Meridian-ADC is listed in the Table 3-II.

Table 3-II Specifications of the developed Meridian-ADC

Parameter	Min	Typ	Max	Unit
Analog-Digital-Converter				
Number of Electrodes			8	
Resolution			24	Bit
Data Interface (SPI)				
Transfer Rate			2	MHz
Measurement Range				
Input Voltage Range	0	1.2875	2.575	V
Reference Voltage		1.2875		V
LSB		0.1535		µV

3.1.3.1 Band-gap Reference

To generate the patient's reference at the Meridian-ADC, a band-gap reference voltage (BGR) was chosen due its low noise feature. After a thorough research over the available voltage reference *ADR1500* [**50**] from ADI appeared as the best candidate for the application due to its 5.0 µV$_{RMS}$ noise level in the frequency band ranging from 0.1 Hz to 10 Hz and an ultra-low current consumption of 50 µA.

3.1.4 Island-controller

In this section the Island-controller will be described. At first the hardware design of Island-controller including analog and digital part will be described.

After that in the software part the development of firmware of the Island-controller for data acquisition and command parsing will be discussed.

3.1.4.1 Hardware

The last part of the signal processing chain was the *Island-controller*. In this unit the digitized signals from Meridian-ADC were acquired using the SPI interface of the Island-controller. It was designed in away so that eight Meridian-ADCs can be connected to it via 4 different SPI buses. Each SPI bus connects two Meridian-ADCs to the Island-controller as shown in concept block diagram in the Figure 3.12. Since each Meridian-ADC is connected to an Electrode-bus containing eight electrodes, 64 channels of signal electrode configuration is possible in the full configuration of Island-Controller. After data acquisition, the data were transmitted to a remote signal processing personal computer (PC) with the help of WiFi. The data was handles with the Transmission Control Protocol/Internet Protocol (TCP/IP) protocol where the Island-configures as a client and PC as server. The Island-controller acted as a main controller (MASTER) in the ExG-system which initiated and stopped biopotential data measurement cycles. The remote signal processing PC sent remote commands over air via using WiFi to the Island-controller which is in the same local area network IEEE 802.11 standard [55]. Island-controller handled the request and deployed respective routines. The device was powered with a 4.2 V (3.7 V nominal voltage) Lithium Polymer battery. The reference voltage 1.287 V for buffering the proband for a biopotential measurement was generated at the Island-controller using a low-noise voltage reference *ADR1500* from ADI.
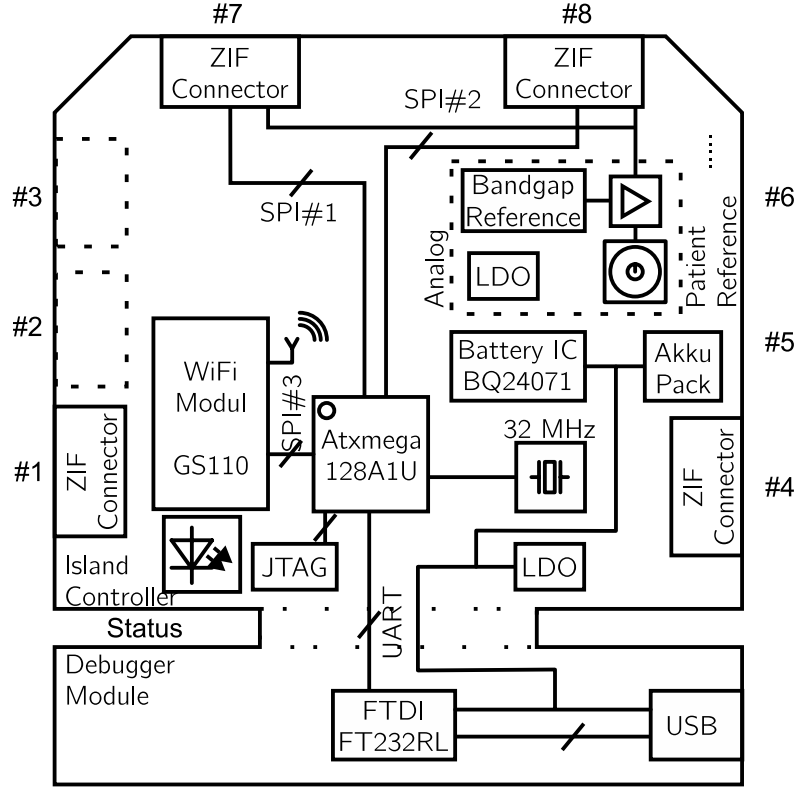
Figure 3.12 Concept diagram of the Island-controller with 8 ZIF connectors for connecting 8 Meridian-ADCs, a AVR XMEGA controller, a WiFi module, power management circuitry and necessary debug interfaces (JTAG, USB)

Since there is no fixed potential in the measurement technique, the proband needs to be buffered to a potential close to the half of system operating voltage i.e Vcc/2. This allowed utilizing the full dynamic range $(\pm\frac{V_{cc}}{2*G})$ where G $(=1+\frac{100k\Omega}{R_g})$ is the gain of INA for the measurement. For that purpose a band-gap voltage reference $ADR1500$ from ADI were chosen. It generates an accurate 1.2875 V output.

The manufactured Island-controller achieved a dimension (width x breadth x height) of 35.4 x 55.7 x 5.65 mm^3.
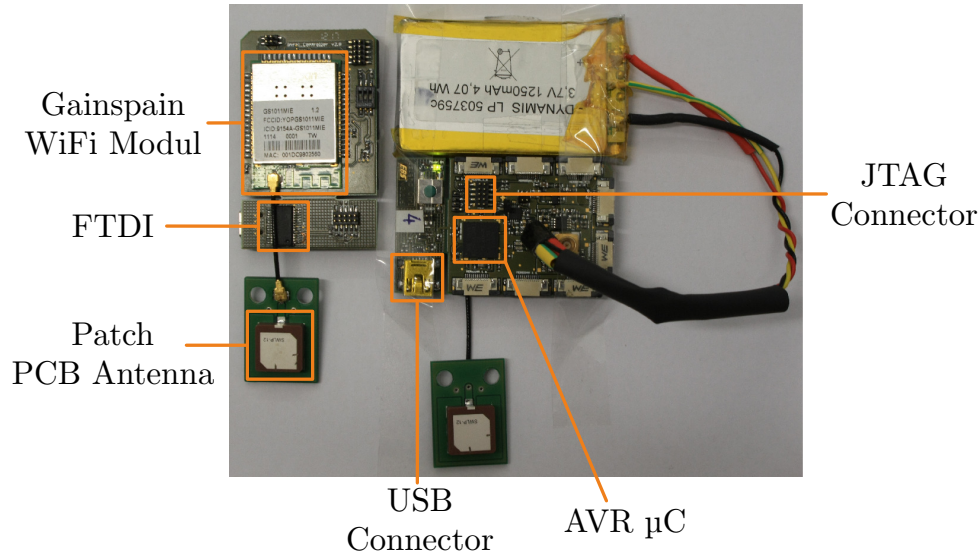
Figure 3.13 The first prototype of Island-controller. It is powered with a LiPo-Battery and the external patch antenna is connected through miniature coaxial RF connector

In the digital part of the Island-controller, an AVR microcontroller (µC) from Atmel from XMEGA family, the ATxmeata128A1 [**56**] was the heart of the system. It was triggered to an external crystal clock of 16 MHz with ±20 ppm accuracy. However an operating frequency of 32 MHz was achieved with the help of the inbuilt phased locked loop (PLL) of the µC. With a typical current consumption of ~18.5 mA, availability of four serial peripheral interfaces (SPIs), eight universal asynchronous receiver/transmitter (USART) interfaces, and 128 Kbytes of in-system self-programmable flash memory, it appeared as a suitable candidate for design of Island-controller. Two SPI busses were used to connect the eight Meridian-ADCs each connecting four of them as shown in the Figure 3.14. The speed of SPI was set to its maximum of 2 MHz. As mentioned in the Table 3-III, the ADS1299 can be sampled from 250 Hz up to 1 kHz. For wireless data transmission, a WiFi module from Gainspan namely *GS1011* [**57**] with external was chosen

and it communicated over a SPI bus with the μC. For the selection of the WLAN module data traffic estimation based of the sample rate of the ADS1298 was calculated and shown in the Table 3-III.

Table 3-III Data traffic estimation for the selection of radio module

Sample Rate [Hz]	Data Throughoutput [Mbps]
250	0.38
500	0.77
1000	1.54

The choice of a WiFi module was mainly because of the high data throughput of 1.54 Mbps for 64 channels Island-controller. This amount of data was only able to be handled with a WiFi module. Moreover WiFi uses the 802.11 radio, 2.4 GHz carrier frequency, seamless integration with existing 802.11b/g infrastructure that supports the basic requirement of medical device certification according to IEC 60601 [58] as well as to be used as an Internet-of-Things (IoT) [59] or telemedicine product [60].

3.1.4.2 Software

In this section, the firmware development for the biopotential data acquisition using the ExG-system will be described. The firmware was specified to execute the following functions:

a) Initialize all the interfaces for all attached Meridian-ADCs, WiFi-module, timers, UART bus for debug output

b) Automatic detection of the number of attached Meridian-ADC

c) Successful connection with an access point (AP) with WiFi module

d) Seven main working modes realized in states

e) A debug output for failure check

f) Optimized for data acquisition (DAQ) and data transmission

g) A kernel for managing commands via air according to IEEE 802.11b/g

   a) Setting the sampling frequency (125 Hz, 250 Hz, 500 Hz or 1 kHz) by the user

   b) Setting the internal gain of the ADS1298 of Meridian-ADC for various working modes

   c) Setting the ADS1299 for short-circuit test, putting test signal on the channels of ADS1299, turning on/off of each channel of ADS1299

   d) Setting parameters of the WiFi-modules e.g. SSID, IP, Netmask, Channel, PSK-passphrase, MAC address

h) Real-time operating system using optimized register settings

With the described specifications, the following finite state machine in the firmware was designed. The firmware was named as *HD-ExG_ OS_ v_ x.y* where *v, x, y* represent the versioning of the firmware. The firmware was realizes as a finite state machine (FSM). The state-diagram in the Figure 3.14 describes the states of the FSM and how they migrate from one state to another.
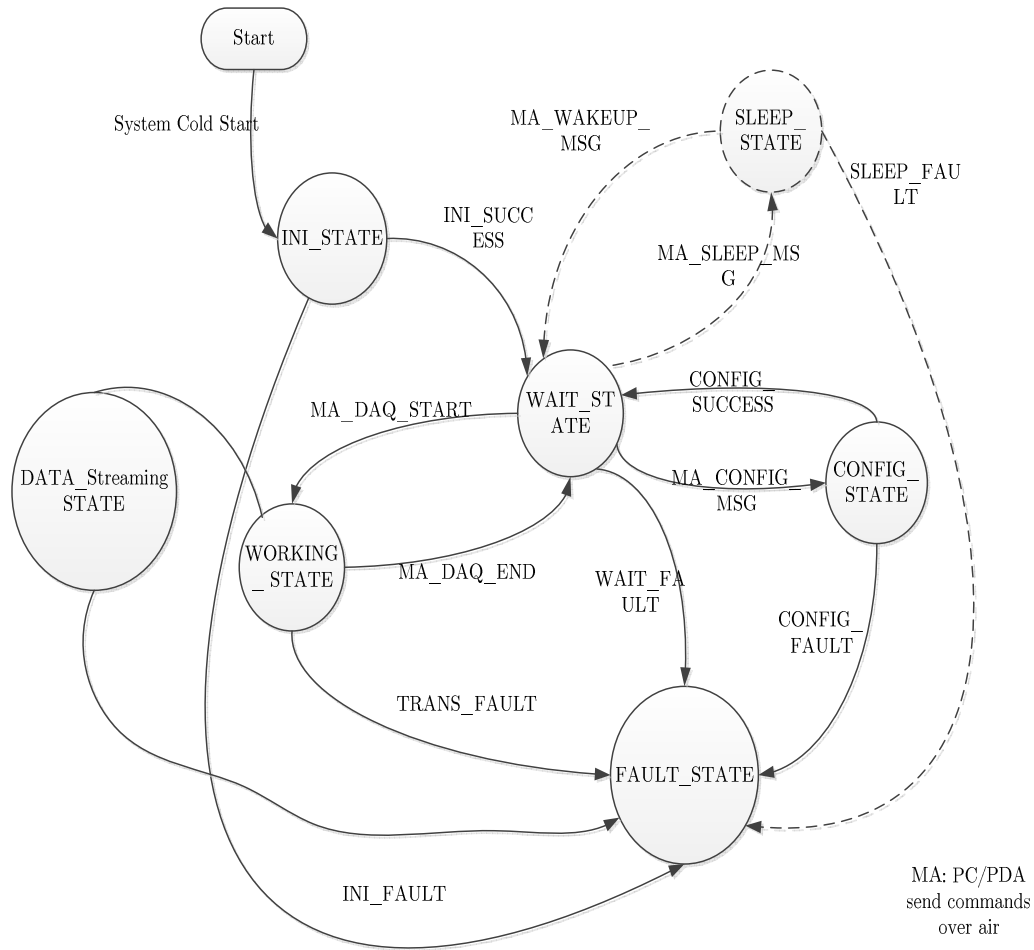
Figure 3.14 State-diagram of the firmware for the Island-controller with seven main states and their interaction

In the state-diagram of the Island-controller seven main states;

    a) Initialization State (INI_STATE),

    b) Wait for Command State (WAIT_STATE),

    c) Configuration State (CONFIG_STATE),

    d) Working State (WORK_STATE),

e) Data Streaming State (DATA_STREAMING_STATE), and

f) Fault State (FAULT_STATE).
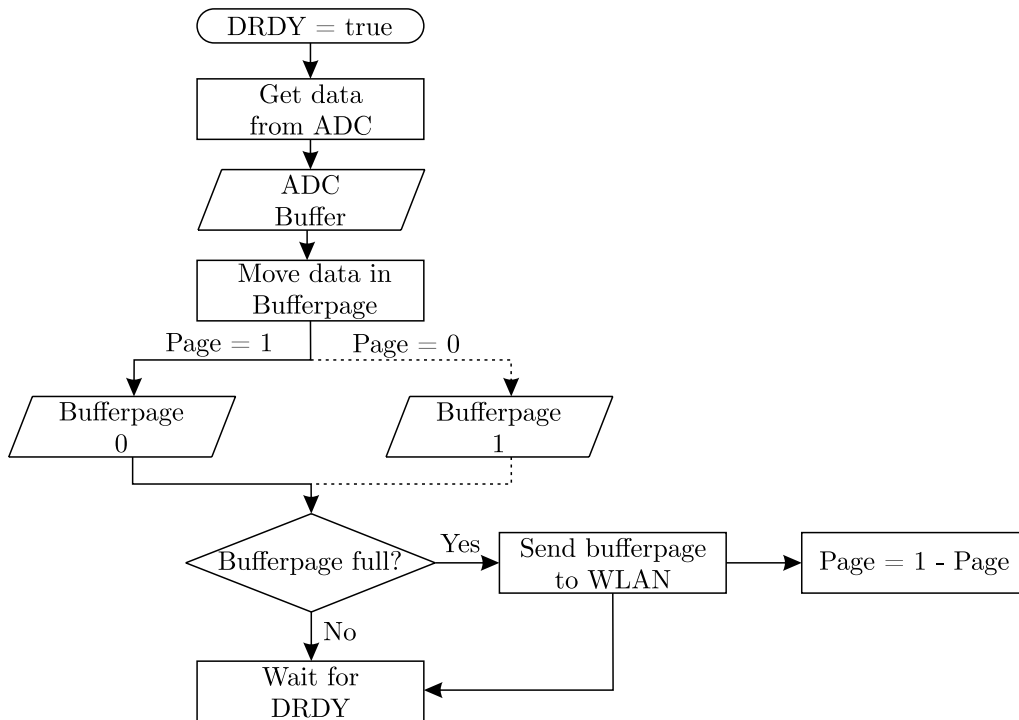
Figure 3.15 Flow-diagram of the implementation of the data acquisition from Meridian-ADC using the Island-controller.

After system cold-start, the firmware let the Island-controller to go to the INI_STATE where all the necessary peripheries were initialized. After that it went to the WAIT_STATE and wait for commands from the remote PC controlling the measurements. As per commands from the controlling PC, it executed the necessary routine either in CONFIG_STATE or went to WORKING_STATE to start data acquisition (DAQ) from the attached Meridian-ADCs. The DAQ is triggered by a data ready interrupt from ADS1299 of the Meridian-ADC and used a double-buffering technique so at

a time only a buffer is busy reading or writing to the WiFi buffer as shown
in the Figure 3.15.

To speed up the copy process between the buffers, the direct memory
access (DMA) of the XMEGA controller was used. This worked in parallel
with other CPU processing and does only incur 20 % of load. The working of
principle of the DMA is displayed in the Figure 3.16.
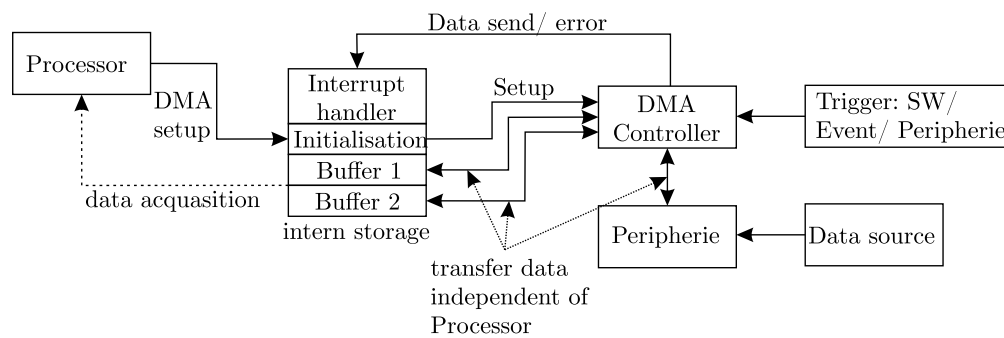
Figure 3.16 Working principle of the DMA in XMEGA

In order to analyze the measured data, it was required to define a structure
of the data in which it should be acquired and sent out via WiFi to a per-
sonal computer (PC). In the Figure 3.17, the structure of measured data is
described
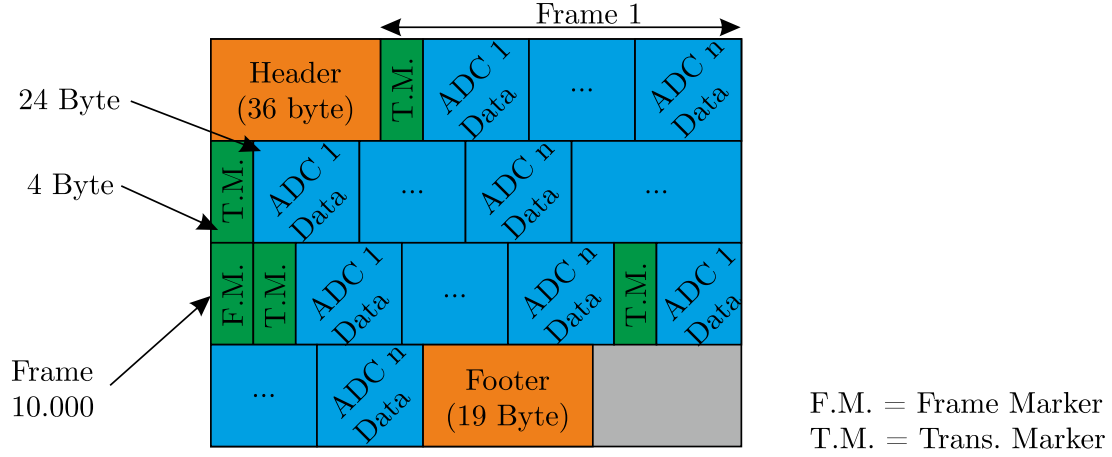
Figure 3.17 Architecture of the measured data stream in which the recorded data from Meridian-ADC was first stored at the Island-controller and then transmitted wirlessly to a remote PC

Every measurement cycle started with a *Transmission Header (Header* in the above Figure 3.16*)* consisting of 36-byte of data. The detail description of each of the parts of the data architecture will be included in the Appendix. A unique *Transmission Marker* consisting of 4 Bytes was defined which precede every measurement data frame. At the end of a measurement session, *Transmission Footer (Footer* in the Figure 3.16*)* of 19-byte length was added to the data stream which includes information about end of measurement, number of samples, timestamp and a checksum. This helped further to plot, analyze, and post-process of the data using MATLAB [61].

3.1.5 Experimental Verification

In order to validate the developed ExG-system [62], it was required to experimentally test for usability, reliability, raw signal quality, capability of measuring biopotential signals.
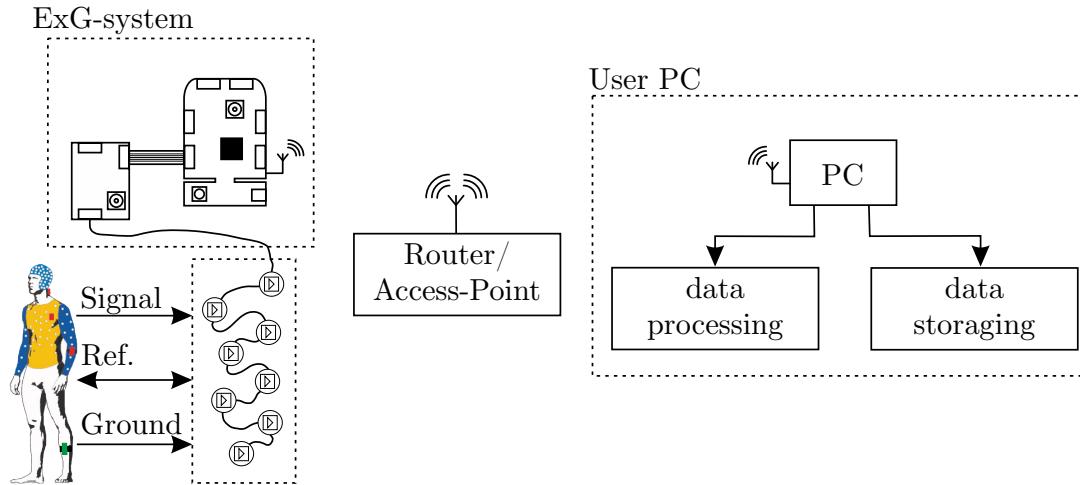
ExG-system

Figure 3.18 A generic view of the biopotential measurement setup in a local area network where a proband wore a ExG-system, a remote user PC transmited commands and received data from the ExG-system via Access-Point (AP)

Moreover the system required to be characterized of system resolution, maximum detectable frequency, maximum signal amplification, maximum wireless data transmission bandwidth, and range. For this purpose several measurements with various experimental setups were executed to test for reliability and reproducibility of the system. The gain of the analog signal processing chain was determined with a calibration test. In this test an input sinus signal with 30 mVpeak-to-peak and 15 Hz was fed into each INA of the Electrode-bus with a signal generator. The digitized data of the signal was reconstructed with MATLAB to generate an exact sinus signal of the same amplitude (30 mV) and frequency (15 Hz). For that a factor, called calibration factor each channel on the Electrode-bus was determined. The measurement setup is schematically presented in the Figure 3.19.
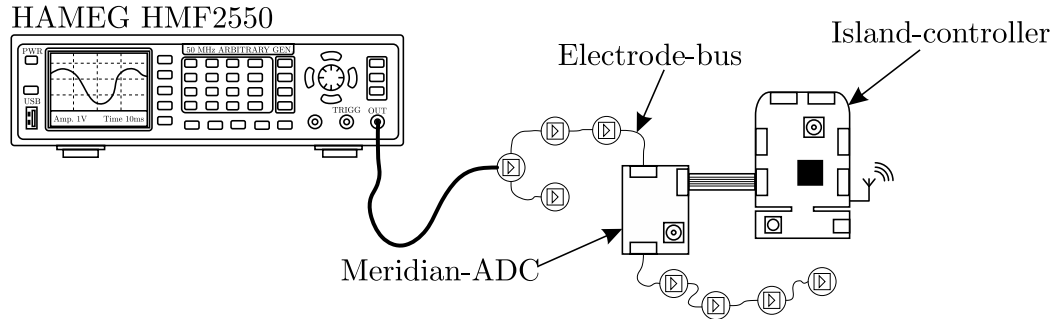
Figure 3.19 Measurement setup for calibration test where the signal (AC) was generated on a signal generator (HAMEG *HMF2550*) and was fed to the differential inputs of the INA. After the signal was passed through the entire signal processing chain of ExG-system, the input signal was to be reconstructed.

It will be required further to determine the system resolution with the help of short-circuit test as well as analyzing measurement result of biopotential tests.
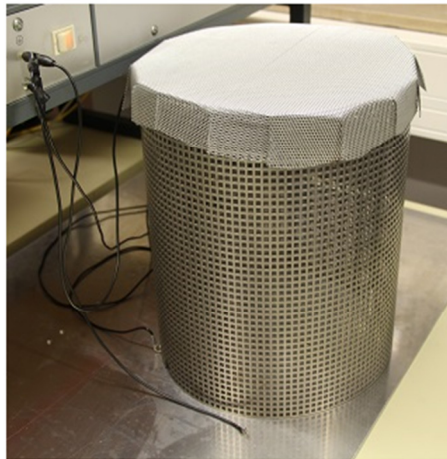
Figure 3.20 Faraday cage for short-circuit test (height: 37 cm, diameter: 32.5 cm)

The short-circuit test was required to evaluate the minimum measureable voltage or the system resolution. If the inputs of the INA were to the same potential, then there will be ideally no voltage at the output of the INA. In

this test the output voltage then refers as the system noise or system resolu-
tion as this is minimum voltage which can be measured with the developed
ExG-system. The Figure 3.20 describes the experimental setup of the test in
which a Faraday cage was built to shield against the electromagnetic waves
as well as 50-Hz noise from main AC.

After completion of these basic tests and identifying the calibration factor
(C_f) and system resolution with short-circuit test, the system was required to
be tested for real biopotential measurements on probands. For these purpose
the EEG, ECG measurement scenario was conceptualized. For ECG meas-
urement the signal electrodes were placed at the bottom of the left wrist and
reference and patient's reference were placed at the bottom of the right wrist
to form a simplified version of *Eindhoven* triangle [63]. For EEG measure-
ment, the electrodes were positioned according to the international $10-20$
system.

3.1.6 Experimental Results

In the section the results from the above mentioned experiments will be
shown and discussed. At first the system was calibrated with the measure-
ment set-up shown in the Figure 3.19. After that a short-circuit measure-
ment were performed to find out the system resolution. During the short-
circuit measurement, the inputs of the INA were tied together with BGR so
that only input system noise at the output of the INA could be measured.
Thereafter the ExG-system was utilized to record biopotential data (ECG,
EEG) from a human body. The corresponding visualization of the measured
raw biopotential data without any further processing is plotted in the Figure
3.23 and in the Figure 3.24.
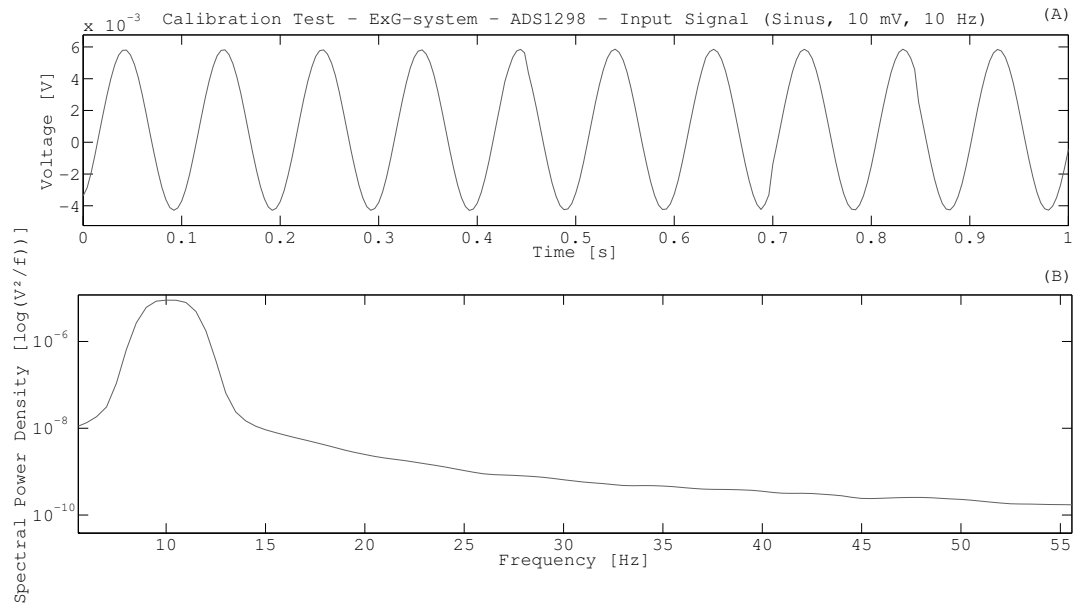
Figure 3.21 Calibration test with sinus signal. A) showing measured voltage over time and B) showing the power spectrum in frequency domain

The calibration test results are shown in the Figure 3.21 where the input sinus signal was reconstructed after its digitized data was received at the remote PC. The same sinus signal as it was fed into the inputs of the INA could be reconstructed with 10 mV amplitude and 10 Hz of frequency. Furthermore there were no 50-Hz coupled noise from the main AC was visible in the power spectral density (PSD) plot in frequency domain.
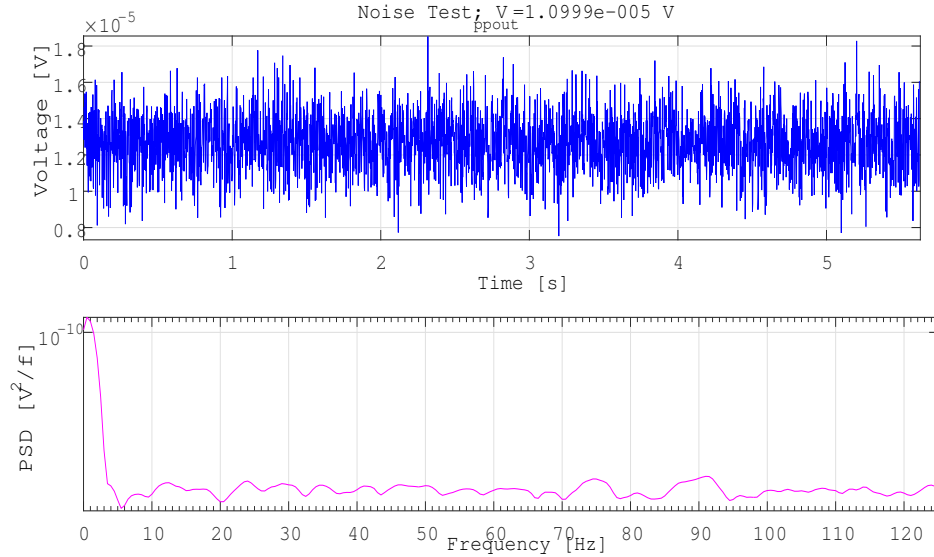
Figure 3.22 Short-circuit test; (A) showing the white noise in time domain and (B) showing the corresponding power spectral density (PSD) amplitude in frequency domain

The noise test results are shown in the Figure 3.22 where the system noise was reconstructed after its digitized data was received at the remote PC. The magnitude input noise was measured as 10 µVpeak-to-peak between 0.1 Hz-125 Hz. Furthermore there were no 50-Hz coupled noise from the main AC was visible in the PSD plot in frequency domain.
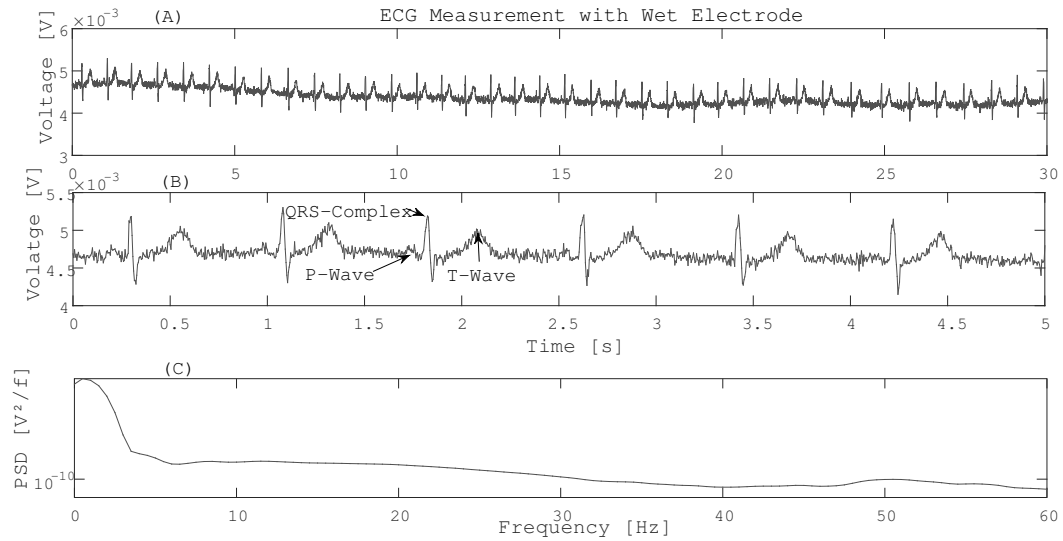
Figure 3.23 Raw data ECG measurement from a proband; A) a time span of 30 s, b) a time slot until 5s to visualize the QRS-complex, P-wave, T-wave, c) corresponding power spectrum in frequency domain. The frequency spectrum shows that the measured signal did not capture any surrounding 50-Hz noise from the main due the high CMRR of the INA.
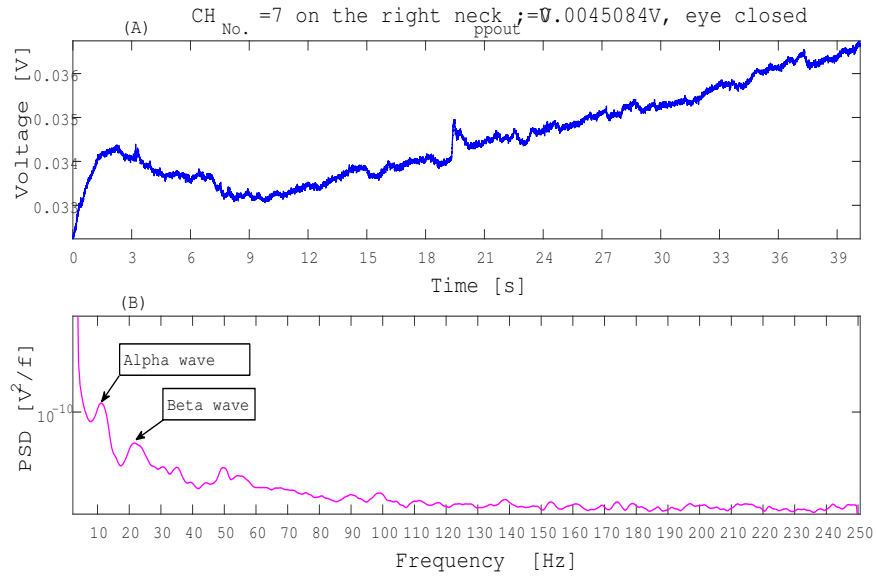
Figure 3.24 (A) Visualization of raw data from an EEG measurement on a proband in time domain and (B) Alpha and Beta rhythm. The signal electrode was placed on the right side of the neck of the proband's head, the reference electrode behind the left ear and the patient's reference electrode behind right ear. The power spectrum (PSD) of the blocks of data reveals that the power near 10Hz and 20Hz shows two peaks, commonly known as alpha and beta rhythm.

3.1.7 Multichannel ExG-system Test

To evaluate if the ExG-system was capable of measuring sixty four channels of electrodes from eight Meridian-ADCs, six different measurements by varying the number of Meridian-ADCs from one to six were performed.

Table 3-IV Data loss of a ExG-system at different settings of sample and number of Median-ADCs

Sample Rate [Hz]	No. of Meridian-ADCs	No. of Channels	Data Loss [%]
250	1	8	0,013
500	1	8	0,032
1000	1	8	12,968
250	2	16	0,03
500	2	16	0,03
1000	2	16	49,72
250	3	24	0,01
500	3	24	24,64
1000	3	24	67,83
250	4	32	0,06
500	4	32	45,53
1000	4	32	81,95
250	5	40	0,07
500	5	40	57,58
1000	5	40	82,24
250	6	48	0,85
500	6	48	74,32
1000	6	48	88,40

To compute the data loss [in %] the following mathematical relation in equation 3.1 was taken into account:

$$d_l[\%] = \frac{(F \times (24 \times N_M + 4) + (M \times 4) + 36 + 19) - d_r}{F \times (24 \times N_M + 4) + (M \times 4) + 36 + 19} \times 100 \qquad (3.1)$$

In equation 3.1 d_l stands for the data loss in %, F for sample rate of the ADC, N_M for the number of Meridian-ADCs, M stands for the number of incoming *Framemarkers,* d_r denotes the number of received data bytes. The basis of the calculation was to determine the difference between originally sent amount of data from the ExG-system and the received data at the PC terminal. The Table 3-IV below shows the results of the measurements extracted from the test of data loss of ExG-system.

3.1.8 Wired Synchronization

If the ExG-system is to be used in a 256 channel system or distributed as an EEG cap on head, ECG vest on the chest, EMG in arm, each of the systems is required to be synchronized with the other. This will help to further correlate the multimodal data from different sensors or to achieve a 256 channel density. A separate USART interface on the ExG-system was conceptualized for this purpose, allowing several ExG-systems to be cascaded as shown in the Figure 3.25. One of the ExG-systems in this assembly was defined as Master which periodically as specified in the configuration header of the firmware *HD_EXG_OS* sends a sync character to all connected slaves on the same USART-bus. Each slave recorded the sync character and inserted it into their stream of data. Since all of the SLAVE devices are connected by a hard wire, they all receive the sync char at the same time. In the offline

data analysis, the sync characters were traced to adjust the frame of data from different ExG-system for time synchronized evaluation of the data according to the Master device as shown in the Figure 3.26.
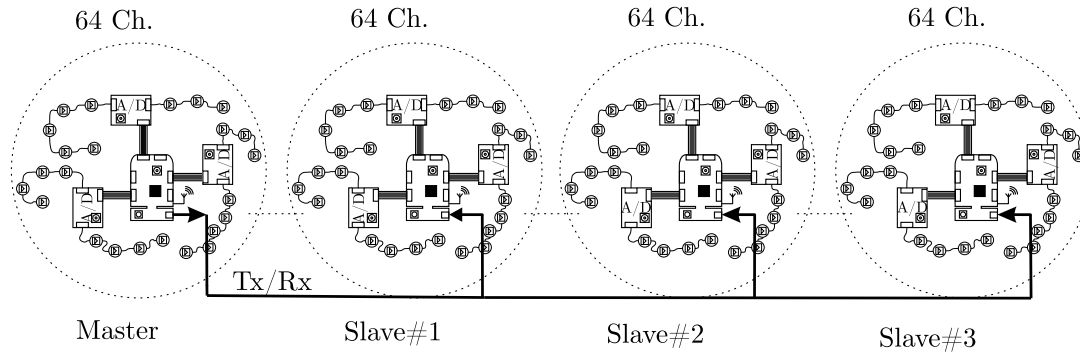
Figure 3.25 A wired synchronization concept of achieving 256 channel of biopotential data acquisition with 4 ExG-systems is presented. The master ExG-system sent a sync-character at a predefined regular interval (e.g. 20 s) over USART to all the slave ExG-systems and they caught this sync-character and inserted it into their data stream so that the measured data can be correlated with the help of the positioning of this sync-character.
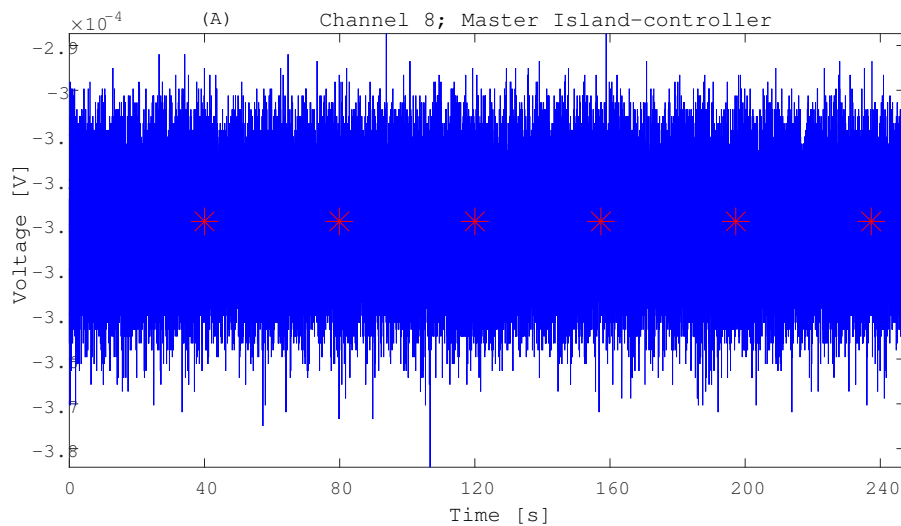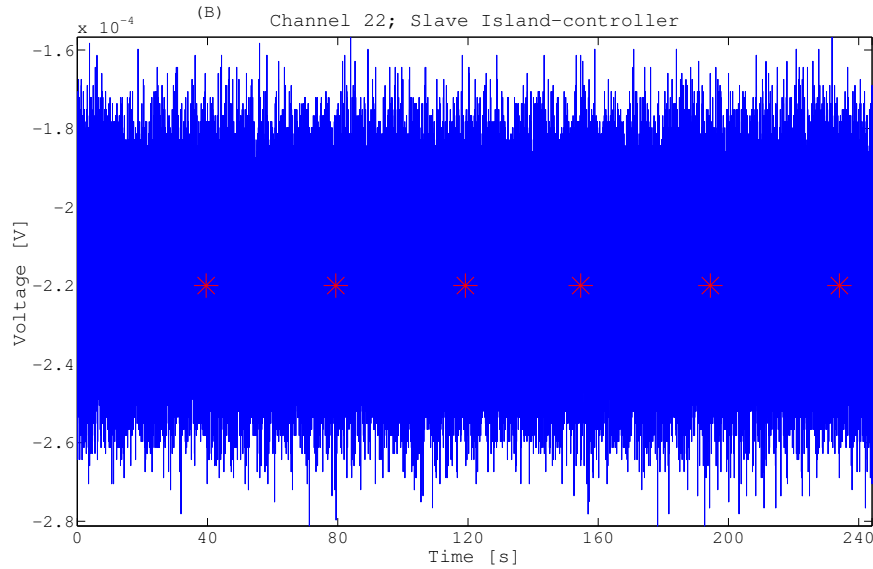
Figure 3.26 A test of time synchronization were performed on two Island-controllers where sync points were inserted every 40 seconds; (A) Master node which initiated the measurement and starts the recording of the sync character, Blue (dotted) is the data and red asterisks shows the sync points. (B) Synchronous measurement starts at the slave node and also records the sync points (red asterisk) with test data.

3.1.9 Summary

By employing the novel modular concept of developing an ExG-system, the number of recording channels with the help of dry electrodes was extended. In its maximum setting using four ExG-systems, 256 channels of data can be achieved. This would enable a spatial sampling resolution <2.5 cm. A wired synchronization concept and implementation was provided. As a consequence the affordability of the system became higher and its design became more compact. However a wireless synchronization of the modules was not realized in the ExG-system. Due to its wireless data transmission capability, the sys-

tem became mobile. Herein it presented the first of its kind wireless ExG-system with a channel density of 256 [**64**]. The system shows a successful integration of WiFi supporting IEEE 802.11b. The system exhibited a low power consumption 41 mW/channel in spite of being incorporated with a power hungry WiFi (Receive ~140 mA, Transmit ~150 mA) module and stand as the 2nd lowest in the comparison table 3-V among the available similar systems at the market.

A dedicated OS was developed for the ExG-system for biopotential measurement which executed the DAQ using DMA for optimal resource planning. The OS was state-based and contains "power-save" state for energy efficient operation.

The generation of the patient's reference voltage at the Meridian-ADC help, low-noise INA, maintaining reduced electromagnetic interference (EMI) techniques in PCB design helped to achieve a relative low peak-to-peak input noise of ~11 µV (see Figure 3.22). Since the root of thus relatively higher input white noise was the voltage reference, a redesign of the Meridian-ADC was necessary.

3.1.10 Final Iteration

In the final interaction a redesign of Meridian-ADC was carried out in which the ADS1299 was used instead of ADS1298, another low noise voltage reference *ISL21090* and a frequency band limitation (using a band-pass filter) between 0.15 Hz and 200 Hz were realized as shown in the Figure 3.27. The new Meridian-ADC was named as *Meridian-ADC_v2*. The detailed circuitry of the band-pass filter containing the active high-pass filter and a passive low-pass filter was shown in the Figure 3.28.
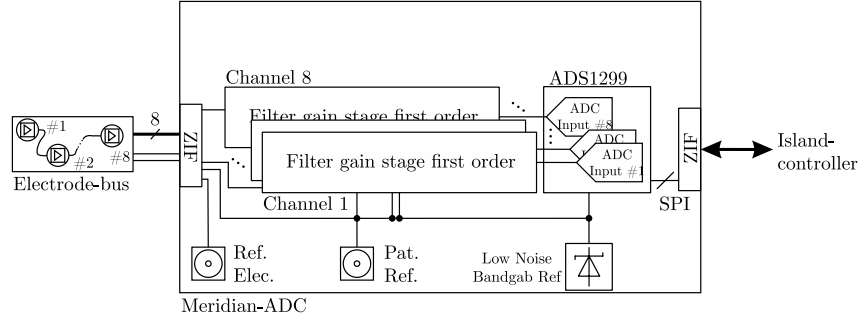
Figure 3.27 Module based schematic diagram of Meridian-ADC_v2 with interfaces towars Electrode-bus and Island-controller. The analog signal processing with filter gain stage of first order and further digitization with ADC1299 is sketched. The output coax interface of patient's reference (Pat. Ref. in the schematic) and input coax interface for reference electrode (ref. Elec. in the schematic) is also shown.

The developed band-pass filter was measured to have the following the characteristic parameters:

Corner frequencies: 0.15 Hz and 200 Hz

Bandwidth: 199.85 Hz

Center frequency: 99.925 Hz

Selectivity: 0.5

These characteristics parameters are extracted from the measured data curve shown in the Figure 3.30. After conducting a short-circuit test, the system resolution of the new ExG-system with Meridian-ADC_v2 was found as ~6.8 µV.
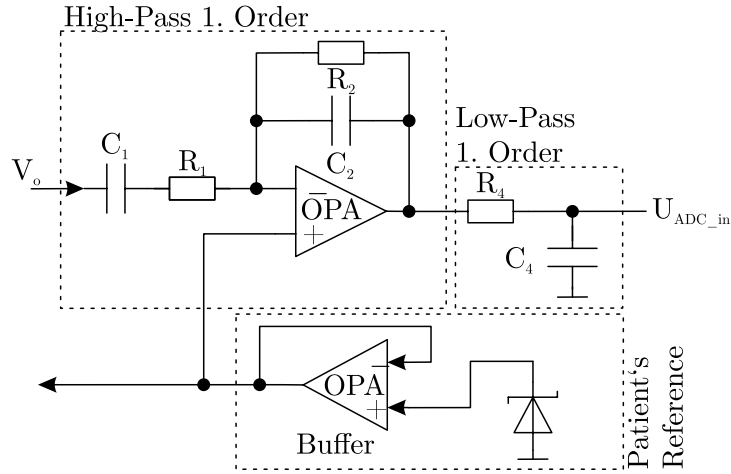
Figure 3.28 The circuitry of the filter gain stage of first order of Meridian-ADC is presented where OPA and INA are the abbreviations of operational amplifier and instrument amplifier respectively. The differentially output voltage V_o from the Electrode-bus of a channel is taken as a input and U_{ADC_in} as output from this filter gain stage as well as input for the ADS1299 are shown.

The achieved dimension of the Meridian-ADC_v2 PCB was (width x breadth x height) 50 x 30 x 1.3 mm^3.
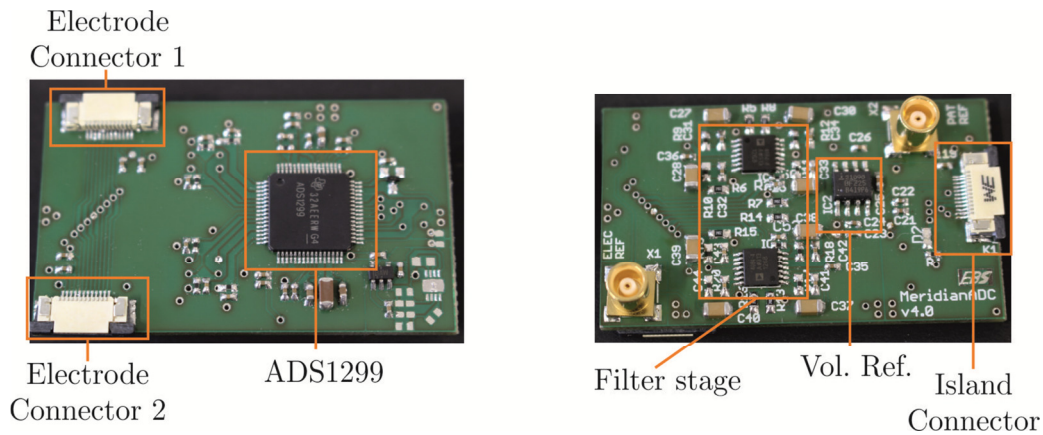
Figure 3.29 The final iteration of Meridian-ADC, namely Meridian_ADC_v2 with 2 ZIF connectors for connecting Electrode-busses as shown in left and the new low noise voltage reference (Vol. Ref.) *ISL21090* from shown on the right
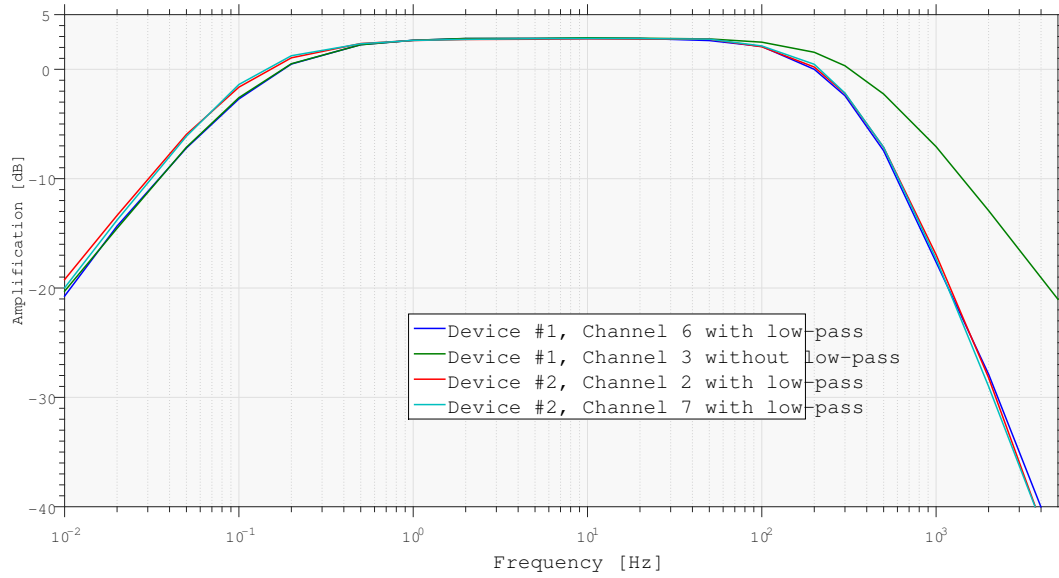
Figure 3.30 Experimental verification of the band-pass filter of Meridian-ADC_v2
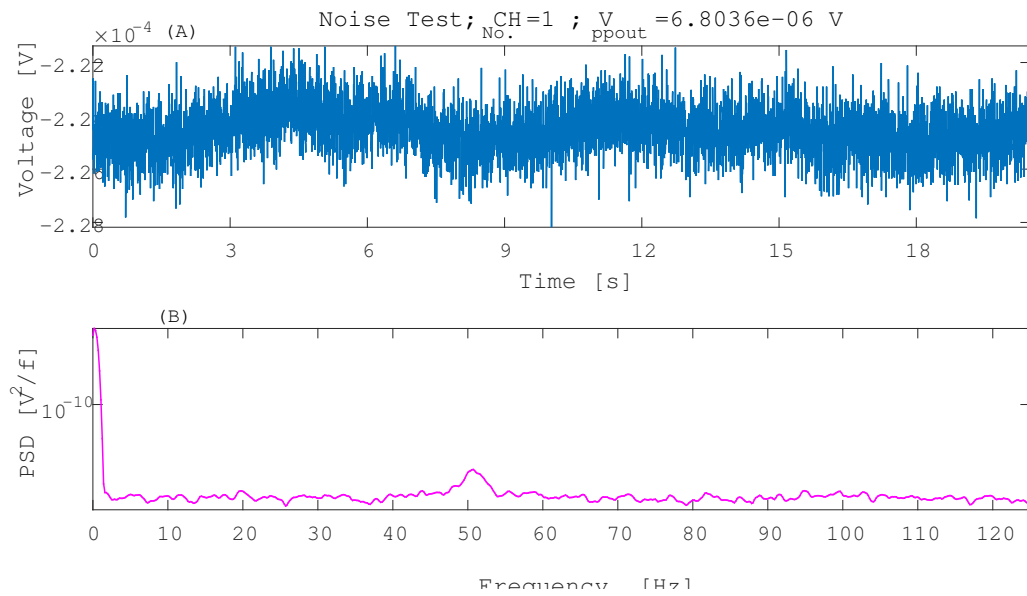
Figure 3.31 Noise test for verifying the system resolution of the ExG-system using the Meridian-ADC_v2; (A) The read-out raw voltage data in the time domain and PSD amplitude in frequency domain

Table 3-V A comparison table with the important specifications of the state-of-the-art Biopotential measurement systems

Parameter	Name of the University where similar systems were developed						
Institution	This Work	UCLA COTS	Tokyo University Personalized	Zhejiang University COTS	Duke COTS	Michigan Personalized	UCSD Personalized
Number of Channels	64 (256)	6	1	2	12	4	1
Signal Resolution [bit]	24	8	-	12	12	-	-
CMRR [dB]	110/115	-	90	126	-	77	-
Maximum Resolution	4μV$_{pp}$	0,06-15 mV	-	-	-	01,-5 mV	3,8 μV
Max. Detectable Frequency	500 Hz	240 Hz	-	4,5kHz	15kHz	10kHz	100Hz
Max. Amplification	35/41 dB	46 dB	-	40 dB	30 dB	39 dB	46 dB
Carrier Frequency	2,4 -2,497 GHz	916 MHz	80-90 MHz	2,4 GHz	2,4 GHz	94-98 MHz	2,4 GHz
Maximum Baud Rate	1Mbps	9,6kbps	-	70kbps	-	-	-
Wireless Communication	802.11b/g/n	FSK	Analog FM	Bluetooth	802.11b	Analog FM	Bluetooth
Supply Voltage	3,3 V	3 V	3 V	3,7 V	3,3 V und 5 V	1,5 V	3V
Power Dissipation/Channel	6 mW	66 mW	10 mW	-	333 mW	2,2 mW	300 mW
Range	40m	2 m	16 m	100 m	9 m	0,5	-
System Clock	32 MHz	4 MHz	-	-	66 MHz	70138 kHz	-
Dimension [cm³]	3,5x5,6x0,6	2,6x2,6x1,8	5,1x0,8 cm²	3,6x2,2x0,4	5,1x8,1x12,4	1,7x1,2x0,2	0,17 diameter
Type of DAQ	Non Invasive	-	-	-	Invasiv	-	-
Bibliography		[70]	[69]	[68]	[67]	[66]	[65]

3.1.11 Encapsulation

A stable mechanical and electrical assembly of the electronics was essential part of the project. To integrate the electronic components of the ExG-system (Electrode-buses, Meridian-ADCs, Island-controller, PCB patch antenna) in a textile cap from *Waveguard*™ [**71**], an innovative and creative design methodology was required so that the ExG-system could be treated as a wearable platform by maintaining the medical standard and law of medical diagnostic products. For positioning electrodes in the Waveguard cap, the international 10−20 system positioning was employed. For each of the components of the ExG-system a separate housing was manufactured using a *MakerBot Replicator 2* 3D printer [**72**]. At the end the ExG-system including its housing was encapsulated in the Waveguard textile cap. First a design concept for placing each of the components of ExG-system in a textile cap to be worn a human head was developed. The concept for deploying 64 channels of EEG electrodes according to the international 10−20 system standard was mentioned before and is shown in the Figure 3.31 below. Following the concept the electronics components of the ExG-system were encapsulated with the help of textile weaving technology and the final encapsulated cap is shown in the Figure 3.32.
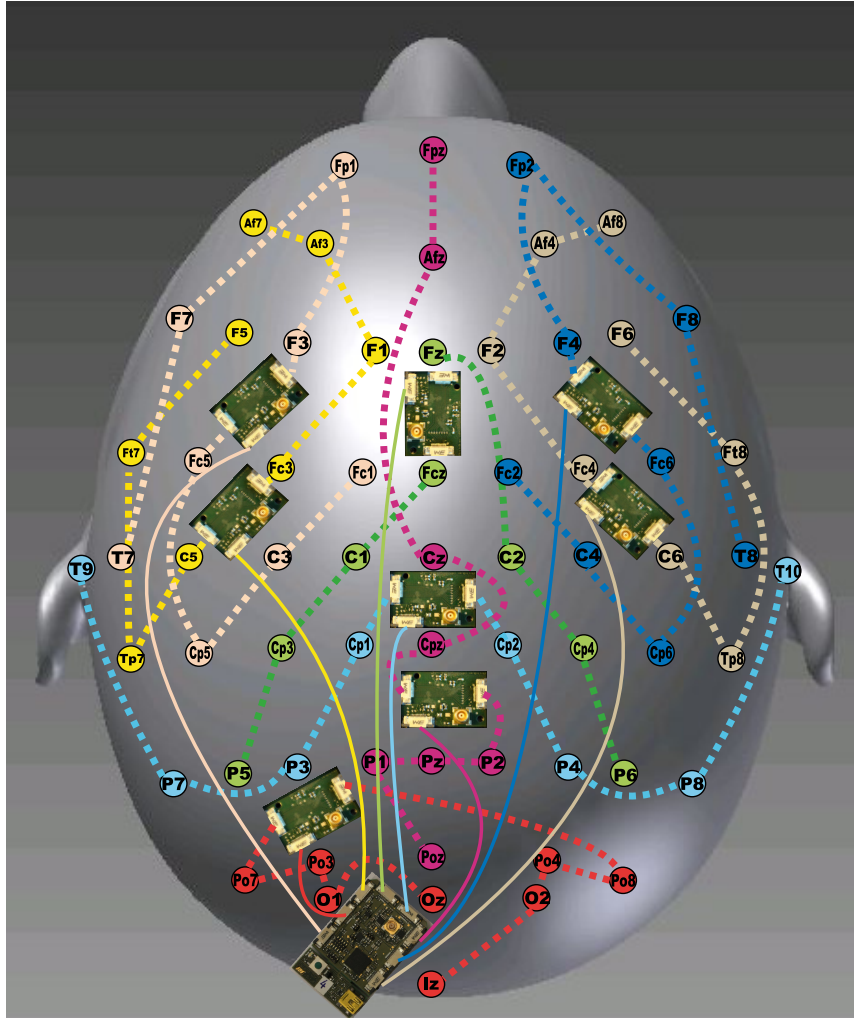
Figure 3.32 Placement of the ExG-system components according to the international 10−20 system for positioning electrodes

Figure 3.33 Encapsulated ExG-system showing the dry electrodes where the electrode-bus was woven into the middle layer of the textile cap on a Mannequin

3.2 SSVEP- and AEP stimulator

EEG-based BCIs make use of visual/auditory stimuli to elicit steady-state visual evoked potentials (SSVEP). The frequency of it is then mapped into a computer input for controlling a device. In this section, the development of the steady-state visually/auditory evoked potential stimulator (SSVEP/AEP-stimulator) will be discussed.

3.2.1 System Design

The system was required to do the following:

1. It should play a video, audio, picture data continuously from a given folder

2. The user should be able to start/stop the measurement

3. At the start and stop of each data, it should insert a timestamp based on the local clock of the system.

Table 3-VI Compatible multimedia data formats for the SSVEP/AEP-Stimulator

Video	Audio	Picture
H.264	WAV	JPG
MPEG-4	MP3	PNG
MPEG-2 (Commercial license)	OGG	GIF (not animated)
VC-1 (Commercial license)		BMP
MJPEG		TIF
VP6, VP8		PCX
OGG Theora		XPM
		TGA (uncompressed)
		LBM
		PBM

It should comprise of two interfaces (USB, LAN) towards the PC side, a 3.5-mm audio cinch connector for audio output and a HDMI output for connecting a monitor.
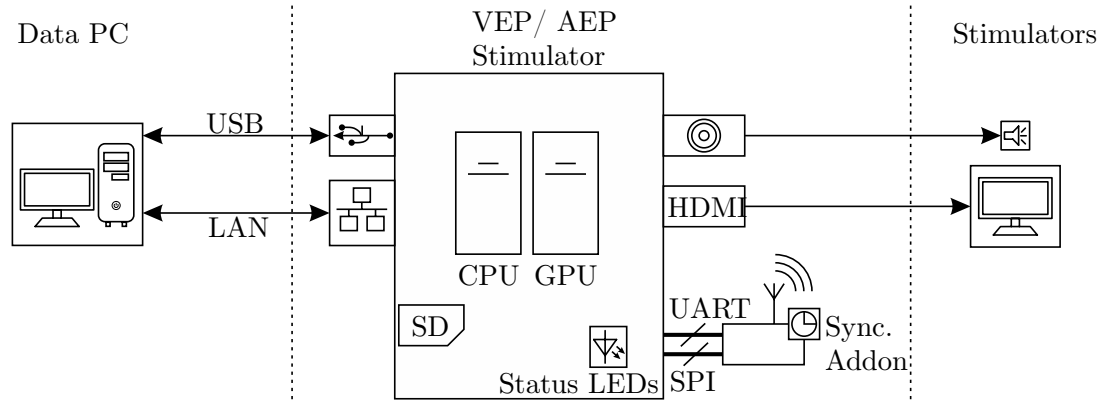
Figure 3.34 Architecture of the SSVEP/AEP-stimulator and its interfaces towards PC and output modalities (speaker, monitor)

For realizing the time synchronization of the SSVEP/AEP stimulator, it should also possess a UART interface for connecting the synchronization addon which will periodically send its trigger. Moreover it should play the following data formats mention in the Table 3-V. To realize these functionalities, a Raspberry Pi (RPi) [73] was utilized. The functional block diagram in the Figure 3.34 describes the working procedure of the stimulator.

3.2.2 Software

To control the data and processing of the time information a real-time operating system (RTOS) was required. *Raspbian,* an unoficial port of Debian Wheezy, [74] operating was chosen for this purpose and *Omxplayer* [75] was chosen to play the media data from a specified folder.
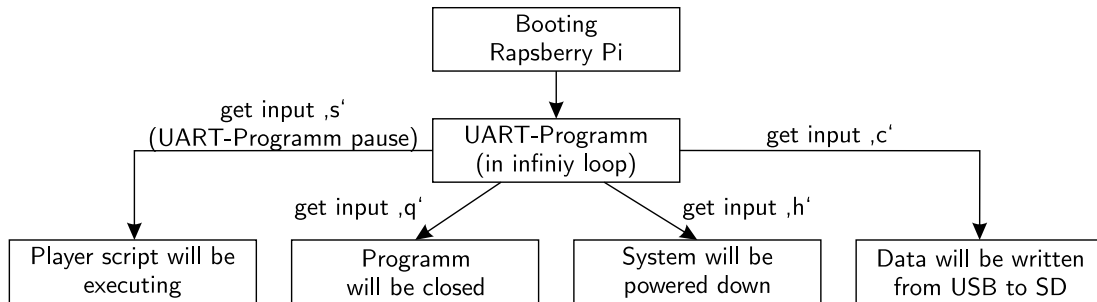
Figure 3.35 Flow-diagram of the main state machine running in Raspbian OS which is triggered by the commands over UART interface

A main finite-state machine was realized using programing language C shown in Figure 3.35 which waited for a user input via UART interface and executed respective operations.
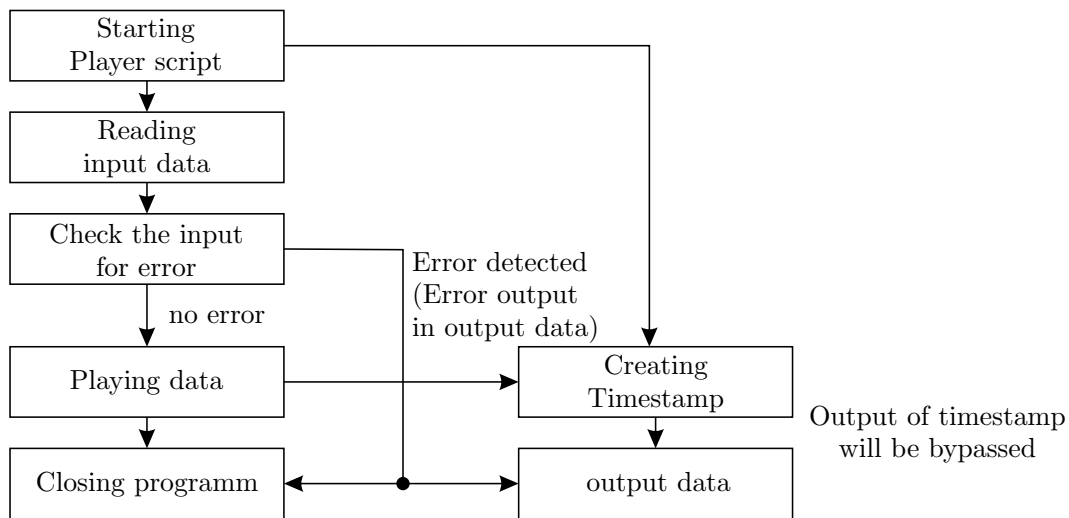
Figure 3.36 Flow-diagram of the *stimulator_player* shell script

It was named *SSVEP_AEP_OS*. If the *SSVEP_AEP_OS* receives a 's' ASCII character via UART interface it started a program names *stimulator_play.sh* shown in the Figure 3.35.

The script plays the data after reading from a lookup table (LUT) the kind of data, order and length. As the script runs the timestamps before the start of each data and after the stopping of each data were recorded.

3.2.3 Time Accuracy

Since the stimulator will be used for group experiment as shown in the Figure 1.1 in the Chapter 1, it was required to investigate the time accuracy of the system. The idea was to pause the playing of a data immediately after it was played. This enables the start playing a media data at a specific time. It was realized through the first in first out (FIFO) of the *Omxplayer*. In realizing the FIFO controlling of *Omxplayer* using the shell script *player_script.sh,* a little delay occurred between the issuing of a FIFO command and reaction of the *Omxplayer* which is also attached to the FIFO. To determine this delay an experiment using two parallel running programs were executed as shown in fig. In which *Program 1* generates a timestamp (t_0^{prog1}) and send a FIFO command to *Program 2* to start another action. As soon as the *Program 2* receives the command from *Program 1* over FIFO, it generated a timestamp (t_0^{prog2}). The delay/reaction time is defined as:

$$\Delta t_0 = t_0^{prog2} - t_0^{prog1} \qquad (3.2)$$
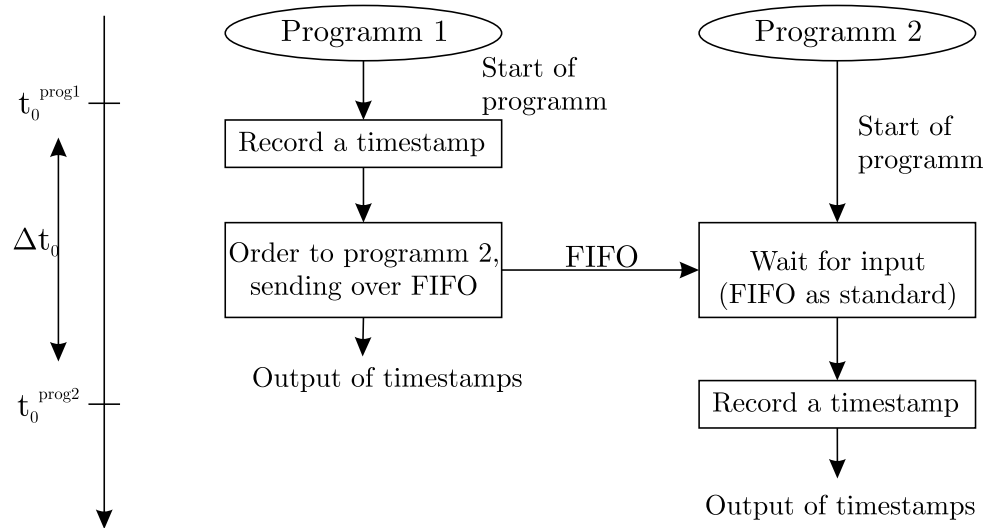
Figure 3.37 Flow-diagram of the programs used to determine the accuracy of the timestamps recorder at the beginning and the end of a media data

The results of the test are shown in the Table 3-IV. It is evident from the Table that delay of transmitting over a FIFO took ~10 ms. The maximum variation was ~2.4 ms.

Table 3-VII Determination of reaction time Δt_0^{prog1} over FIFO

t_0^{prog1} [µs]	Δt_0 [µs]	t_0^{prog2} [ms]	Variation from average Δt_0 [ms]
738302	749055	10,753	0,596
200897	212338	11,441	1,284
568995	580563	11,568	1,411
568880	576961	8,081	2,076
738800	749820	11,02	0,863
917360	925960	8,6	1,557
137699	149140	11,441	1,284
66234	73959	7,725	2,432
125488	133509	8,021	2,136
5656	13483	7,827	2,33
738999	750451	11,452	1,295
891101	902595	11,494	1,337
217080	228280	11,2	1,043
649187	660761	11,574	1,417
Average			
		10,1569286	

4 Clock Synchronization

The main emphasis of this thesis lies on the clock synchronization of multi-modal wireless collaborative BCI system comprising of ExG-systems; inertial measurement units (IMUs), SSVEP/AEP-Stimulator, and a signal processing PC. In this Chapter, at first the time synchronization concept for a cBCI scenario will be presented. Since each of the system in a cBCI scenario can be characterized either as sensor or actuator and these together form a sensor-actor network, they can be modelled as a sensor-actuator network. Modelling of time synchronization protocol in such a sensor-actuator network will be presented in the Section 4.2. In this work several suitable state-of-art time synchronization protocols were implemented considering the same cBCI scenario. The implementation of these time synchronization protocols in the cBCI scenario will be described in this chapter. There were two different kinds of measurement setups conceptualized and realized for conducting stationary and dynamic measurement. These setups will be briefly discussed in this Chapter. For each kind of measurement a novel measurement and evaluation technique was devised and will be discussed. At the end an in-depth analysis of the result will be presented.

4.1 State-of-the Art Time Synchronization Protocols

The overall performance of a distributed wireless sensor network depends on time synchronization. Clock synchronization is an old problem long before the advent of wireless sensor networks and has been studied extensively. An atomic clock is a classic solution and is found in global position system (GPS). Due to its size, cost, power consumption and poor indoor signal quality, it is not practicable to equip a small sensor node used for BCI with a GPS module. Each sensor node is equipped with an independent software clock generated by a local oscillator which is prone to phase noise due to voltage fluctuations and temperature change. The hardware clock exhibits a skew irrespective of the initial calibration. To compensate the drift and skew, the clocks of the sensors have to be adjusted in continuous intervals so that the offset between the sensor clocks becomes close to zero. Time synchronization in wireless sensor networks is a widely studied phenomenon and a number of time synchronization algorithms have been introduced. Some of the most common protocols include: (i) Reference Broadcast Synchronization (RBS) [76], (ii) the similar Flooding Time Synchronization Protocol (FTSP) [77], (iii) Multi-hop Broadcast Synchronization [78], (iv) Timing-sync Protocol for Sensor Networks (TPSN) [44], and (v) Pairwise Broadcast Synchronization (PBS) [79] which all require a precise time stamping at the MAC layer of the radio module. RBS utilizes the broadcast property of the network layer to synchronize the sensor nodes with one another. A chosen reference node broadcasts messages at certain intervals and the nodes which are to be synchronized generate timestamps at the receipt of the broadcast from the reference node. All the receivers exchange their timestamps after they received the reference broadcast with one another. Based on these observations, each node calculates its relative offset and skew with a linear regres-

sion. The MBS protocol is similar to the RBS protocol but differs by forming a network with a global time stamper (GTP) initially. It does not correct its clock during the synchronization phase since all the neighboring nodes correct its clock with respect to the GTP. MBS relies on the safe functionality of the broadcaster and GTP nodes. In this work a novel protocol termed Hybrid Broadcast Synchronization (HBS) was established; it is a hybrid of RBS and MBS and can be directly applied to collaborative BCI. The HBS protocol does not need any dedicated GTP in the network. HBS utilizes both the elimination of the sources of delay at the sender's side, as RBS and GTP similar to MBS to correct its clock. For the above mentioned protocols, the microcontroller (µC) of each sensor node requires access to the MAC layer of the radio module to generate a timestamp as soon as the reference broadcast is received [76], [77], [78]. However, this is not possible in many medical devices where the access to the lowest stack is prohibited for certification and security issues. Therefore, these protocols need to be adapted according to the requirement of a collaborative BCI scenario. The various synchronization protocols were evaluated on a test-bed for a collaborative BCI and their performance was compared.

4.2 Synchronization Concept

The problem definition in the chapter 2 propagates the need for time synchronization in a cBCI scenario. The cBCI is composed of a group of probands all wearing an ExG-system, IMUs and their ERPs are triggered by a same SSVEPA/AEP-stimulator. An ExG-system and a SSVEP/AEP-stimulator were already developed in this work and described in the previous chapter. In the existing scenario presented in the Figure 4.1 a multimodal sensor-actuator network consisting probands embodied with wireless biopo-

tential measurement systems (ExG-system, IMUs), SSVEP-stimulator, video
camera connected to the signal processing PC – all connected through a
common access point. Now the time synchronization among these multimod-
al sensors was needed to be achieved without any modification in the exist-
ing multimodal sensor-actuator network. To develop a first of its kind as far
the knowledge of the author time synchronized multimodal sensor-actuator
network for executing cBCI experiments, it required a combined embedded
[80] hardware-software solution.
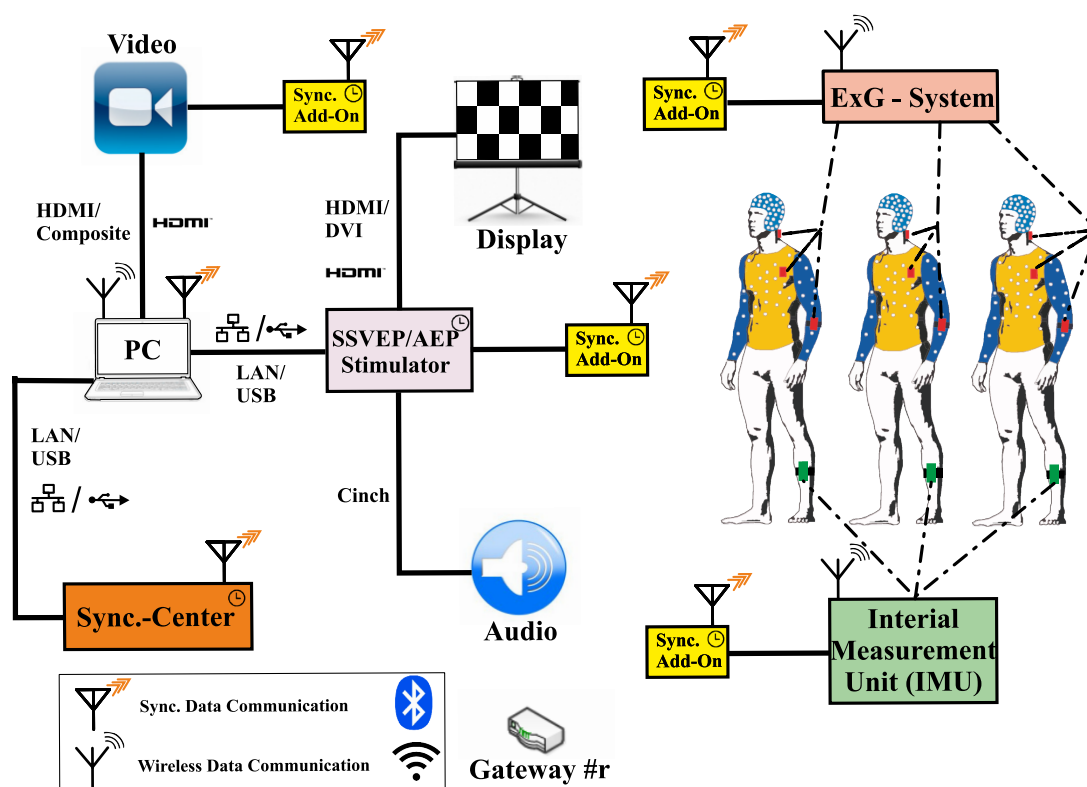
Figure 4.1 Enhancement of the cBCI scenario with the realization of time synchro-
nization using synchronization-center and synchronisztion-addon

To solve this issue a novel, intelligent hardware pair consisting of a synchro-
nization-center (SC) and synchronization-addon (SA) were conceptualized.
The SC was attached to the main signal processing PC and SAs were at-

tached to ExG-system, IMU, video camera, SSVEP/AEP-stimulator. Only a single SC was required for the network and SA for each sensor/actuator module. The hardware pair mainly consisted of a microcontroller (µC) for implementing the live algorithm of the time synchronization protocol and a radio module for wireless transmission of data required to implement the protocols. To achieve live time synchronization simultaneously with the data measurement and transmission which was controlled by firmware of ExG-system, two dedicated firmwares [81] were required to be developed for the novel hardware pair. The firmware is a finite-state-machine on which the time synchronization algorithms were to be implemented. The firmware implementation will be described in detail in the subsection 4.2.2. This is so far the first of its kinds of implementation in a cBCI scenario as far as the author's knowledge is concerned. The results of the above described method were published and acknowledged in international conferences and journals [82], [83].

The SC comprised an Ethernet interface for PC; the SA incorporates a universal asynchronous receiver/transmitter (UART) and transistor-transistor logic (TTL) interface for the ExG-systems. Both also contained a battery-powered ± 20 ppm stable and accurate crystal oscillator, a Bluetooth low energy (BLE) module, a µC and a secure digital memory card (SD card). According to the *Federal Communications Commission* (FCC) any unlicensed medical device can use the industrial scientific and medical (ISM) frequency band [84]. Since the *BLE112* module from *Bluegiga Technologies* [85] is already a *Conformité Européene* (CE) certified stack, it simplifies the further certification of the envisioned application, thus it was chosen as a radio module. A crystal oscillator with a resonance frequency of 16 MHz was used to create timestamps with µs precision, the BLE module for communicating the global timestamps from SC to SAs, and the µC to implement dif-

ferent time synchronization protocols. This allowed comparing the synchronization protocols for the same cBCI scenario. Due to the intended use of the cBCI for medical applications, it was required to implement the protocols by only accessing the application layer of the Bluetooth module. The timestamp of a received message was generated at the finite-state machine (FSM) of the host processor connected to the Bluetooth module via an UART interface. This is different to other state-of-the-art protocols in which the timestamp is generated in the MAC layer of the radio module. The disadvantage is that this approach increases the average time delay of the message transport above the typical delays sources in conventional protocols [77]. At the application layer of the FSM processing time is unpredictable, asymmetrical and highly variable due to different tasks running on the FSM. In the Section 4.5.1, the variance of the measured delays will be discussed in more detail. One of the key challenges in this work was to develop an algorithm to adjust the clock of the sensors in a way so that the variations of processing time at the sensor nodes can be eliminated.

A critical communication path is defined here as the path of a software message originated from the physical layer of the BLE module to the application layer at the µC, and its associated traverse time, as shown in red color in the Figure 4.2. Since the message at the sender side also suffers from the delays introduced in the critical path, a receiver based synchronization protocol was chosen to be developed. By utilizing a receiver based algorithm the uncertainties added due to the time-stamping at the application layer at the sender side could be eliminated. However, for the recently proposed PBS method based on a two-way messaging protocol, it was theoretically shown that using two different delay models (an exponential and a Gaussian model) required less overheads to adjust the clock skew and offset [79]. Moreover, it utilized Cramer-Rao low bounds and maximum likelihood estimators to de-

termine the clock skew and offset analytically. As mentioned by the authors, this protocol has not yet been evaluated experimentally and still states an open research problem [**79**]. Here, this protocol was adapted and implemented for the cBCI scenario to verify the synchronization accuracy. A novel hybrid time synchronization approach which is a combination of RBS and MBS was proposed in this work and will be described below. Before describing the protocol, it is required to model the clock of a general sensor node.

4.2.1 Mathematical Descriptions

The main two variables of the clock are slope (s_i) and offset (k_i) which are to be adjusted with the help of a synchronization algorithm on the fly. In a receiver based sync protocol a designated reference node broadcasts N messages periodically in a network. Each of the nodes in the network generates a timestamp as soon as it receives the broadcast message from the reference node. The number of messages is linearly proportional to the accuracy of the estimation of skew and offset; however increasing numbers of messages for a synchronization phase requires more energy. This is a trade-off which was investigated in [**86**]. In the MBS protocol one node was specified as parent node. This node generated timestamp t_p^k for k^{th} broadcast from the reference node and broadcasts it so that all neighboring node can collect a synchronization point pair consisting of (t_i^k, t_p^k). Once a node collected the predefined number of timestamps (N), it can calculate the skew difference and time offset difference with respect to the parent node skew using a linear regression:

$$\varphi_i^{d\_t} = \frac{\sum_k^N (t_p^k - \bar{t}_p)(t_i^k - \bar{t}_i)}{\sum_k^N (t_p^k - \bar{t}_p)^2} \tag{4.3}$$

$$\theta_i^{d\_t} = \bar{t}_i - \varphi_i^{d\_t} \bar{t}_p \tag{4.4}$$

where $\varphi_i^{d\_t}$, $\theta_i^{d\_t}$ represent the skew and time offset difference of node i with respect to the parent node, respectively; t_i^k, t_p^k denote the time at node i and parent node of the broadcast message number k, respectively; $\bar{t}_i$,$\bar{t}_p$ describe the average of local timestamps on parent node and node number i for N.

In the above described cBCI scenario the SC acted as a reference node and SAs as general network nodes. The timestamps were collected at the host µC connected to the BLE of SA, as shown in the Figure 4.3. The critical path induced four more sources of delay as compared to common implementations for wireless networks using MAC layer time stamping. These can be defined as $T_{GLD}, T_{BGLD}, T_{UARTD}$, and T_{INTD} where T_{GLD} is the delay to transmit the message from the Link Layer (LL) to the Generic Access Profile (GAP); T_{BGLD} the time required to process the message by the application peripheral interface (API) of the Bluetooth module, T_{UART} the time to transmit the message over the UART and T_{INTD} the interrupt handling time at the host controller [76], [77], [78], [44]. Additionally, there could be a presence of jamming signals from external Bluetooth/Wi-Fi modules sharing the same 2.4 GHz frequency band in the vicinity which could deteriorate the robustness of the synchronization and add further delays due to increased access time as well as blocking of transmission channels. These additional delays introduce new challenges in the given application scenario for the algorithm implementation.
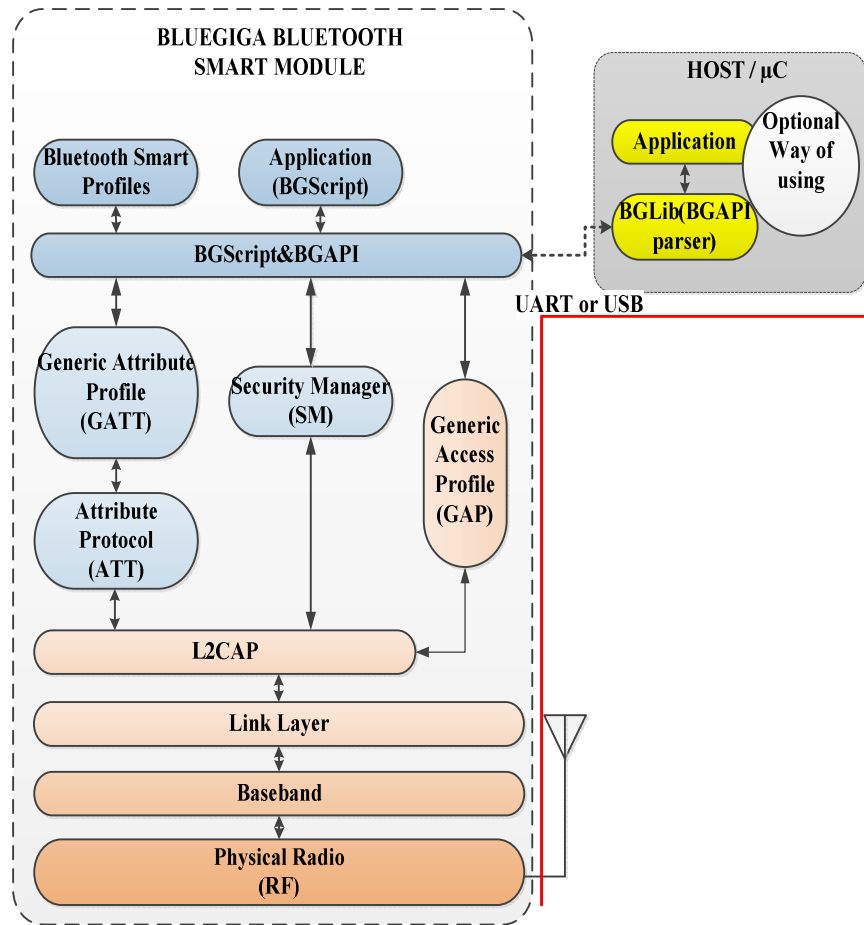
Figure 4.2 Smart software stack of a *Bluegiga* Bluetooth low energy 4.0 module and host μC including the software interface (UART or USB). This visualizes the critical path (indicated in red) from the RF layer of the BLE stack to the application layer of the μC. The time required for a message to travel the critical path defines the additional delay introduced by the proposed synchronization method.

To cope with the delays in the critical path without having a precise timestamp triggered the development of a novel hybrid broadcast synchronization protocol for usage in the cBCI scenario. In the following the protocol is described.

4.2.2 Protocol Description

The time synchronization in the heterogeneous sensor network was realized with the help of a SC connected to a central PC and several SAs. For each sensor node in the cBCI scenario one SA was required. During the initialization phase (INIT) the SC sent a "*Hello*" message, the SAs generated a timestamp as soon as it recognized an interrupt at the UART bus of the µC. The SAs exchanged their timestamps with each other to eradicate initial offset accordingly. After that the synchronization phase (SYNC) began, in which the SC sent messages with its ID, message number (*MsgNo*), interval between messages (*T*) and *N*. Every SA which is to be synchronized generated a timestamp at the receipt of the broadcasts from the SC. At the end of the synchronization phase when the predefined number of broadcasts from the SC was reached, the SAs exchanged these timestamps with each other so that every SA has the information about the receipt of the broadcast at other nodes. The SA stored these timestamps along with its own timestamp in a two dimensional table. It was assumed that the SA with the minimum timestamp among all the SAs received the message first; this defines the parent node. This assumption was based on a statistical measurement on the time differences among the SAs that will be discussed further in section V. The parent node was not fixed but determined dynamically in each sync phase. This had two main advantages; in case of failure of a parent node in the network or if more nodes were added, in the next sync phase it could be substituted by another one. Furthermore, since the parent node was dynamically selected, it was not required to block a node for providing the functionality of a parent. The selected parent node provided the global time in the network. Once each of the SAs collected *N*, the HBS protocol calculated the

skew difference considering the minimum offset, $\varphi_i^{d\_\theta}$, of each SA using linear regression (LR) according to:

$$\varphi_i^{d\_\theta} = \frac{\sum_k^N (t_i^k - \bar{t}_i)(\theta_{min}^k - \bar{\theta}_{min})}{\sum_k^N (t_i^k - \bar{t}_i)^2} \tag{4.5}$$

It then adjusted its local clock t_i to a corrected value t_g according to the following equation:

$$t_g = t_i + \bar{\theta}_{min} + \varphi_i^{d\_\theta}(t_i - \bar{t}_l) \tag{4.6}$$

where $\theta_{min}^k, \bar{\theta}_{min}$ described the minimum offset of the kth message and the average of all minimum offsets, respectively.
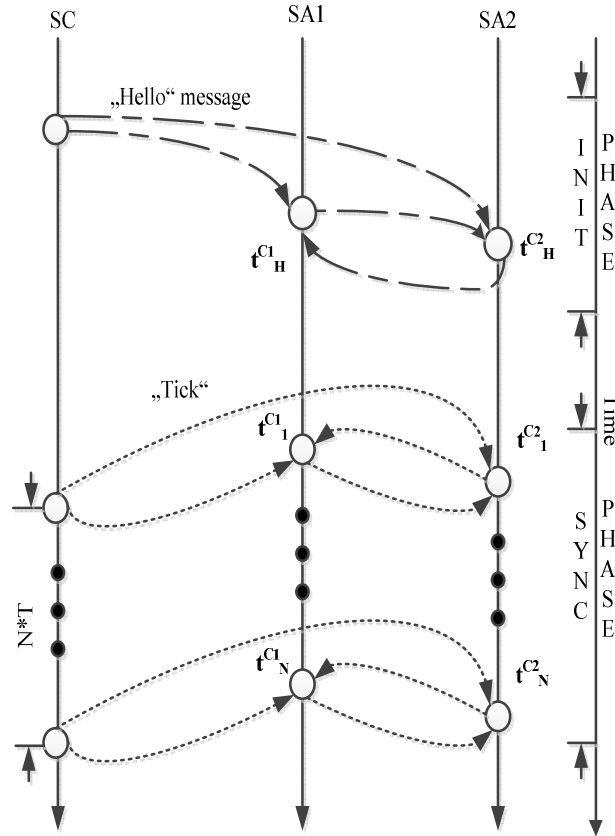
Figure 4.3 HBS protocol in two phases; INIT phase establishes the first handshaking to create the network; SYNC phase implements the message communication regulation to adjust skew and offset with each other.

The Figure 4.3 shows diagrammatically how the HBS protocol exchanges messages in a network with two nodes in the initialization and synchronization phases. Between the two phases, there was a time out interval. During the initialization phase the SC initiated a handshake "*Hello*" message to find out the number of nodes present in the network. After that the synchronization phase began and lasted for N*T seconds.

4.3 Implementation on a cBCI scenario

For an actual implementation of the time synchronization algorithm for a cBCI scenario as shown in the Figure 4.1 (based on the ExG-system described in the Chapter 3), a number of constraints had to be taken into account.

A general PCB prototype as shown in the Figure 4.5 was developed on which the functionalities of SA and as well as SC were implemented. If it was to be used as a SA, it could be attached to each sensor node through an UART interface, to utilize it as a SC, the Universal Serial Bus (USB) interface for connecting a PC was used. As it should be possible to seek medical certification for the final end application, the following specifications were set: a) each SA must use a separate radio channel for communication of the sync messages, b) the sync protocol should be implemented at the application layer without accessing the low layer protocol stack, c) each SA should be able to store timestamps up to 24 hours. Furthermore, a low power consumption implementation was desirable; therefore we used a BLE module and tried to minimize the required number of messages for time synchronization. For ease of hardware realization, a PCB was designed that allowed to implement both the SC and the SAs. The hardware consisted of a crystal oscillator, a BLE module, a low-power µC, an Ethernet IC *CP2200* [**87**], high-density connectors and a battery protection and management IC *BQ24074* [**88**] from TI. The central component of the PCB was an 8-bit low-power µC ATXmega128A1 [**56**] from Atmel® with 9 kB RAM and 128 kB flash memory. The *CC2450* IC, which is the core of *BLE112* module, is a true system-on-chip from TI for Bluetooth low energy applications offering data rates up to 1 Mbps using *Gaussian frequency shift keying* (GFSK) [**89**]. A stable ($\pm$20 ppm) external crystal oscillator with a frequency of 16 MHz

was chosen to generate a local clock with 1 µs granularity. Employing an external crystal oscillator allowed the timer events of the µC to work also in low power mode so that an energy efficient synchronization protocol could be established.

Table 4-I Structure of the timestamp clock variable

Bit position	Name of the Variables
0:15	Microseconds (µs)
16:31	Milliseconds (ms)
32:39	Seconds (s)
40:47	Minutes (m)
48:55	Hours (h)

Two custom-made optimized real-time-operating systems (RTOS) were developed using the programming language C, of which one ran on the SC and the other on the SA. The software clock of the SC and SA were generated using the fast reacting (below 1 µs) event system of the µC, in which the timer event was triggered by a timer overflow. The timestamp of the software clock was realized as a 56-bit long variable comprising six components as shown in Table 4-I.

The finite state-machine (FSM) of the firmwares of SC and SA contained the following main states: a) hand-shaking, b) synchronization phase, c) wait phase, and c) fail-back state. The SC, connected to the central signal processing PC (see figure 4.1), was responsible to create and manage the sensor network with groups and hops [90] so that an individual group can be

allocated to a particular functionality within a cBCI application. The firmware had a direct interface with a PC which analyzed the BCI data to generate control signals (i.e. in the VEP/AEP stimulator); a simplified flow-diagram of SC is shown in the Figure 4.3. It broadcasted periodic "Ticks" every time interval T, as depicted in the flow-diagram of the Figure 4.3.
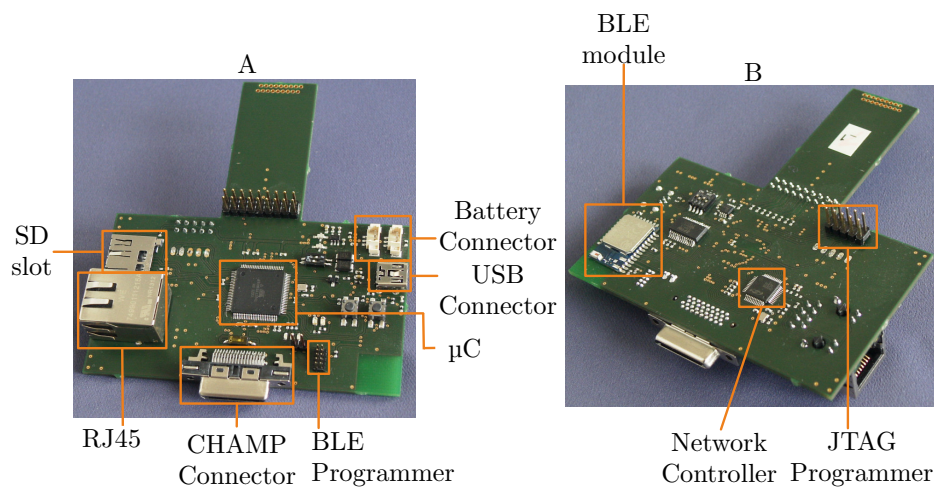
Figure 4.4 First prototype of the SA; A) Top side of the sync modules with SD slot for micro SD card, RJ45 for LAN connection, Champ connector for connecting biopotential amplifier and other debugging interfaces (programmer, USB); B) Bottom side of the sync module where BLE module, network processor for LAN and programming interface are visible

The other firmware was located on the SA, where the calculation to estimate the synchronization parameters took place and informed the ExG-system about the current time via a transistor–transistor logic (TTL) trigger. The flowchart of the firmware for the SA is shown in the Figure 4.5. The EEG-system recorded the timestamps and integrated them in the measurement data stream of the ExG-datasets from each proband. Cross-correlation and further signal analysis then would allow determining the occurrence of P300 ERP from the probands. According to the specifications, time variables were required that do not overflow in 24 hours. Within this

time period, the timestamps increase in their value, thus it requires more memory space to store the average of N timestamps which is needed to compute the skew in the sync phase. The average is stored in a floating point variable which has a maximum length of 32-bit. After reaching a measurement time of more than 6 h, an overflow occurred in this variable. As a consequence skew computation became faulty which was a non-trivial problem. To overcome this issue the skew computation was broken down into several steps by using memory space optimized variables, as shown in the equation 4.7. To realize the computation the local time average $\bar{t}_i$ of node i to be synchronized was calculated as:

$$\bar{t}_i = t_1 + \frac{T(N-1)}{2} + \frac{\Delta t_1 (N-1)}{N} + \frac{\Delta t_2 (N-2)}{N} + \cdots + \frac{\Delta t_{N-1}}{N} \qquad (4.7)$$

where N is the number of synchronization messages in an interval, $\Delta t_k = t_{k+1} - t_k - T$ for $k \in (1, 2, 3, \dots N)$ is the deviation in the interval time from expected value, which is in the range of milliseconds, and t_k is the timestamp of the kth message.
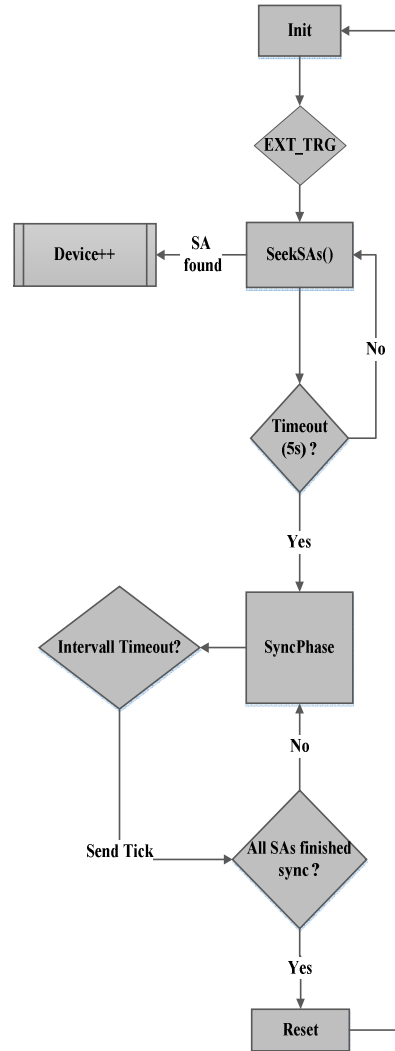
Figure 4.5 Simplified flow-diagram of the state-machine of the SC showing the interface (Device++) to the signal processing PC, network discovery (finding SAs) and synchronization phase.

This mathematical formulation allowed the average to be calculated correctly as a 32-bit floating point variable in an 8-bit reduced instruction set computing (RISC) architecture even when the sum of all timestamps t_k is at the highest possible value of a 64 bit variable (2^{64}–1). Now using the equation 4.7, the skew computation was reformulated by introducing three inter-

mediate variables so that the final value of the skew difference $\varphi_i^{d\_\theta}$ could be fitted into a 32-bit floating value:

$$\varphi_i^{d\_\theta} = \sum_{x=1}^{N} \frac{B_x}{(C_1^x A_1 + C_2^x A_2 + C_3^x A_3 + \cdots + C_N^x A_N)} \tag{4.8}$$

where $B_x = \theta_{min}^x - \bar{\theta}_{min}$; $A_x = t_i^x - \bar{t}_i$;

and

$C_1^x = \frac{A_1}{A_x}, C_2^x = \frac{A_2}{A_x}, C_3^x = \frac{A_3}{A_x}, \dots, C_N^x = \frac{A_N}{A_x}$, for $x \in (1, 2, 3, \dots N)$

In a similar way, the equation 4.3 was reformulated. Since the chosen 8-bit controller did not support floating point operation, a suitable software library was utilized for the purpose. The maximum length of the variables used for skew and average calculations was 32-bit. Employing the equations 4.7 and 4.8, it was possible to limit the variables $\bar{t}_i$, $\varphi_i^{d\_\theta}$ to 32-bit, even when more than 6 hours of time elapsed. Since the computation was implemented using a software library, the µC took a relatively long computation time of ~250 ms. The long computation time did not however affect the synchronization accuracy as this computation time was calculated in each phase and then subtracted from the global time adjustment. Moreover, in a 250 ms time window the relative drift between the crystal oscillators of two different SAs was negligible.
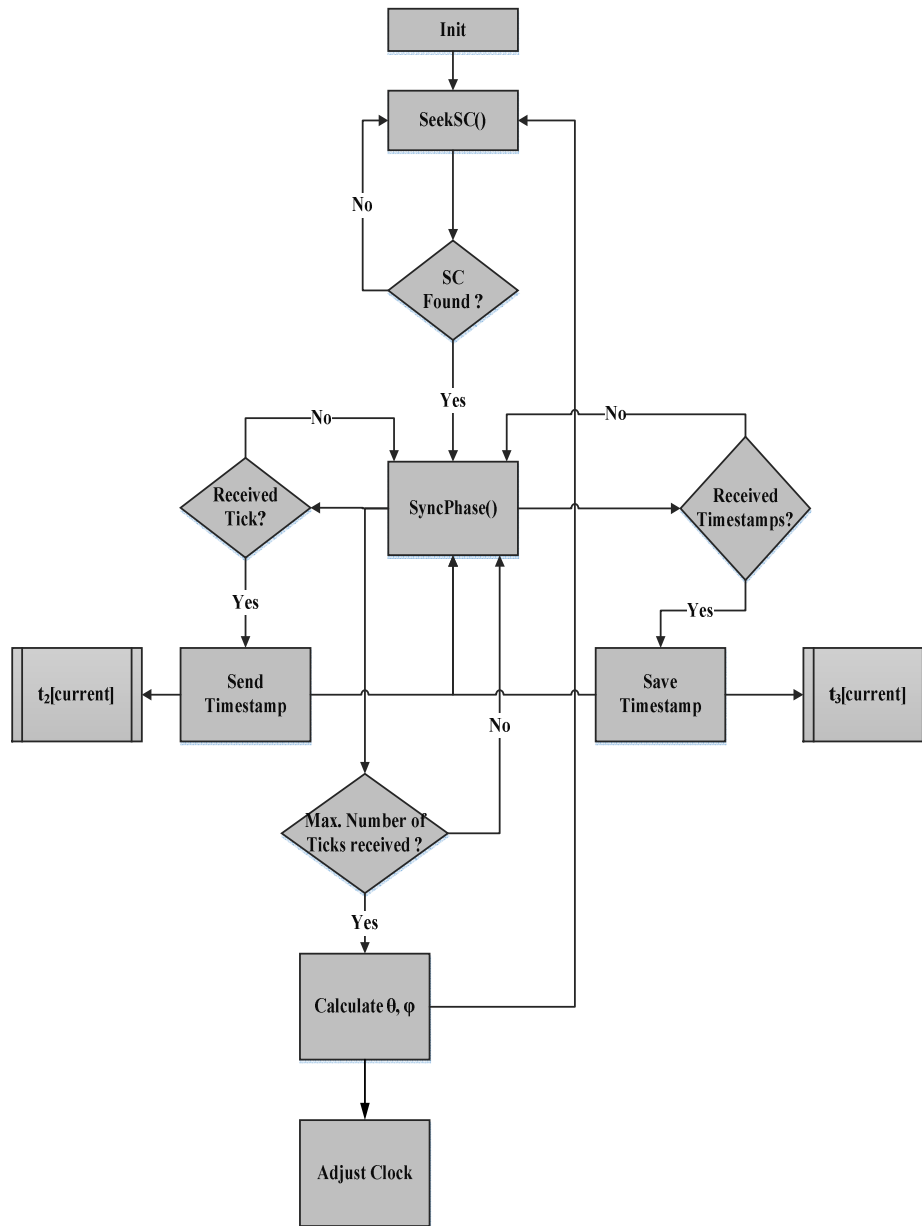
Figure 4.6 Simplified flow-diagram of the state-machine including the initialization (handshake) and synchronization phase of the SA.

To verify the accuracy of the computation described above using the floating point software library (Float64) in comparison to MATLAB running on a 64-bit Intel processor and to a standard double variable of the AVR-GCC library [91], a test was conducted. In this test the values of the inter-

mediate variables were recorded and evaluated offline. During the test with N = 10, T = 10 s, the values of these variables using the equations 4.7 and 4.8 were calculated in the µC and on a PC with an Intel 64-bit processor. The values were compared to off-line MATLAB computations using the equations 4.3 and 4.4; from Table II is can be seen that an exact value within a meaningful time resolution was able to be calculated with the proposed method. Furthermore, it is obvious that the standard AVR GCC library was unsuitable.

Table 4-II Comparison of the accuracy of the timing variable used in the protocol implementation between MATLAB, Float64-software library and double of AVR-GCC

Variables	MATLAB	Float64 (after simplification)	AVR-Double
$\bar{t}_i$ [µs]	1.613069098000000e+07	1.6130690980000001e+7	Not possible
$\bar{t}_p$ [µs]	161272194	161272194	Not possible
$\varphi_i^{d\_t}$	0.999935488238323	0.99993548823832301	1.000687
$\theta_i^{d\_t}$	4.511975334447622e+04	4.5119753344476223e+4	-43552.000000

4.4 Evaluation and Analysis

After successful implementation of the protocol algorithm in the sync hardwares (SAs, SC), it was required to evaluate their performance. In this section the three different measurement setups for charactering receiver-to-receiver delay [92], verifying the accuracy of synchronization and corre-

sponding measurement techniques, their results will be presented. At the end of the section an analysis of the results will be discussed.

4.4.1 Experimental Setup

The objective of the measurement setup was to characterize the systems SA, SC and their performance in terms pairwise difference between the receptions of messages, synchronization accuracy, stability, safety. Three different measurement setups were conceptualized for the tests. It was required to test for two wireless sensor network scenarios in which each SA can be considered as a sensor addon. There were three basic setups: a) Chi-Square test for determining the pairwise difference [76] between the receptions at different SAs was achieved using a statistical Chi-test [93], b) time synchronization test on stationary nodes, and c) time synchronization test on mobile nodes. In order to evaluate the reproducibility of the measurement result, all of the measurements were repeated for three times according to specified parameters. The main parameters were T: interval between the broadcast, N: number of synchronization points and ϑ: speed of the model train in case of dynamic measurement. During the measurement the temperature was kept constant and monitored with a thermoelement (type K) connected to a multi meter. In order to give a qualitative marker to the synchronization, a *figure of merit* (FoM) namely *synchronization error* (sync error) was defined as below:

$$\delta_{n,m} = t_k^{SA\#n} - t_k^{SA\#m} \tag{9}$$

$\delta_{n,m}$ denoted the relative difference in time between on SA#n with respect to SA#m at an instantaneous moment considered as k.

a) Chi-Square-Test

To characterize broadcasting based synchronization protocols it was first required to find the delays between the receptions of the broadcast messages at all SAs. This would help finding out the achievable accuracy with the developed sync-modules (SA, SC). The task was to determine the distribution of the pairwise difference between reception times at the SAs of a message from a SC. Therefore the parameter pairwise difference [76] between two reception times of a message between the four SAs was required to be defined. The pairwise difference was defined as

$$\Delta_{nm} = t_k^{SA\#n} - t_k^{SA\#m} \tag{4.9}$$

where $n \in \{N_{\nexists} : n \neq m\},$ m was the number of the fixed reference SA and k denoted the kth message. In order to find the statistical distribution or the good fit of the of the parameter Δ_{nm}, a statistical test namely Chi-Square test was performed

The pairwise difference was measured by connecting the GPIO of all SAs to a four channel oscilloscope with the trigger set on the GTP (SA#4). This allowed recording the delay between the rising edges of the GPIO signals with respect to the other three SAs. The GPIOs were programmed in such a way so that it generated a rectangular pulse with a width of 20 ms immediately after receiving a broadcast message from the SC at the FSM of the µC of the SAs.
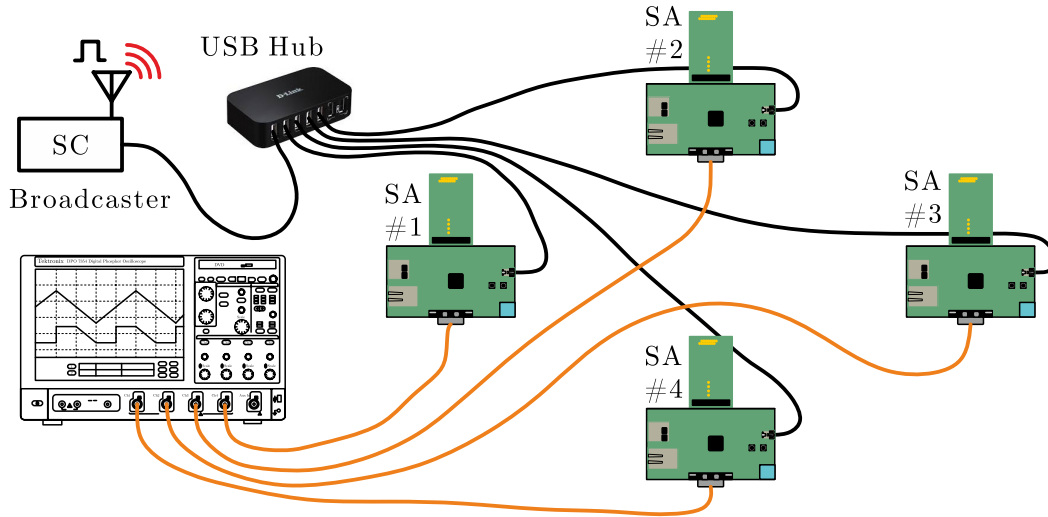
Figure 4.7 Measurement setup for Chi-square test where the GPIO and GND lines of the SAs were connected to a Oscilloscope and a SC sends periodic broadcasts

Since the GPIO activity was controlled at the FSM, it occurred later than the actual reception of the message at the physical layer of the radio module and caused a quasi-random delay. The objective of the measurement was to record the distribution of this delay. The Figure 4.7 depicted the measurement setup in a schematic view and how it was realized in the laboratory. This setup allowed carrying out a Chi-squared test for SA#4 as the GTP. It was repeated for 1500 message broadcasts and a distribution was calculated, as shown as histograms in the Figure 4.11.

b) Stationary Test

The idea of the stationary setup was realized in a scenario where the ExG-systems with SAs were mounted on probands which are fixed to a position. It imitated the scenario of a group EEG experiment which is commonly found in classroom scenario or while observing a keynote presentation and will be discussed in the Chapter 6. In Stationary measurement setup, the

SAs were distributed spatially at a fixed distance from each other on a table. The SC or Broadcaster was also fixed to a position near the Log PC.
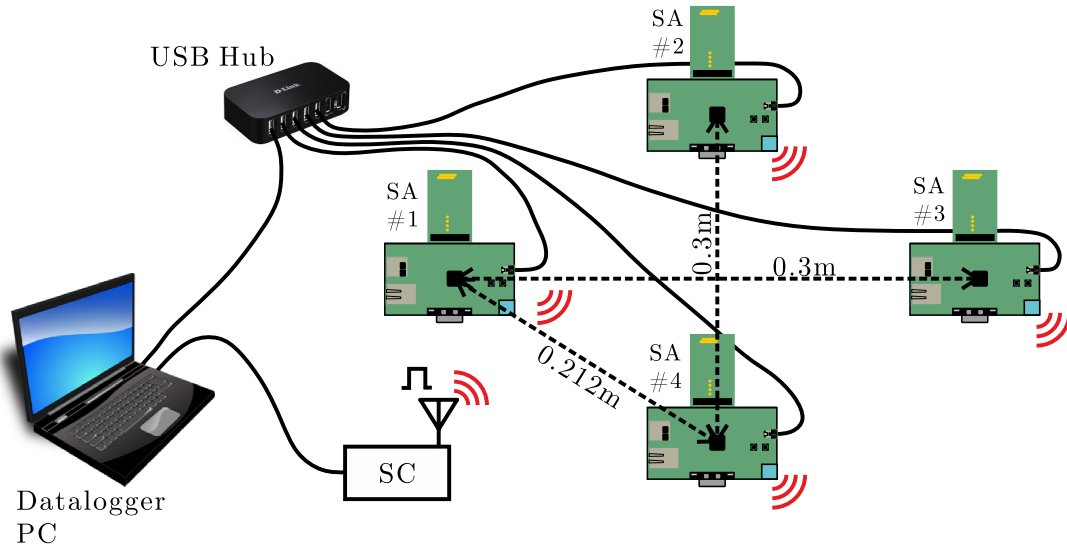
Figure 4.8 Experimental setup for stationary sync modules; 4 SAs were spatially distributed on a table and a SC was placed adjacent to the Datalogger PC; All the modules were powered with USB and this interface was used for getting the timestamps at the Datalogger PC

The synchronization protocols PBS, TPSN, RBS, MBS and HBS were implemented and tested on a test-bed consisting of four SAs and one SC. The measurement setup for time synchronization test with four spatially distributed stationary SAs is shown in the Figure 4.8. They were connected to a common USB-hub linked to the central PC so that the synchronization errors between the SAs could be calculated offline. One of the SAs nodes was chosen as global time stamper (GTP); SA#4 acted as GTP in the network depicted in the Figure 4.8. It generated a rectangular pulse on a suitable general-purpose input/output (GPIO) pin once it received a completion message of the synchronization phase from all other SAs.

c) Dynamic Test

A dynamic measurement setup in which the sync-modules were driven with various constant velocities using a model train was constructed and was described in the Figure 4.8 and in the Figure 4.9. The model train was controlled via a controller area network (CAN) shield connected to an *Arduino* board. SAs were mounted on the compartments of the model train and it generated a timestamp according to its local clock as soon it detects an optical obstacle. The optical obstacle was designed and printed with a 3D printer from *MakerBot* and the optical interrupt was realized with a transmissive photointerrupter *GP1A52LRJ00F* [**94**] from Sharp corporation as described in the Figure 4.10. The objective of dynamic measurement setup was to imitate a scenario of a group of persons walking or jogging with mobile wearable sensors. In this case these mobile sensors were our biopotential measurement system ExG-system connected with the SA (synchronization addon).
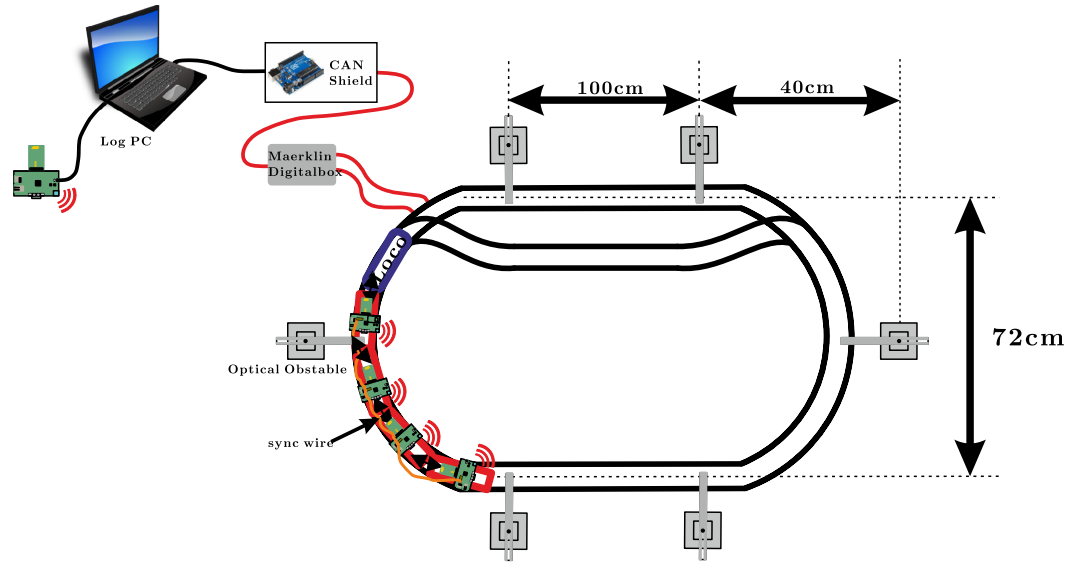
Figure 4.9 Dynamic Measurement setup with a model train on the right on which the locomotive from Maerkin carry the sync-addons; The speed of the model train was controlled by a Arduino Uno board. This was realised using a CAN shield which is connected to the digital control box of *Maerklin* (Maerklin Digitalbox).

The idea of the measurement setup was to evaluate the performance of the time synchronization using the developed sync-module prototypes optimizing cost and effort.
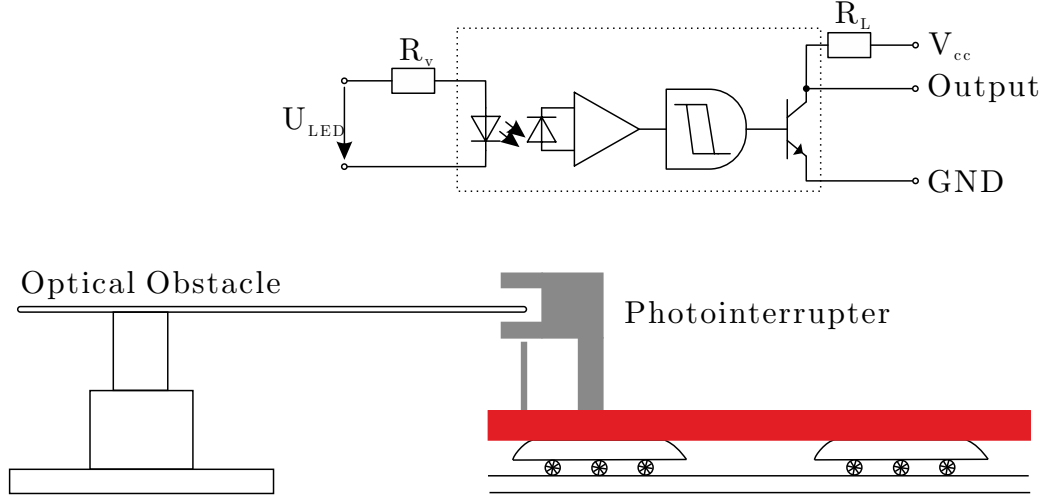
Figure 4.10 zoomed in view of the optical obstacle and the photointerupter with its corresponding circuit

4.4.2 Measurement Techniques

Before the start of the measurement, a fixed protocol was defined for comparing the results with each other. Each measurement was repeated thrice to verify its reproducibility. The stationary tests with were mainly dependent on three parameters; N: number of exchanged messages, T: Time difference between the broadcasted messages, $T_{duration}$: total duration of the measurement. The measurement routine was divided into two categories: a) short span of time of 3 hours and b) long span of time of over 24 hours. Another parameter, ϑ: the speed of the model train was added for the dynamic measurement. The parameters T, N were linearly dependent on the accuracy of the synchronization [86]. These tests were required to ensure the stability, safe functioning of the hardware and finding out software bugs. The computation of the sync variables skew and offset were realized using a self-developed floating point software library according to IEEE 747 [95] as de-

scribed in section 4.2.1, it was essential to verify its correctness in comparison to MATLAB running on an intel PC with Pentium x86 architecture, standard AVR double [**91**], and floating library developed in this work. For that purpose, the variables skew and offset which were calculated with the exchanges and generated timestamps were stored for offline verification from a measurement.

Table 4-III General test conditions

Operating Voltage	3.3 V
Temperature	22 °C
Frequency of the clock Source	32 MHz crystal
Number of runs (N)	20
Interval between broadcasted messages (T)	10 seconds

To experimentally determine the synchronization error for the five implemented protocols, the GTP (SA# 4) was wired to the other SAs. As soon as a SA finished its synchronization phase and corrected its clock, it sent out message "sync finished" to the GTP before starting the next sync phase. It idled in a wait state until an interrupt from GTP; then it generated a timestamp based on its corrected clock. Once the GTP had received the "sync finished" message from all SAs present the network, it generated a 20 ms wide rectangular pulse. On its falling edge, timestamps from all the nodes including GTP were collected to measure the sync error at an instant in time. The sync error between the SAs were determined from an experiment with a number of messages, N=20 and an interval between messages of T=100 s running for three hours.

4.4.3 Results

Chi-square Test

With measurement setup described in the Figure 4.7, the Chi-square tests were performed. To visualize the distribution of the pairwise differences between the reception times, histogram graphs as shown in the Figure 4.11were generated using MATLAB.
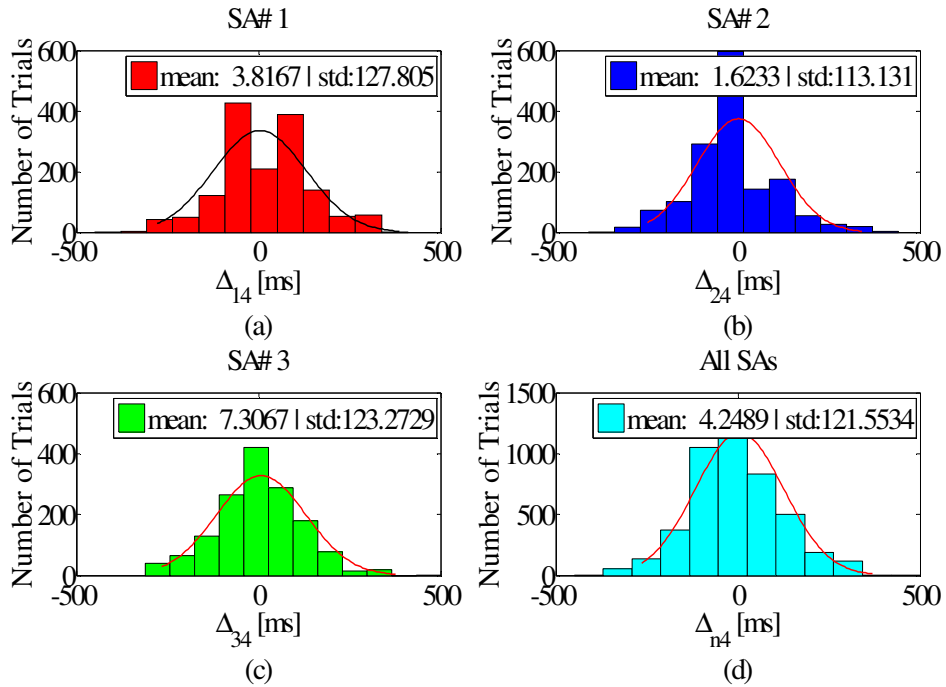
Figure 4.11 Histogram of the difference in reception time between the GTP SA#4 and the other 3 SAs. The mean and standard deviation (std) of the Δ_{nm} (defined in equation) are calculated and shown in the legends of each distribution curve. The mean, std values are given in ms.

The four histograms plots shown in the Figure 4.11 presents the result of the Chi-squared test in which the pairwise difference between the reception times of each SA with respect to SA#4 (GTP) was determined and plotted for SA#1 (see Figure 9a), SA#2 (see Figure 9b) and SA#3 (see Figure 4.11c) as histograms. Figure 4.11d shows a histogram of Δ_{n4} comprising all

measured differences in reception time. The distributions showed an approximated Gaussian form where the pairwise difference was found to be in the range of [-500, 500] ms. The test was repeated three times to verify the reproducibility. Since the broadcast algorithms were based on the assumption that all reference broadcasts arrived at the same time on all SAs, this test provided a measure for the expected sync error after implementation of the protocol on SAs. The distribution of the pairwise difference time reported in [78], [98], [80] was in the range of [+20, -20] µs whereas our test showed a range of [-500, +500] ms. The order of magnitude difference can be explained by the fact that the timestamp was generated at the FSM, which waited for an UART interrupt to generate a timestamp. The FSM also verified if the message came from the expected SC or different node interfering at the same 2.4 GHz spectrum. This was the main source of delay in the generation of the timestamp. With the pairwise difference time reported in [**76**], [**96**], [**78**] it was possible to achieve a synchronization error of below 10 µs, therefore, in our work we could expect a synchronization error of below 250 ms.

Stationary Nodes

Similarly the measure setup described in the Figure 4.8 was utilized to perform the test for determining the synchronization error of each child SA with respect to the parent SA. The sync error measured among the four SAs is shown in the Figure 4.12. In this test, the following test conditions were taken into account:

Table 4-IV Test conditions of stationary tests with SAs and SC

Operating Voltage	3.3 V
Temperature	22 °C
Frequency of the clock Source	32 MHz crystal
Number of runs (N)	20
Interval between broadcasted messages (T)	100 s
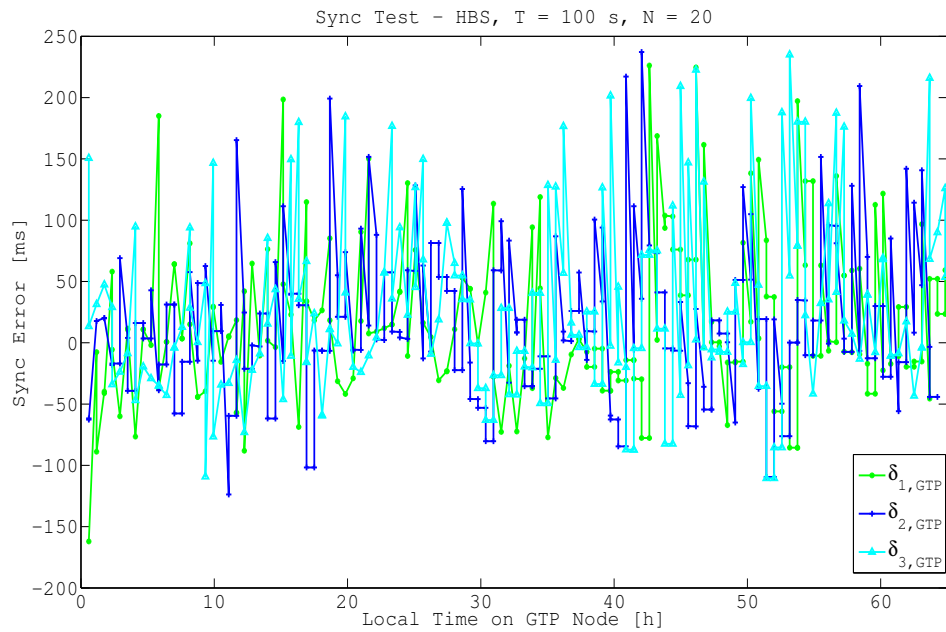
Figure 4.12 In the measurement setup 4 SAs were synchronized to find out the relative time difference on the SAs with respect to a fixed SA which the GTP. The plot shows a measurement result for the evaluation test of time synchronization accuracy among 4 SAs which was run for approximately 65 hours. An average relative difference in time was found to be 14.7 ms, 9.91 ms, 29.4 ms for $\delta_{1,GTP}$, $\delta_{2,GTP}$, and $\delta_{3,GTP}$, respectively.

Table 4-V Overview of synchronization error of five time synchronization protocol for a 3 hours long measurement

Protocol	Sync Error [ms]			Sync Parameters	
	Minimum	Average	Maximum	N	T [s]
PBS	0.167	38.97	98.956	20	100
TPSN	0.179	43.339	147.717	20	100
MBS	0.529	86.980	234.906	20	100
RBS	0.24	65.660	221.033	20	100
HBS	0.343	37.715	237.188	20	100

To statistically analyze the data a confidence interval of 95% was considered on the set of the sync points and visualized in the Figure 4.13. A *confidence interval* gives an estimated range of values which is likely to include an unknown population parameter, the estimated range being calculated from a given set of sample data (definition taken from [**97**]).
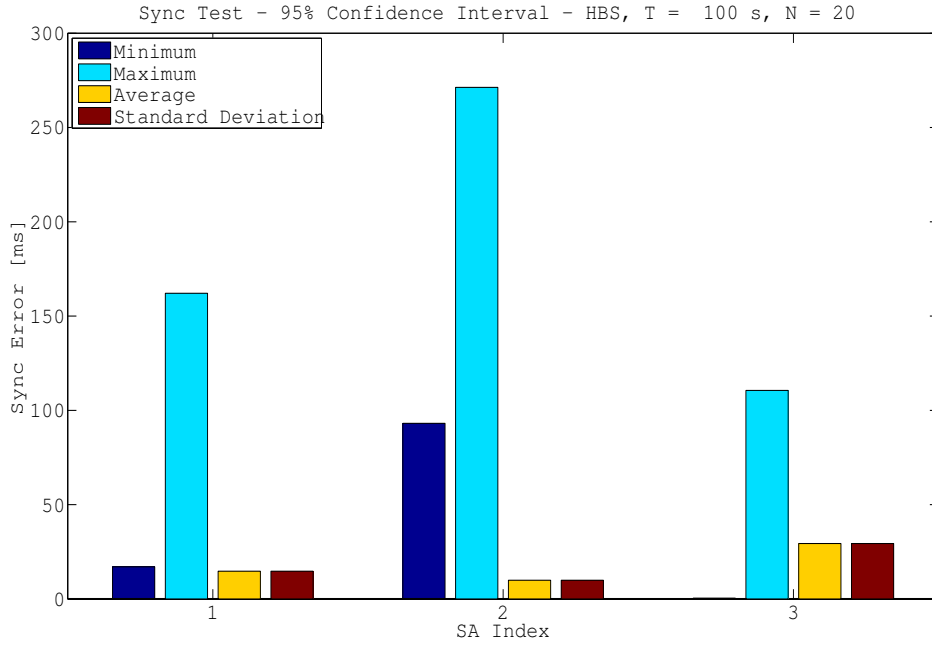
Figure 4.13 Statistical results of the HBS method, showing the minimum, maximum, average and standard deviation of the sync error on 3 SAs w. r.t. the GTP using the 95% confidence interval.

Dynamic Nodes

To evaluate the performance of the sync algorithms while they are running on mobile sync modules, a set of experiments was carried out in the measurement setup shown in the Figure 4.9. Apart from the standard configuration parameters T, N, a new parameter velocity of the model train (υ) was introduced.

The table below shows the summary of result from the dynamic experiment:

Table 4-VI Overview of the results of the time synchronization test on dynamic sync modules

Sync Error [ms]			Sync Parameters		
Minimum	Average	Maximum	N	T [s]	Υ [km/h]
0.046	2.83	84.3	10	100	6
0.09	41.1	209	10	20	6
0.01	9.5	54.7	10	100	6
0.086	28.9	218	10	20	25

The velocity of the model train was set to a uniform speed equivalent to jogging speed of 6 km/h and a running speed of 25 km/h. Due to timely constraints, only RBS protocol was tested in the dynamic scenario.

4.4.4 Summary

In this work four state-of-the-art time synchronization protocols PBS, TPSN, MBS, RBS for a cBCI scenario were adapted and implemented on a hardware test-bed comprising one SC and four SAs. The implementation of the PBS protocol was demonstrated and experimentally evaluated for the first time. Moreover, a novel hybrid broadcasting protocol (HBS) was proposed and was realized. The implementation of the time synchronization algorithm took place at the FSM of the microcontroller of each node connected to a BLE module on a PCB. The main signal processing path started at the physical layer of the radio module and ended at the FSM of the µC. The timestamping was triggered by reception of a message at the end of the signal processing path. Since the generation of the timestamp was executed at the top layer in the signal processing path, it induced four more non-deterministic sources of time delay additional to already existing delays if the timestamp were to be generated at the MAC layer. As a consequence a relatively large sync error during the evaluation of the protocols was noticed.

Utilizing the PBS protocol in the network a sync error of 38.979 ms was achieved in comparison to 65.660, 43.339, 86.980, and 37.715 ms from the adapted RBS, TPSN, MBS, and HBS protocols, respectively. This is however a better sync error accuracy than an estimated value based on the Gaussian distribution of the pairwise difference between two reception times of a message. Implementing the floating point calculation in 8-bit RISC microcontroller architecture introduced a limitation in computation accuracy which was handled with an appropriate mathematical formulation without loss of accuracy. The implementation adhered to the initial specifications that were required to be fulfilled for licensing as a medical product later. The sources of delay were discussed in an analysis of the network, and the accumulative delay was experimentally investigated in hardware with a Chi-squared measurement. The HBS protocol was compared with other state-of-the-art protocols on the network test-bed. For an envisioned application in a P300 based collaborative BCI experiment, the achieved sync error is suitable, since P300 event related signals occur 300–400 ms after stimulation. As identified the cause of achievable sync error lies in the implementation of the time synchronization at the application layer of sync modules, it was decided to apply a cross-layer approach. In this approach the timestamp at the receiver will be generated using the receiving activity map of the transceiver module. In the final iteration of sync modules this approach will be experimented for PBS and RBS methods.

4.4.5 Final Iteration

To achieve a better sync error, it was required to execute the following enhancements in the existing hardware:

    a) Generation of timestamp earlier using a cross-layer approach

    I.   This could be realized if a receiving activity of the radio module could be monitored. As soon as a radio module receives a packet via its antenna, there is current fluctuation visible on a general-purpose input/output (GPIO) as in the form of a rectangular wave. If a µC is attached a radio module to that GPIO pin, a local timestamp can be generated as soon as a message arrived at the radio module; thereby eliminating the sources of delay.

    II.   An further iteration of sync modules are required

b) Instead of using the software stack from *Bluegiga*, develop a custom stack by modifying original stack from *Texas Instruments*, so that the receiving activity of the radio module could be monitored.

4.4.5.1 Hardware

For the sync modules version 2, an ARM® Cortex®-M4 microcontroller namely *ATSAM4E16C* [98]from Atmel Corporation was chosen which consumes less power, has an inbuilt floating point processor so that those complex calculation for skew and offset can be carried out directly on the hardware. Moreover it possesses request-to-send (RTS), clear-to-send (CTS) pins for hardware handshaking and reliable UART data transfer between the µC and the Bluetooth module. To make the sync modules version 2 more energy efficient and smaller, *BLE113* [99] module from Bluegiga was chosen. It contains a *CC2541* [100] radio transceiver SoC from Texas Instrument. The sync modules are sync addon v2 (SA_v2) and sync center v2 (SA_v2). The only difference between them was a debugger board which has a USB and

debugger interface that let to be connected to a PC for debugging purpose and if it was to be used a sync center v2.
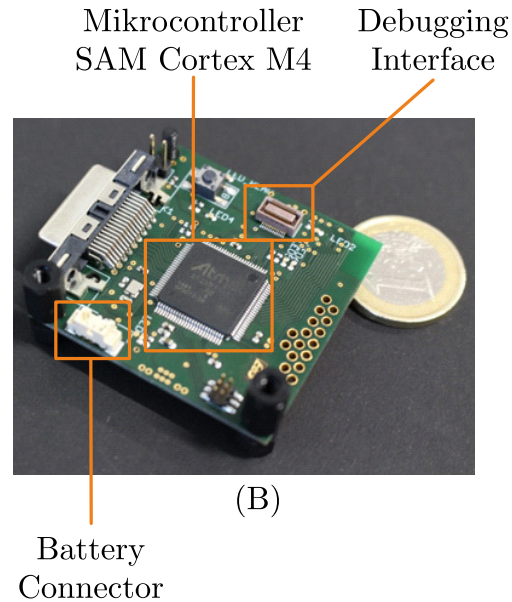
Figure 4.14 Top view of synchronisation-addon v2 with ARM Cortex SAM4 processor, a stable 16 MHz crystal crystal, connectors for battery, slim-slack connector for the debugger board, and connector for ExG-system.

The version 2 of synchronisation-addon as shown in the Figure 4.14 (top view) and in the Figure 4.15 (bottom view) was also optimized in its size and a dimension of 4.5x4.4 cm^2 was achieved which is about 3 times less than side of the version 1 of the previous synchronisation-addon version shown in Figure 4.15 and in the Figure 4.16. Due to the usage of a less power consuming radio and processor, the current consumptionw was reduced to ~50 mA from ~68 mA.

(A)
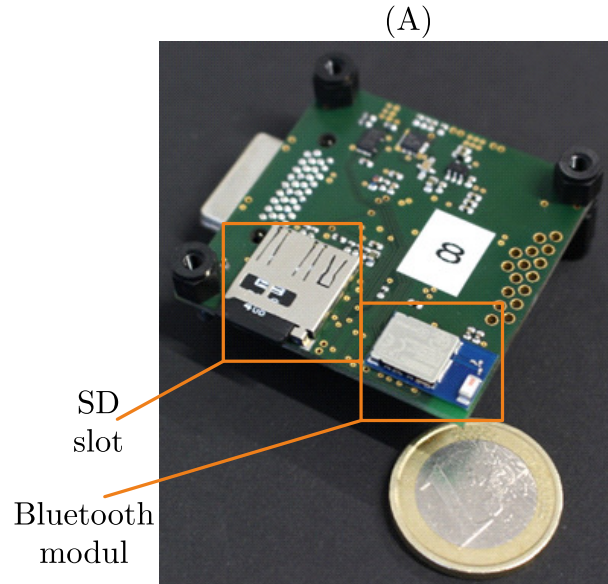
Figure 4.15 Bottom view of the Synchronization Addon v2 with Bluetooth module BLE113, micro SD card holder.

4.4.5.2 Firmware

There were two main firmwares developed:

a) Custom BLE Stack: The aim of this stack was to use *CC2541* as a Bluetooth transceiver and to generate activity monitoring for which the freely available BLE stack was considered.

b) Firmware of the ARM Processor: The main objective of this firmware was to enhance, adjust and port the already existing firmware developed previously for sync modules version 1 and to make it compatible for ARM® Cortex®-M4 processor.

4.4.5.3 Results

To evaluate the performance of the new sync modules a stationary experiment using the same setup explains in the Figure 4.8 was performed. However there were 3 SA_v2 modules of which one was named *Parent* and other two as *ChildA* and *ChildB*. After implementation of PBS, RBS protocol, the following results were achieved to show the performance of the final iteration.
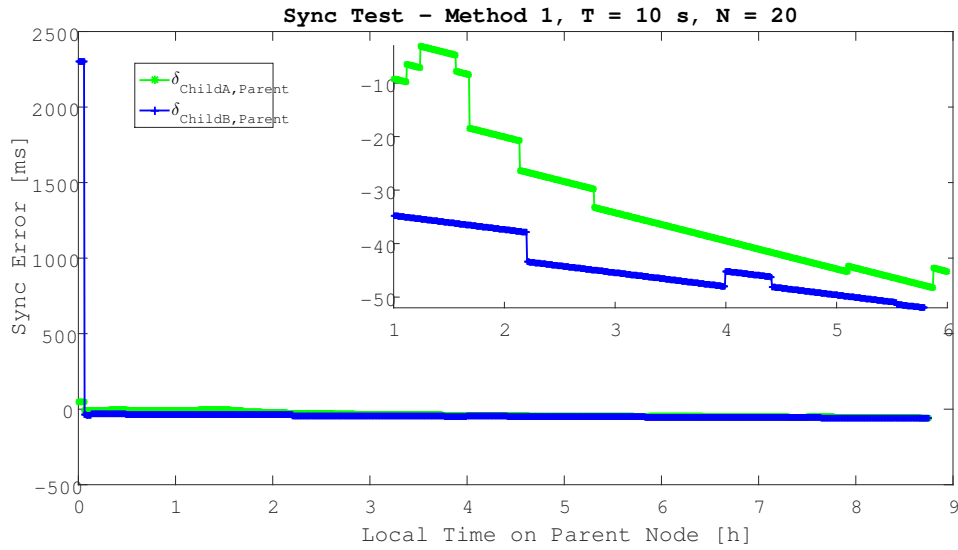
Figure 4.16 Approximately 9 hours long stationary time synchronization experiment with sync modules of final iteration; A zoomed inset diagram shows the plot with truncated axes.

As shown in the Figure 4.16, the maximum, average sync error among the modules were reduced to ~38 ms from ~280 ms and ~32 ms from ~41 ms respectively for T = 10 s and N = 20. The statistical analysis is visualized in the Figure 4.17 in which the minimum, maximum, average and standard deviation of the sync error considering 95% of confidence interval.
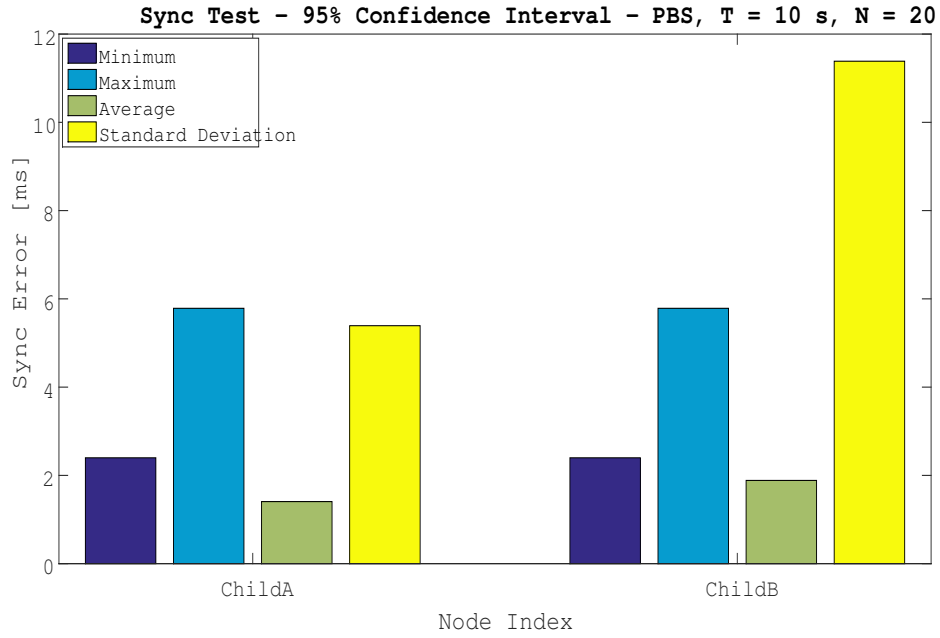
Figure 4.17 Statistical results of the HBS method, showing the minimum, maximum, average and standard deviation of the sync error on the Children SA_v2s w. r.t. the Parent SA using the 95% confidence interval.

5 Discussion

5.1 Analysis of the ExG-system

In the work a high resolution (configurable from 8 up to 256 channels), wireless ExG-system with dry electrodes was developed to be used in telemonitoring of Epilepsy patients as well as for BCI applications. Monitoring the fine structure of spatial and temporal muscle activity require a spatial sampling of 5 mm. Similarly using EEG data as a neuroimaging technique with high temporal and low spatial resolution require a resolution less than 5 mm. This developed system allows to mount 256 electrodes encapsulated in a cap achieves less than of 5 mm resolution. So, the system could be applied to these conditions in which a high density EEG data is required. The demand of long time monitoring of epilepsy patients without hampering their mobility and signal quality possesses a huge problem in the field of medical device technology. The evaluation of the dry electrodes showed that the comfort of wearing such dry electrode was less and dependent on the acceptability of the persons. This resulted in the usage of dry electrode for recording biopotential signals in a restricted period of 1 hour time. However the developed

ExG-system was autarky and was powered through a Lithium-Polymer battery. The chosen battery (*LP 503759*c from *Dynamis* [**101**]) has a capacity of 1250 mAh and could last for 12 .5 hours if only eight channels of data recording is active. The flexible housing of ExG-system allowed the battery to be exchanged on regular interval. Implementing a battery current monitoring algorithm in the *HD_ExG_OS* firmware, an alarm for exchanging the battery could be set.

The developed firmware operated safe and stable in receiving commands from the remote PC and sending measured data back to the remote PC for further analysis. However during the multichannel test as described in section 3.4, data losses were noticed at the remote PC during the verification procedure. A data loss of ∼0.0135 – 0.85 % were observed if the sample rate of the ADC was set to 250 Hz, ∼0.032 – 74.32 %, 12.968 – 88.40 % for channel density ranging between 8–48 as shown in the Table 3-IV. After a thorough investigation with an Oscilloscope, no data loss between the Meridian-ADC and the µC of the Island-controller connected over SPI bus was found. Varying the number of channels and sample rate of the ADC, the problem could be found. After contacting the manufacturer of the WiFi-module, *Gainspan*, it was confirmed that SPI-bus of the module operates at the maximum of 1.4 MHz. Since the SPI speed of the ATxmega µC could be set to an integer factor of 1, the highest speed of the SPI between the µC and the WiFi module was set to 1 MHz. This was the bottleneck of the WiFi module and was not informed during the design of ExG-system. According to the MDD [**102**] and ISO14971 [**103**], a medical diagnostic product should be data loss free. However in case of wireless data communication, the protocol must ensure with the help of checksum if there has a data loss taken place. Since the developed ExG-system exhibited less than 1% data loss, an integration of a checksum as an error control process was required. In the appre-

hension of this issue, a checksum was already included in the *transmission header* of the ExG data stream and insertion of *frame marker* before each data packet assured safe detection of an error prone data packet. Moreover it allowed to exactly identifying the channel with data loss, so that at the remote PC responsible for verifying the data can issue a resend of that concerned data packet request.

The noise test results of the ExG-system showed an input noise level of ~11 µVpeak-peak which is relatively high for an ExG-system. The reasons of this amount was analyzed to have lied primarily in the design matrices of the Electrode-bus, high wide band noise of ~6 µV of the of the voltage reference *ADR1500*. In realizing a flexible solution the length of the Electrode-bus became longer (40 cm) which didn't have any shielding. The dimension of the Electrode-bus was susceptible to 50-Hz detector of main AC. There was also not sufficient separation between the analog and digital. As a result there was a crosstalk between the measurement channels of the Electrode-bus. Moreover the unwanted signals from the measurement apparatus at the measurement room constituted another amount of noise during the experiments. After locating one the causes of this high input noise of the system, a redesign of Meridian-ADC was carried out to solve the issue. With the help of the Meridian-ADC_v2, the input noise or the system resolution was reduced ~6.8 µVpeak-to-peak.

5.2 Analysis of the Time Synchronization

As previously stated the PBS protocol, to the authors' best knowledge, has not yet been implemented and experimentally evaluated in a hardware wireless network. However, for brevity, its implementation is not described here, but the reader is referred to the Appendix B. PBS proposes a novel

synchronization approach based on a two-way communication protocol assuming a Gaussian distribution of timing delays during the message transport. It further claimed better energy efficiency in comparison to other state-of-the-art protocols. Since our Chi-square test setup experimentally established that the difference in reception time of the SAs was approximately Gaussian, it was reasonable to assume that the delay time also has a Gaussian distribution, as assumed in [79]. This makes PBS a promising protocol for the envisioned application. Additionally, the novel HBS protocol (as described in the Chapter 4) and three other state-of-the-art protocols were implemented on the test-bed shown in the Figure 4.8. This allowed a comparison between the implemented protocols in term of energy consumption and sync error. The Table 4-VI presented a brief summary of the protocols implemented with their characteristics.

The implemented protocols can be categorized into two groups: i) two-way communication or sender-receiver communication protocols and ii) receiver-based communication protocols. PBS, TPSN belong to the first group and MBS, RBS, HBS to the second. In the following, their performance in terms of energy consumption (measured by the number of required timing messages) and synchronization accuracy is briefly discussed. The protocols belonging to the second group rely on a fixed broadcaster (in our test-bed. the SC), for which safe functioning needs to be guaranteed, whereas the protocols of the first group do not require a fixed broadcaster hence they do not depend on a safe functioning of a particular node in the network. The PBS protocol needed $2N$ timing messages to synchronize in comparison to $N{\times}L$ messages for MBS, $N+ L(L-1)/2$ for RBS and $2N(L-1)$ for TPSN where L is the number of nodes in the network. In the HBS protocol, the communication utilizes a the broadcast property of the radio layer so that it requires $N(L+1)$ messages.

From the detailed overview of the conducted measurement as shown in the results (see Table 4-V), It was evident that the MBS protocol resulted in a comparably high average sync error of 86.980 ms whereas the PBS and HBS protocols exhibited an average sync error of approximately 38.979 ms and 37.715 ms, respectively. However, the maximum sync error (226.188 ms) of the HBS protocol was comparatively higher than of PBS protocol which was 98.956 ms. The HBS protocol was also investigated for a long run-time experiment for 65 hours. The Figure 4.12 shows the sync error of SAs with respect to the GTP. It can be seen that the sync errors of the different SAs lay within a range of 0.343 ms–237.188 ms. Furthermore, the maximum sync error was approximately the same as for the 3 hour measurement result as presented in table IV. To get an estimate about the distribution of the sync error points in a 95% confidence interval, a separate bar-plot was generated after the statistical calculation of the measured dataset of sync errors. This was shown graphically in the Figure 4.13. It depicted the distribution of minimum, maximum, average, standard deviation of $\delta_{n,GTP}$. On all three SAs, an average value of $\delta_{n,GTP}$ less than 30 ms was observed.

The timestamping was triggered by reception of a message at the end of the signal processing path. Since the generation of the timestamp was executed at the top layer in the signal processing path, it induced four more non-deterministic sources of time delay additional to already existing delays if the timestamp were to be generated at the MAC layer. As a consequence a relatively large sync error during the evaluation of the protocols was noticed. Another issue was using a μC with FPU support. To resolve these issues, a redesign of sync modules were planned and developed. By generating the timestamps using the receiving activity map register of the *CC2451* transceiver, a better and stable average sync error of less than 2 ms was achieved considering a 95% confidence interval of the measured dataset of sync-error

with the implementation of PBS protocol. This reduction in sync error was achieved with the help of generation of the timestamps in the link layer of the Bluetooth stack. Apart from that the floating point unit (FPU) of the cortex processor was faster and more accurate in calculating the sync parameters (offset, skew) than that of the previous version where the FPU was emulated in the embedded software.

6 Application Scenario & Future Work

In this Chapter potential applications of the developed time synchronized cBCI system will be briefly presented. After that in the future work section, it will be described how the performance of the biopotential measurement system and time synchronization could be improved. Their applications of BCI are not only limited to robotics but has been extended to group experiment which was also mentioned in the Chapter 1.

cBCI could be used to for instance in the studies of neurophysiology where psychologist are interested to know if the same kinds of ERPs occurs if a group of probands are stimulated with the same kinds of stimuli. The concept of a quasi-stationary group experiment scenario is demonstrated in the Figure 6.1 where the probands are the attendants of a conference. They were all visualizing and listening to the same plenary talk and embodied with an EEG systems and SAs for recording EEG and for establishing time synchronization among them. However no such scenario has been found so far in available literature as far as author's knowledge is concerned.

6.1 Classroom Experiment

Figure 6.1 A typical quasi-stationary group experiment scenario where a group of attendants sited with less physical movement (quasi-stationary) of a conference listening and watching a keynote presentation. The attendants were wearing an EEG-cap and sync modules for recording the EEG data and to synchronize their clock at the rate of the global time provider.

Furthermore, such group experiment scenario can contribute to the fully automated driving using collaborative BCI. Such experiments will form the basis of future fully automated driving where car-to-car communication will be fused with collaborative BCI to improve the accuracy in decision making algorithms.

6.2 Dynamic Setup
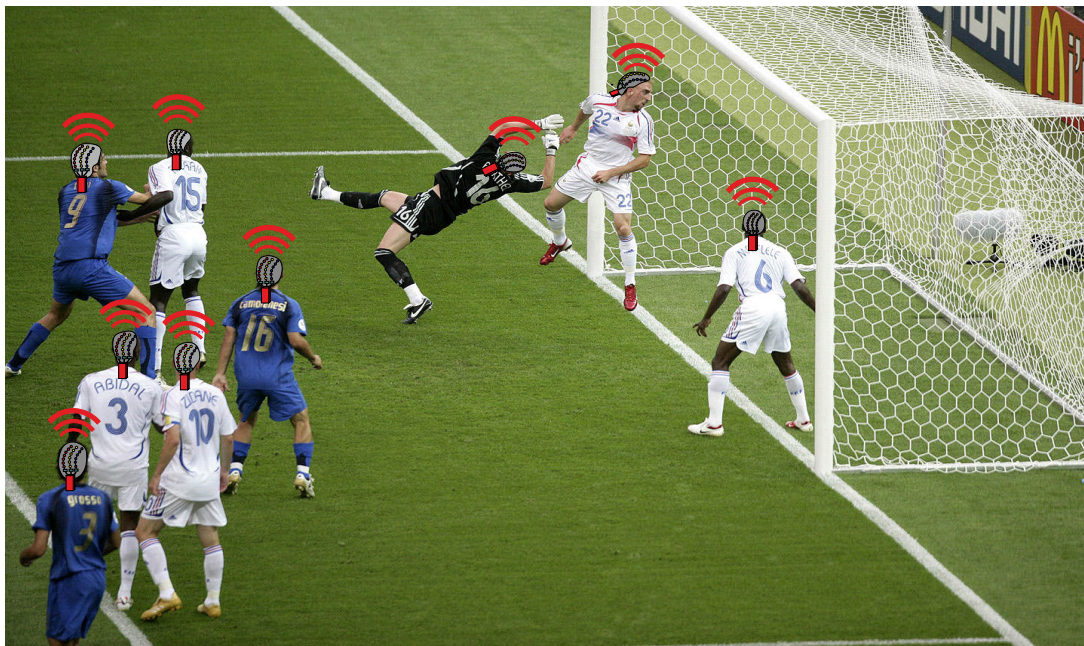
Figure 6.2 A dynamic scenario of group experiment where ERP of each proband (football players) are stimulated from the behavioral changes of the other players, game, environment – probands equipped with mobile EEG-cap and sync modules

Another interesting group experiment could be in sports where two or more players perform an action based on their learned methods, strategies. It's therefore of great interest for neurophysiologist, sport physiologist and even for mathematicians to know how does human brain process information while actively involved in sport since each player in a sport decides based on practices and speed of reflex the best possible move. Such a novel experiment scenario was conceptualized for this purpose and shown in the Figure 6.2 where a snapshot of a football match at a very crucial point of the match, corner scenario is considered since all players are much focused to perform their best play. Since the probands in such a scenario are mobile, so it was

required a system which is mobile, wearable and able to achieve online synchronization. So each player can be embodied with an EEG-system along with sync modules that were developed in this work. This will help to analyze the time synchronized ERPs data from a group of players for post processing.

6.3 Further Work

The developed ExG-system has the flaw of data loss due to the WiFi-module. This motivates a redesign of ExG-system with a module *CC33300* [104] from *Texas Instruments* which has a SPI bus speed scalable up to 16 MHz. Since dry electrodes with direct contact to skin over a metal pin using the resistive property was found to be painful for long time measurement, capacitive electrodes could be investigated for the purpose.

Time synchronization using Bluetooth low energy stack was investigated deeply using the broadcasting property of the stack as usage of BLE was pre-specified due to its popularity of easier certification procedure of medical diagnostic device. Other radio transceivers which also work in ISM band [105] (sub-GHz) could be investigated to attain a lower sync error as reported in the research works [76], [77], [78] utilizing MAC layer time stamping.

Bibliography

[1] B Z Allison, E W Wolpaw, and J R Wolpaw, "Brain-Computer Interface Systems: Progress and Prospects," *Expert Review of Medical Devices*, vol. 4, no. 4, pp. 463-474, July 2007.

[2] J. d. R. Millan et al., "Combining brain - computer interfaces and assistive technologies state-of-the-art and challenges," *Frontiers Neurosci*, vol. 4, pp. 1-15, 2010.

[3] A. Nijholt et al., "Brain-Computing Interfacing for Intelligent Systems," *IEEE Intelligent Systems*, vol. 23, no. 3, pp. 72-79, May/June 2008, doi: 10.1109/MIS.2008.41.

[4] B Allison, S Dunne, R Leeb, J d. R Millan, and A Nijholt, *Towards Practical Brain-Computer Interfaces: Bridging the Gap from Research to Real-World Applications*. Berlin: Springer-Verlag GmbH, 2012.

[5] A Kübler, D Mattia, R Rupp, and M Tangemann, "Facing the Challenge: Bringing Brain-Computer Interfaces to End-Users," *Artifical Intelligence in Medicine*, vol. 59, no. 2, pp. 55-60, October 2013.

[6] Y. Wang and T-P. Jung, "A Collaborative Brain-Computer Interface

for Improving Human Performance," *PLoS ONE*, vol. 6, no. 5, p. e20422, 2011.

[7] J. Guan and Y. Chen, "Single-trial EEG classification using in-phase average for brain-computer interface," *Frontiers of Electrical and Electronic Engineering in China* , vol. 3, no. 2, pp. pp 194-197 , June 2008.

[8] F B Vialatte, M Maurice, J Dauwels, and A Chichocki, "Steady-State Visually Evoked Potentials: Focus on Essential Paradigms and Future Perspectives," *Progress in Neurobiology*, vol. 90, no. 4, pp. 418-438, April 2010.

[9] E C Leuthardt, G Schalk, J R Wolpaw, J G Ojemann, and D W Moran, "A Brain-Computer Interface Using Electrocorticographic Signals in Humans," *Journal of Neural Engineering*, vol. 1, pp. 63-71, Jun 2004.

[10] A Matran-Femandez, R Poli, and C Cinel, "Collaborative Brain-Computer Interfaces for the Automatic Classification of Images," in *2013 6th International IEEE/EMBS Conference on Neural Engineering(NER)*, San Diego, CA, 2013.

[11] T. Togowa, T. Tamura, and P. A. Öberg, *Biomedical Sensors and Intruments*, 2nd ed. ISBN: 978-1-4200-9078-9: CRC Press, 2011.

[12] J. G. Webster and Eren H., *Measurement, Instrumentation, and Sensors Handbook - Electromagnetic, Optical, Radiation, Chemical, and Biomedical Measurement*, 2nd ed. ISBN: 978-0849383472: CRC Press, 2014.

[13] J. G. Webster and Eren H., *Measurement, Instrumentation, and Sensors Handbook - Electromagnetic, Optical, Radiation, Chemical, and Biomedical Measurement*, 2nd ed. ISBN: 978-0849383472: CRC

Press, 2014.

[14] C. M. Gaona et al., "Non-uniform High-Gamma (60 - 500 Hz) Power Changes Dissociate Cognitive Task and Anatomy in Human Cortex," *The Journal of Neuroscience*, vol. 31, no. 6, pp. 2091-2100, 2011.

[15] R.J. Staba, C.L. Wilson, A. Bragin, I. Fried, and J. Engel, "Quantitative analysis of high-frequency oscillations (80-500 Hz) recorded in human epileptic hippocampus and entorhinal cortex," *J Neurophysiol*, vol. 88, no. 4, pp. 1743-52, 2002.

[16] Hill NJ, Farquhar J, Schölkopf B. Martens SM1, "Overlap and refractory effects in a brain–computer interface speller based on the visual P300 event-related potential," *Journal of Neural Engineering*, vol. 6, no. 2, Apr. 2009.

[17] Woldorff, "Distortion of ERP averages due to overlap from temporally adjacent ERPs: analysis and correction".

[18] J. G. Webster, *Medical Instrumentation Application and Design (4th Edition)*. ISBN: 978-0471676003: Wiley, 2011.

[19] D. L. Schomer and F.L. de Silva, *Niedermeyer's Electroencephalography: Basic Principles, Clinical Applications, and Related Fields (6th Edition)*. ISBN: 978-0781789424: Lippincott Williams & Wilki, 2011.

[20] Springhouse, *ECG Strip Ease: An Arrhythmia Interpretation Workbook (1st Edition)*. ISBN: 978-1582555584: Lippincott Williams & Wilkins, 2012.

[21] Y. Tomita, T. Horiuchi S. Nishimura, "Clinical application of an active electrode using an operation amplifier," *Biomedical Engineering, IEEE Transactions on*, vol. 39, no. 10, pp. pp. 1096-1099, 1992.

[22] T. D. Clark, R. J. Prance C. J. Harland, "Electric potential probes - new directions in the remote sensing of the human body," *Meas. Sci. Technol.*, vol. 13, pp. pp. 163-169, 2002.

[23] D.R. Merrill, M. Bikson, and J.G. Jefferys, "Electrical stimulation of excitable tissue: design of efficacious and safe protocols," *J. Neurosci Methods*, vol. 141, no. 2, pp. 171-98, 2005.

[24] D.A. Robinson, "The electrical properties of metal microelectrodes," *Proceedings of the IEEE*, vol. 56, no. 6, pp. 1065-1071, June 1968.

[25] A. Hassibi, R. Navid, R. W. Dutton, and T. H. Lee, "Comprehensive study of noise processes in electrode electrolyte interfaces," *Journal of applied physics*, vol. 96, no. 2, pp. 1074-82, 2004.

[26] G. T. A. Kovacs, "Introduction to the Theory, Design and Modeling of Thin-Film Microelectrodes for neural Interfaces," in *Enabling Technologes for Cultured Neural Networks.*: Academic Press, 1994, pp. 121-166.

[27] A. Peper, C.A. Grimbergen A.C. Meeting van Rijn, "High-quality recording of bioelectric events Part 1 Interference reduction, theory and practice," *Medical and Biological Engineering and Computing*, vol. Vol. 29, no. No. 4, pp. pp. 433-440, 1991.

[28] M.D. Johnson, K.J. Otto, and D.R. Kipke, "Repeated voltage biasing improves unit recordings by reducing resistive tissue impedances," *Neural Systems and Rehabilitation Engineering (IEEE Transactions)*, vol. 13, no. 2, pp. 160-165, 2005.

[29] J.C. Huhta and J.G. Webster, "60 Hz interference in electrocardiography," *Biomedical Engineering (IEEE Transactions)*, vol. 20, no. 2, pp. 91-101, 1973.

[30] J.R. Wolpaw, N. Birbaumer, W.J. Heetderks, D.J. McFarland, and P.H. Peckham, "Brian-computer interface technology - A review of the first international meeting," *Rehabil. Engineering (IEEE Transactions)*, vol. 8, pp. 164-173, 2000.

[31] M.C. Roco and W.S. Bainbridge, "Converging Technologies for Improving Human Performance," 2003.

[32] Yijun Wang and Scott Makeig, "Predicting Intended Movement Direction Using EEG from Human Posterior Parietal Cortex," in *Foundations of augment cognition: Neuroergonomics and operational neuroscience (HCI 2009).*: Springer, 2009, pp. 437-446.

[33] J. Santamaria and K.H. Chiappa, "The EEG of drowsiness in normal adults," *J. Clin. Neurophysiol*, vol. 4, no. 4, pp. 327-82, 1987.

[34] T.P. Jung, S. Makeig, M. Stensmo, and T.J. Sejnowski, "Estimating alertness from the EEG power spectrum," *IEEE Trans. Biomed. Engineering*, vol. 44, no. 1, pp. 60-69, 1997.

[35] L. Summerer, D. Izzo, and L. Rossini, "Brain-machine interfaces for space applications-research, technologial development and opportunities," *Int. Rev. Neurobiol.*, vol. 86, pp. 213-223, 2009.

[36] E. Donchin and M. G. H. Coles, "Is the P300 component a manifestation of context updating?," *Behavioral and Brian Sciences*, vol. 11, no. 3, pp. 357-374, 1988.

[37] M. Kutas, G. McCarthy, and E. Donchin, "Augmenting mental chronometry: the P300 as a measure of stimulus evaluation time," *Science*, vol. 197, no. 4305, pp. 792-795, 1977.

[38] I.F. Akyildiz, W. Su, Y. Sankarasubramaniam, and E. Cayirci, "Wireless sensor networks: A survey," *Computer Networks*, vol. 38, no.

4, pp. 393-422, 2002.

[39] X T Du, W Zhang, and D Li, "A Real-Time and Low Power Working Method for Mobile WSN," *Mathematical Problems in Engineering*, vol. 2014, p. 6, 2014.

[40] C Otto, E Jovanov, and A Milenković, "Wireless Sensor Networks for Personal Health Monitoring: Issues and an Implementation," *Computer Communications (Special issue: Wireless Sensor Networks: Performance, Reliability, Security, and Beyond*, vol. 29, no. 13-14, pp. 2521--2533, Aug 2006.

[41] N. Tackett, E. Jovanov, and A. Milenkovic, "An implementation of time synchronization in low-power wireless sensor networks," *System Theory (SSST), IEEE 43rd Southeastern Symposium on*, pp. 61 - 66, 2011.

[42] H. Kopetz and W. Ochsenreiter, "Clock Synchronization in Distributed Real Time Systems," *IEEE Transactions on Computers*, vol. 36, no. 8, pp. 933 - 939, 1987.

[43] H. Kopetz and W. Schwabl, "Global time in distributed real time systems," *Technical Report 15/89*, 1989.

[44] S. Ganeriwal, R. Kumar, and M. B. Srivastava, "Timing-sync Protocol for Sensor Networks," in *Proceedings of the first International Conference on Embedded Networked Sensor System*, New York, 2003.

[45] M. Horauer, K. Schossmaier, U. Schmid, R. Höller, and N. Kerö, "Time Synchronization prototype system for Ethernet LANs," *34th Annual Precise Time and Time Interval (PTTI) Meeting*, pp. 1 - 17, 2002.

[46] A. B. Usakli, "Improvement of EEG Signal Acquisition: An Electrical Aspect for State of the Art of Front End," *Computational Intelligence*

and Neuroscience, vol. 2010, no. 2010, p. 7, 2009.

[47] F. Sarvar, N. J. Poole, and P.A. Witting, "PCB glass-fibre laminates: Thermal conductivity measurements and their effect on simulation," *Journal of Electronic Materials*, vol. 19, no. 12, pp. 1345-1350, 1990.

[48] Texas Instruments, "Micro-Power(50µA), Zerø-Drift, Rail-to-Rail Out Instrument Amplifier," *INA333 datasheet*, Jul. 2008 [revised Oct. 2008].

[49] Texas Instruments, "Low-Power, Single-Supply, CMOS, INSTRUMENT AMPLIFIERS," *INA331 datasheet*, Dec. 2001 [revised Apr. 2005].

[50] Analog Devices, "ADR1500 - 1.2875 V Micropower, Shunt Voltage Reference," *ADR1500 datasheet*, 2006.

[51] eemagine. Legal disclaimer. [Online]. http://www.eemagine.com/legal-disclaimer.html

[52] G.H. Klem, H.O. Lüders, H.H. Jasper, and C. Elger, "The ten-twenty electrode system of the International Federation. The International Federation of Clinical Neurophysiology," *Electroencephalogry Clin. Neurophysiol. Suppl.*, vol. 52, pp. 3 - 6 , 1999.

[53] Texas Instruments, ADS129x - Low-Power, 8-Channel, 24-Bit Analog Front-End for Biopotential Measurements, 2010.

[54] Texas Instruments, ADS1299 - Low-Noise, 8-Channel, 24-Bit Analog Front-End for Biopotential Measurements, 2012.

[55] IEEE, GET IEEE 802: Local and Metropolitan area network standards.

[56] Atmel, Preliminary - ATxmega128A1 / ATxmega64A1, 2013.

[57] GainSpan, Datasheet - GS1011MxxS Low-power wireless System-on-Chip Wi-Fi Module, 2013.

[58] W. Hofheinz, *Elektrische Sicherheit in medizinisch genutzten Bereichen*

(3rd Edition). ISBN: 978-3-8007-3588-4: VDE, 2014.

[59] P. Suresh, J. V. Daniel, V. Parthasarathy, and R. H. Aswathy, "A state of the art review on the Internet of Things (IoT) history, technology and fields of deployment," *Science Engineering and Management Research (ICSEMR), 2014 International Conference*, pp. 1 - 8, 2014.

[60] A. Amadi-Obi, P. Gilligan, N. Owens, and C. O'Donnell, "Telemedicine in pre-hospital care: a review of telemedicine applications in the pre-hospital environment," *International Journal of Emergency Medicine*, 2014.

[61] MathWorks, MATLAB.

[62] U Ghoshdastider, C Lange, R Viga, and A Grabmaier, "A Modular and Wireless ExG Signal Acquisition System with a Dense Array of Dry Electrodes," *Sensors, 2012 IEEE*, pp. 1-4, Oct 2012.

[63] Becker DE., "Fundamentals of Electrocardiography Interpretation," *Anesthesia Progress*, vol. 2, pp. pp. 53-64, 2006.

[64] U. Ghoshdastider, R. Viga, and M. Kraft, "Non-invasive synchronized spatially high resolution wireless body area network," *Intelligent Sensors, Sensor Networks and Information Processing (ISSNIP) 2014, IEEE 9th International Conference*, pp. 1 - 6 , 2014.

[65] Y.M. Chi and G. Cauwenberghs, "Wireless non-contact EEG/ECG electrodes for body sensor networks," *2010 international conference on body sensor networks (BSN)*, pp. 297 - 301, 2010.

[66] S. Farschchi, I. Mody, and J.W. Judy, "A TinyOS-based wireless neural interface," *26th international conference of the IEEE engineering in medicine and biology society*, pp. 4334 - 4337, 2004.

[67] L. Obeid, M.A.L. Nicolelis, and P.D. Wolf, "A multichannel telemetry system for single unit neural recordings," *Journal of Neural Methods*, vol. 133, pp. 33 - 38, 2004.

[68] X. Ye et al., "A portable telemetry system for brian stimulation and neuronal activity recording in freely bahaving small animals," *Journal of Neuroscience Methods*, vol. 174, pp. 186 - 93, 2008.

[69] S. Takeuchi and I. Shimoyama, "A Radio-Telemetry System with a Shape Memory Alloy Microelectrode for Neural Recording of Freely Moving Insects," *IEEE Transactions on Biomedical Engineering*, vol. 51, no. 1, pp. 133-137.

[70] P. Irazoqui-Pastor, I. Mody, and J.W. Judy, "Transcutaneous RF-powered neural recording device," *24th annual conference/ annual meeting IEEE biomedical engineering society*, pp. 23 - 26, 2002.

[71] antneuro. waveguard. [Online]. https://www.ant-neuro.com/products/waveguard

[72] MakerBot. Online Site - Replicator 2. [Online]. https://eu.makerbot.com/shop/de/3d-drucker/replicator-2/53/makerbot-replicator-2?c=47

[73] Rapsberry, Homepage - Rapsberry Pi.

[74] Raspbian,.

[75] Embedded Linux Wiki. Omxplayer. [Online]. http://elinux.org/Omxplayer

[76] L Girod, J Elson, and D Estrin, "Fine-Grained Network Time Synchronization using Reference Broadcasts," *SIGOPS Oper. Syst. Rev.*, vol. 36, no. SI, pp. 147-163, Dec 2002.

[77] B. Kusy, G. Simon, A. Ledeczi, and M. Maroti, "The Flooding Time

Synchronization Protocol," in *Proceedings of the 2nd International Conference on Embedded Networked Sensor Systems*, Baltimore, 2004.

[78] A. Marco et al., "Synchronization of Multihop Wireless Sensor Networks at the Application Layer," *Wireless Communications, IEEE*, vol. 18, no. 1, pp. 82-88, February 2011.

[79] E. Serpedin, K. Noh, and Qaraqe K.-L., "A New Approach for Time Synchronization in Wireless Sensor Networks: Pairwise Broadcast Synchronization," *IEEE Wireless Communications*, vol. 7, no. 9, pp. 3318-3322, 2008.

[80] H. Kopetz, *Real-Time Systems - Design Principles for Distributed Embedded Applications.* ISBN: 978-1-4419-8237-7: Springer, 2011.

[81] G. Stringham, *Hardware/Firmware Interface Design: Best Practices for Improving Embedded Systems Development.* ISBN: 978-1856176057: Newnes, 2009.

[82] U. Ghoshdastider, R. Viga, and M. Kraft, "Experimental Evaluation of A Pairwise Broadcast Synchronization in A Low-Power Cyber-Physical System," *Radio and Wireless Week (RWW)*, 2015, Accepted.

[83] U. Ghoshdastider, R. Viga, and M. Kraft, "Wireless time synchronization of a collaborative brian-computer interface using bluetooth low energy," *IEEE Sensors 2014: Valencia Conference Centre*, pp. 2250 - 2254, 2014.

[84] Afar communications, FCC Rules for Unlicensed Wireless Equipment operating in the ISM bands.

[85] Bluegiga.   BLE112   Datasheet.   [Online]. https://www.bluetooth.org/tpg/RefNotes/BLE112_Datasheet1.pdf

[86] P. Briff, A. Lutenberg, L.R. Vega, and F. Vargas, "On the Trade-Off of

Power Consumption and Time Synchronization Quality in Wireless Sensor Networks," *Sensors*, pp. 1, 4, 28-31, Oct 2012.

[87] Silicon Labs, Datasheet: USB-to-UART-Converter CP2200/1.

[88] Texas Instruments, BQ2407x - 1.5-A USB-Friendly Li-Ion Battery Charger and Power-Path Management IC, 2008.

[89] Hsing-Ya Chiang, Sheau-Chien Wang Hsiang-Te Ho, "Gaussian frequency-shift keying transciever for ISM wideband communication," US6480553 B1, Nov. 13, 1998.

[90] L. Zhou, X. Wang, W. Tu, G.M. Muntean, and B. Geller, "Distributed Scheduling Scheme for Video Streaming over Multi-Channel Multi-Radio Multi-Hop Wireless Networks," *Selected Areas in Communications, IEEE Journal on*, vol. 38, no. 3, pp. 409 - 419, April 2010.

[91] GCC Wiki. AVR GCC Wiki. [Online]. https://gcc.gnu.org/wiki/avr-gcc

[92] Fei Hu and Xiaojun Cao, *Wireless Sensor Network: Principles and Practice.* ISBN: 978-1420092158: Auerbach Publications, 2010.

[93] G.W. Corder and D.I. Foreman, *Nonparametric Statistics for Non-Statisticians: A Step-by-Step Approach.* ISBN: 978-0-470-45461-9: Wiley, 2009.

[94] SHARP, Datasheet: Photointerrupter GP1A52LRJ00F, 2005.

[95] IEEE, IEEE Standard for Floating-Point Arithmetic.

[96] P. Sommer and R. Wattenhofer, "Gradient Clock Synchronization in Wireless Sensor Networks," *International Conference on Information Processing in Sensor Networks*, vol. 37, no. 48, pp. 13-16, 2009.

[97] Valerie J. Easton and John H. McColl. Statistics Glossary. [Online]. http://www.stats.gla.ac.uk/steps/glossary/

[98] Atmel Corporation, "32-bit Cortex M4 Microcontroller SAM4E16," *ATSAM4E16C Datasheet*, Apr. 2015.

[99] BlueGiga, Datasheet: Bluetooth Modul BLE113, 2013.

[100] Texas Instruments, CC2541 - 2.4-GHz Bluetooth™ low energy and Proprietary System-on-Chip, 2012.

[101] Dynamis Batterien, Lithium-Polymer Battery LP 503759c, 2012.

[102] CROM Source, "EU Recast of the Medical Device Directives: The Rocky Road to the new Medical Device Regulation," *www.cromsource.com/wp-content/uploads/2012/12/EU-Recast-of-the-Medical-Device-Directives.pdf*, 2014.

[103] ISO, Risikomanagement nach DIN EN ISO 14971.

[104] Texas Instruments, CC3000 - TI SimpleLink™ CC3000 Module – Wi-Fi 802.11b/g Network Processor, 2012.

[105] Bundesnetzagentur (BNetzA). (2015, Apr.) Funkanwendungen auf den ISM-Bändern. [Online]. http://emf3.bundesnetzagentur.de/pdf/ISM-BNetzA.pdf

Appendix A

A.1 Data Traffic Estimation of the ExG-system

No. of Meridian-ADCs	No. Channels	Sample Rate	Total Data Throughoutput			
		[Hz]	[MB/s]	[KB/s]	[Byte/s]	[Bits/s]
1	8	250	0.006	5.981	6125	49000
2	16		0.012	11.841	12125	97000
3	24		0.017	17.700	18125	145000
4	32		0.023	23.560	24125	193000
5	40		0.029	29.419	30125	241000
6	48		0.034	35.278	36125	289000
7	56		0.040	41.138	42125	337000
8	64		0.046	46.997	48125	385000

1	8	500	0.012	11.963	12250	98000
2	16		0.023	23.682	24250	194000
3	24		0.035	35.400	36250	290000
4	32		0.046	47.119	48250	386000
5	40		0.057	58.838	60250	482000
6	48		0.069	70.557	72250	578000
7	56		0.080	82.275	84250	674000
8	64		0.092	93.994	96250	770000
1	8	1000	0.023	23.926	24500	196000
2	16		0.046	47.363	48500	388000
3	24		0.069	70.801	72500	580000
4	32		0.092	94.238	96500	772000
5	40		0.115	117.676	120500	964000
6	48		0.138	141.113	144500	1156000
7	56		0.161	164.551	168500	1348000
8	64		0.184	187.988	192500	1540000

A.2 Data Structure of the *Transmission Header*

					Transmission Header						
Byte #	**Name**		**Bit 7**	**Bit 6**	**Bit 5**	**Bit 4**	**Bit 3**	**Bit 2**	**Bit 1**	**Bit 0**	**Value/Hex**
1	ESCAPE	Byte 1	0	0	1	0	1	0	1	0	0x2a
2		Byte 2	0	0	1	0	1	0	1	1	0x2b
3		Byte 3	0	0	1	0	1	0	1	0	0x2a
4		ID	0	0	1	0	1	0	0	0	0x28
5	ISLAND_ID		1	0	0	1	0	0	1	0	0x92
6	MESSUNGS_ID		Measurement ID								
7	Timestamp: Byte 10		10th Byte of Timestring in seconds								
...	...		...								
16	Timestamp: Byte 1		First Byte of Timestring in seconds								
17	MERIDIAN_SLOTS		Meridian Slots								
18	MERIDIAN0	MERIDIAN_ID	MeridianID / 0x92=ADS1298 / 0x3e = ADS1299								0x92/0x3e
19		POWERDOWN	EL EC7	EL EC6	EL EC5	EL EC4	EL EC3	EL EC2	EL EC1	EL EC0	
...	MERID	MERIDIA	MeridianID								0x92/0

#	Name		Bit 7	Bit 6	Bit 5	Bit 4	Bit 3	Bit 2	Bit 1	Bit 0	Value/Hex
	IAN1	N_ID									x3e
...		POWERD OWN	EL EC7	EL EC6	EL EC5	EL EC4	EL EC3	EL EC2	EL EC1	EL EC0	
...	...	...				...					
32	MERID IAN8	MERIDIA N_ID				MeridianID					0x92/0x3e
33		POWERD OWN	EL EC7	EL EC6	EL EC5	EL EC4	EL EC3	EL EC2	EL EC1	EL EC0	
34	SAMPLES_PER_S ECOND					8-Bit-Value					
35	CHNSET		0		Gain		0		Mux		
36	Checksum					8-Bit-Checksum					

A.3 Data structure of the *Transmission Footer*

Byte #	Name		Bit 7	Bit 6	Bit 5	Bit 4	Bit 3	Bit 2	Bit 1	Bit 0	Value/Hex
						Transmission Footer					
1	ESCAPE	Byte 1	0	0	1	0	1	0	1	0	0x2a
2		Byte 2	0	0	1	0	1	0	1	1	0x2b
3		Byte	0	0	1	0	1	0	1	0	0x2a

3											
4		ID	0	0	1	0	0	1	0	0	0x24
5	Frame Counter	[31:24]				8-Bit-Value					
6		[23:16]				8-Bit-Value					
7		[15:8]				8-Bit-Value					
8		[7:0]				8-Bit-Value					
9	Timestamp: Byte 10					10th Byte of Timestring in seconds					
-	...					...					
18	Timestamp: Byte 1					First Byte of Timestring in seconds					
19	Checksum					8-Bit-Checksum					

A.4 Data Structure of the Transmission Data

Transmission Data										
Byte #	Name		Bit 7	Bit 6	Bit 5	Bit 4	Bit 3	Bit 2	Bit 1	Bit 0	Val-ue/Hex
1	ESCAPE	Byte 1	0	0	1	0	1	0	1	0	0x2a

2		Byte 2	0	0	1	0	1	0	1	1	0x2b
3		Byte 3	0	0	1	0	1	0	1	0	0x2a
4		ID	0	0	1	1	1	1	1	1	0x3f
5	Meridian 0	Byte 0			Data Byte					
6		Byte 1			...					
...		...			...					
28		Byte 23			...					
29	Meridian 1	Byte 0			...					
30		Byte 1			...					
..		...			...					
52		Byte 23			...					
53	Meridian 2	Byte 0			...					
54		Byte 1			...					
...		...			...					

55		Byte 23	...
..	...	...	...
29 + (M-1)*24	Meridian (M-1)	Byte 0	...
19		Byte 1	M = Slots of Meridian
20		...	...
21		Byte 23	...

A.5 Data Structure of the *Transmission Frame* Marker

Transmission Frame Marker

Byte #	Name		Bit 7	Bit 6	Bit 5	Bit 4	Bit 3	Bit 2	Bit 1	Bit 0	Value/Hex
1	ESCAPE	Byte 1	0	0	1	0	1	0	1	0	0x2a
2		Byte 2	0	0	1	0	1	0	1	1	0x2b
3		Byte 3	0	0	1	0	1	0	1	0	0x2a
4		ID	0	0	1	1	1	1	0	1	0x3D

Appendix B

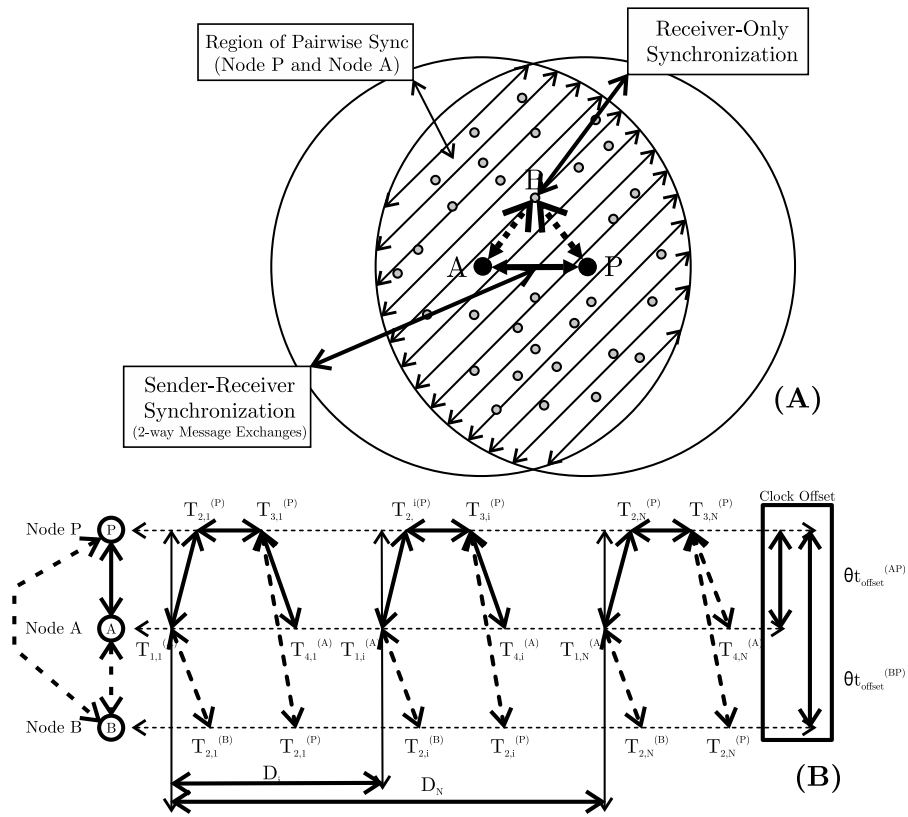## B.1 Pairwise Sender-Receiver Synchronization

Figure B.1 (A) Pairwise broadcast synchronization protocol with sender-receiver synchronization between A, P nodes and receiver-only synchronisation on node B; (B) clock synchronisation model with timestams exchange routine betwenn node P, node A, and node B

From Figure B.1

$$T_{2,i}^P = T_{1,i}^A + \theta_{offset}^{AP} + d^{AP} + X_i^{AP} + \theta_{skew}^{AP}\left(T_{1,i}^A - T_{1,1}^A + d + X_i^{AP}\right) \qquad (B.1)$$

$$T_{4,i}^A = T_{3,i}^P + \theta_{offset}^{PA} + d^{PA} + Y_i^{PA} - \theta_{skew}^{AP}\left(T_{4,i}^A - T_{1,1}^A - d - Y_i^{AP}\right) \qquad \text{(B.2)}$$

where $\theta_{offset}^{PA} = -\theta_{offset}^{AP}$, d^{PA} and X_i^{PA}, Y_i^{AP} denote the fixed and random portions of timingdelays in the message transmissions from *Node A* to *Node P,* respectively. The maximum likelihood estimator (MLE) of clock offset was found to be given by

$$\hat{\theta}_{offset}^{AP} = \frac{\overline{U} - \overline{V}}{2} \qquad \text{(B.3)}$$

With the delays in up-link $U_i \triangleq T_{2,i}^P - T_{1,i}^A$ and down-link $V_i \triangleq T_{4,i}^A - T_{3,i}^P$. From (B.1) *Node A* can be synchronized to the parent node *Node P* by simply taking the difference of the average delay observations $\overline{U} = \sum_{i=1}^N [T_{2,i}^P - T_{1,i}^A]/N$ and $\overline{V} = \sum_{i=1}^N [T_{4,i}^A - T_{3,i}^P]/N$. To guarantee a long-term stability of synchronization, a clock skew requires to be applied.

B.2 Considering Exponential Delay Model

Let X_N, X_1, Y_N, Y_N be independent and identically distributed (i.i.d.) exponentially distributed random variations (RV) with mean α. P and R then become zero mean Laplace distributed RVs with variance $2\alpha^2$, respectively. Thus, the joint PDF of P and R is given by

$$f_{P,R}(p,r) = \left(\frac{1}{2\alpha}\right)^2 e^{-\frac{(|p|+|r|)}{\alpha}} \qquad \text{(B.4)}$$

The likelihood function becomes

$$L(\theta_B, \alpha) = \left(\frac{1}{2\alpha}\right)^2 e^{-\frac{1}{\alpha}\left(\left|\frac{D_{(2)} - D_{(1)}(1+\theta_B)}{1+\theta_B}\right| + \left|\frac{D_{(4)}(1+\theta_B) - D_{(3)}}{1+\theta_B}\right|\right)} \qquad \text{(B.5)}$$

where $D_{(1)} \triangleq T_{1,N}^{A} - T_{1,1}^{A}$, $D_{(2)} \triangleq T_{2,N}^{A} - T_{2,1}^{A}$, $D_{(3)} \triangleq T_{3,N}^{A} - T_{3,1}^{A}$; $D_{(4)} \triangleq T_{4,N}^{A} - T_{4,1}^{A}$ and θ_B define the skew between *node* A and *node* P.

According to the derivation of the proposed clock skew estimate from the PBS paper, the following maximum likelihood like estimator (MLLE) was achieved:

$$\hat{\theta}_B^{EMLLE} = \frac{2D_{(2)}D_{(3)}}{D_{(1)}D_{(3)} + D_{(2)}D_{(4)}} - 1 \tag{B.6}$$

B.3 Considering Exponential Delay Model

If a Gaussian delay model was considered, the following MLLE could be achieved:

$$\hat{\theta}_B^{GMLLE} = \frac{D_{(2)}^2 + D_{(3)}^2}{D_{(1)}D_{(2)} + D_{(3)}D_{(4)}} - 1 \tag{B.6}$$

Lebenslauf

Name	- Unmesh Ghoshdastider
Geburtsdatum	- 30.07.1984
Geburtsort	- Kolkata
Nationalität	- Indisch

Ausbildung

Jul 2002 – Mär. 2005	Studium der Mathematik Universität Universität Kolkata Abschluss: B. Sc.
Apr.2005 – Feb. 2009	Studium der Elektrotechnik Vertiefung Elektronik Universität Duisburg-Essen Abschluss: B. Sc.
Feb.2009 – Mär 2011	Studium der Elektrotechnik- und Informa tionstechnik Vertiefung Mikro-und Optoelektronik Universität Duisburg-Essen Abschluss: M. Sc.

Anstellung

April 2011 – Mai 2015	Doktorand Universität Duisburg-Essen, Fachgebiet Elektronische Bauelemente und Schaltungen